Seismic Vulnerability Assessment of large Urban Areas using the TanDEM-X Mission and RapidEye Data

MASTERTHESIS

Submitted to the Paris-Lodron-University Salzburg
in partial fulfilment of the requirements for the degree of
Master of Science (M.Sc.)

submitted by

Marianne Jilge

Supervisor:

Dr. Dirk Tiede

Department:

Interfaculty Department of Geoinformatics – Z_GIS

Germering, August 2014

This master thesis emerged on the German Remote Sensing Data Center (DFD) of the German Aerospace Center (DLR), Oberpfaffenhofen

Department of Geo-Risk and Civil Security

Deutsches Zentrum
für Luft- und Raumfahrt e.V.
in der Helmholtz-Gemeinschaft

For my deceased sister Verena.

Abstract

Rapid urbanization processes and an increase of natural disasters such as earthquakes cause a high level of seismic risk. The occurrence of an earthquake in such densely populated regions would have catastrophically impacts on millions of people. Thereby, the largest risk emerged from buildings due to collapsed and falling remains. To mitigate this, the knowledge of how vulnerable certain urban areas are is mandatory. Therefore, to assess seismic urban vulnerability, detailed information of the building inventory itself is required. Already many studies focused on the assessment of seismic vulnerability of single buildings with remotely sensed data. The assessment of seismic building vulnerability requires therefore VHR remote sensing data, which are correlated with high costs and computation time when applying the assessment on large areas.

In this work seismic vulnerability of homogeneous urban structures with VHR remote sensing and DSM data of a large urban area are assessed to tackle this problem. This analysis was carried out for the Turkish megacity Istanbul, a very earthquake prone region. Therefore, optical remote sensing data, in particular RapidEye data, and elevation data from the TanDEM-X mission were applied. The utilization of these data necessitates initially some preprocessing (i.e. atmospheric correction, mosaicing) and preparation steps (i.e., nDSM calculation). To cope with the large urban extent, an object-based image analysis procedure to derive homogeneous urban areas by scale optimization is applied. In the next steps homogeneous urban areas are characterized by means of multisource remotely sensed data. Subsequently, feasible features by considering in situ information of seismic vulnerability are identified. Finally the seismic vulnerability of homogeneous urban areas is estimated by three approaches of statistical learning, due to varying a priori knowledge. The estimation of seismic vulnerability is grounded on Support Vector Machines, particularly on Support Vector Regression (SVR), an ensemble of One-Class Support Vector Machines (ν-OC-SVM), and Soft-Margin Support Vector Machines (C-SVM).

The procedure could gain viable estimation results of seismic vulnerability. Such as for the application of the SVR approach for Istanbul's district Zeytinburnu, the best model comprises a mean percentage error of less than 11% and a correlation coefficient of

0.75. The classification approaches aimed to identify different building types which are related with a certain degree of seismic vulnerability. The implementation of ν-OC-SVM ensembles could only obtain moderate accuracies for the best model (κ < 0.47). As opposed to the applied C-SVM approach, where for the best model an excellent accuracy of κ > 0.8 could be achieved. Therefore, this study features the potential of multi-source remote sensing data for assessing seismic vulnerability of urban structure types.

Acknowledgement

At this point I would like to thank everyone who has contributed to the success of this thesis.

First of all, my special thanks go to Christian Geiß for his outstanding supervision, patience, and his time to answer all my questions.

I would like to thank Dr. Dirk Tiede from the University of Salzburg (Z_GIS) for his valuable advice and the takeover of this thesis.

In addition, I am very grateful to Dr. Hannes Taubenböck for his comprehensive support.

Furthermore, I would like to thank Rolf Richter and Aliaksei Makarau for their advice regarding the atmospheric correction and testing the optical data with the not yet available new algorithm for VHR images. As well, thank you to Patrick Leinenkugel for his support with ATCOR.

My personal thanks are addressed to Birgit Jilge, Gerhard Jilge, and Matthias Würsching for their continuing encouragement - in many ways - during my studies and especially during my thesis.

List of Figures

Chapter 1: Introduction

Chapter 2: Foundations

Chapter 3: Study Area and Data Basis

Chapter 4: Extraction of Building Height Information

Chapter 5: Delineation of Urban Structure Types

Chapter 6: Characterization of Seismic Vulnerability Features

Chapter 7: Identification of vulnerable Urban Areas

Chapter 8: Results and Discussion

List of Tables

Chapter 2: Foundations

Chapter 3: Study Area and Data Basis

Chapter 6: Characterization of Seismic Vulnerability Features

Abbreviations

ATCOR	Atmospheric and Topographic Correction
BE	Bare Earth
CFS	Correlation-Based Feature Selection
C-SVM	C-Support Vector Machine
DLR	German Aerospace Center (Deutsches Zentrum für Luft- und Raumfahrt)
DSM	Digital Surface Model
DTM	Digital Terrain Model
ENVI	Environment for Visualizing Images
ESP	Estimation of Scale Parameter
GIS	Geographic Information System
GLCM	Gray-Level Co-Occurrence Matrices
GPS	Global Positioning System
GUF	Global Urban Footprint
$\mathbf{h_i}$	Initial Segmentation
I	Moran's I
IDW	Inverse Distance Weighting
LiDAR	Light Detection and Ranging
LUT	Look-up Table
MAPE	Mean Absolute Percentage Error
mPD	Mean Percentage Difference
nDSM	Normalized Digital Surface Model
NDVI	Normalized Differenced Vegetation Index
NIR	Near Infrared
$\boldsymbol{\nu}$**-OC-SVM**	nu-One-Class Support Vector Machine

OA	Overall Accuracy
OBIA	Object-Based Image Analysis
OBJ	non-ground Object
OC-SVM	One-Class Support Vector Machine
PA	Producer's Accuracy
pnDSM	Preliminary Normalized Digital Surface Model
potOBJ	potential non-ground Object
R	Correlation Coefficient
RE	RapidEye
RBF	(Gaussian) Radial Basis Function Kernel
SAR	Synthetic Aperture Radar
SRTM	Shuttle Radar Topography Mission
SVM	Support Vector Machine
SV	Support Vector
SVDD	Support Vector Data Description
SVR	Support Vector Regression
v	Intrasegment Variance
UA	User's Accuracy
USGS	U.S. Geological Survey
VHR	Very high resolution
WEKA	Waikato Environment for Knowledge Analysis

Contents

1. Introduction

1.1 Motivation

Since decades an increase of extreme natural hazards and their impacts on humans and the environment is reported. Especially in extremely dense populated urban areas, such as megacities in earthquake-prone regions the risk of being affected by a seismic event is high as never before. Earthquakes in sparsely populated and fragmented regions have only impact on a lower number of inhabitants and its infrastructure compared to densely populated regions. The continuing growth of urban population and the associated increase in constructions such as infrastructures, dwellings and industries would threaten the lives of million people if an earthquake would occur in such type of urban areas. As a sideway the damages and destructions could bring the economy in many countries, particularly in developing countries, to a standstill. The behavior of different constructions varies with respect to different factors (e.g. material, height, shape etc.) in the case of a seismic event.

Earthquakes are unavoidable but detailed knowledge about seismic risk can enable the decline of it and reduce damages and losses (BILHAM, 2009; TUCKER, 2013). Subject to different characteristics, areas or objects feature a differing vulnerability against earthquake. Therefore, numerous of properties of the building inventory have to be considered before making a statement about the seismic vulnerability for a specific level of ground shaking (ERDIK ET AL., 2003). The assessment of seismic vulnerability in urban areas is the aim of this study to tackle the seismic risk for an earthquake prone region.

Experts prognosticated a high probability for an earthquake with a magnitude larger 7 for the region around the Turkish megacity Istanbul (e.g., PARSONS, 2004). Such an earthquake would have disastrous consequences for the inhabitants, the city and the entire economy of Turkey. Against this background, the aim of this study is the seismic vulnerability assessment of such large urban areas by means of multi-source remote sensing data and a priori knowledge. Thereby, an assessment for single buildings is not usable due to cost and time. Therefore, a further challenging task is the derivation and identification of homogeneous urban areas, which are composed of similar buildings, to evaluate the entire city area.

1.2 State of the Art and Objectives

The assessment of seismic vulnerability in urban areas is not unprecedented. In conventional studies high detailed in situ building-by-building analysis by structural engineers are used to obtain seismic building vulnerability. However, such kind of vulnerability assessment is not applicable and feasible with respect to the high spatiotemporal dynamic of urban areas among others evoked by urbanization and economic processes. An aggregation of such in situ information to broader spatial units, for instance by aggregated census data inhibits the consideration of small-scale hazard effects in risk models (WIELAND ET AL., 2012). Therefore, the information of seismic urban vulnerability is imprecise, out of date or even not available for many regions.

This lack of availability can be tackled by remote sensing data (cf. chapter 2.4). In relation to seismic vulnerability assessment in urban areas, many studies have already profited from the advantages from remote sensing. TAUBENBÖCK ET AL. (2009) and BORZI ET AL. (2011) used remote sensing data for the characterization of different building types and gather fragility functions from them. Another approach was carried out by BORFECCHIA ET AL. (2009), where in situ data for various building types where collected and combined with remotely sensed data to derive seismic vulnerability by applying a supervised classification approach for the residual building inventory. GEIß ET AL. (2014 a, 2014 b) used a supervised classification and regression analysis to assess seismic vulnerability by a combination of in situ data of seismic vulnerability information and derived information of urban morphology by remote sensing data.

The problem on which scale the assessment should be carried out followed the idea of urban structure types. These are established in various applications of urban planning, mainly in Germany (HEIDEN ET AL., 2012). In chapter 2.1.1 it is referenced to some studies dealing with urban structure types.

MÜLLER ET AL. (2006) determined that urban structures can be valuable for assessing seismic vulnerability of buildings, if they are composed of similar building types and embedded in a spatial context. WIELAND ET AL. (2012) and PITTORE & WIELAND (2013) implemented the idea of urban structure types with Landsat images. They used urban structure information as strata for the subsequent analysis of the building stock with VHR optical remote sensing data and ground-based omnidirectional imaging (i.e., world housing encyclopedia information). A combination of them enabled finally the

assessment of probable seismic vulnerability. Thus, their approach focused on delineating homogeneous urban structures and afterwards assessing seismic vulnerability.

As opposed to WIELAND ET AL. (2012) and PITTORE & WIELAND (2013), this study applies a priori knowledge of seismic vulnerability for the identification of homogeneous urban structures by an object-based image analysis approach (PAL & PAL, 1993; BLASCHKE, 2010) for a set of optical VHR remote sensing data and DSM information. In this context the first research question related to this study emerged:

> *How can homogeneous settlement units be delineated and characterized by means of VHR multispectral remote sensing data and a digital surface model?*

For the assessment of seismic vulnerabilities of urban structures different approaches of statistical learning (CHEN & HO, 2008; CAMPS-VALLS ET AL., 2014), under consideration of in situ information should be implemented to address the question:

> *How accurate are SVM algorithms under consideration of different a priori knowledge for vulnerability assessment of urban structures?*

Consequently, this study is structured by introducing the fundamental terminology in chapter 2; the description of study area, data basis and relevant pre-processing steps such as atmospheric correction and mosaicing of the optical remote sensing data in chapter 3; the extraction of building height information from the DSM data by using morphological filters in chapter 4; followed by chapter 5, occupied with delineating homogeneous urban structures by image segmentation techniques with scale optimization; the determination and selection of seismic vulnerability features in chapter 6; chapter 7 introduces Support Vector Machines and the applied approaches of this study and the utilization of them to assess seismic urban vulnerability; in chapter 8 the results are presented and discussed, and finally, in chapter 9 a conclusion and an outlook is given. The general procedure of this work is illustrated in figure 1.

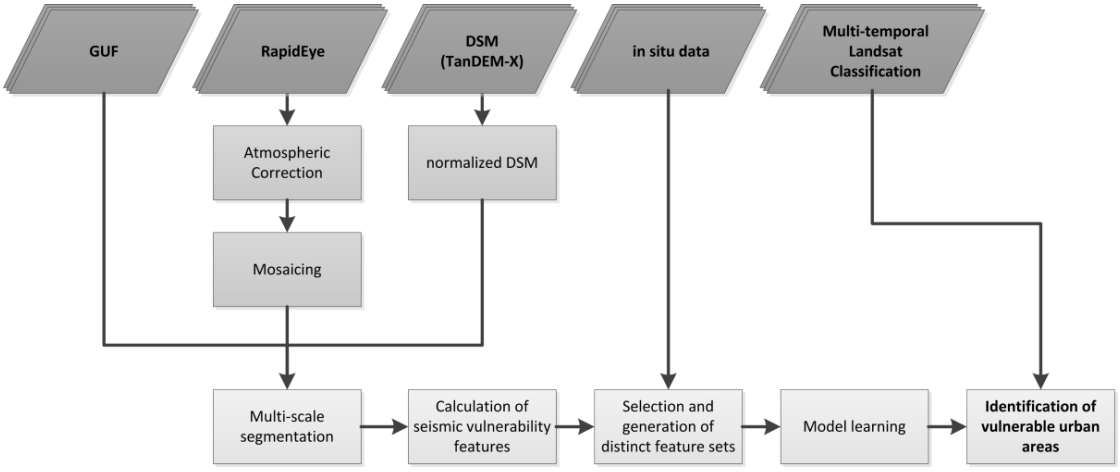

Figure 1: *Workflow of the entire procedure.*

2. Foundations

This chapter introduces the fundamental terminology regarding seismic vulnerability assessment in this study. That comprises the definition of urban areas, risk, natural hazards with focus on earthquakes, vulnerability, seismic vulnerability with focus on urban structures, and the concepts of remote sensing with respect to seismic vulnerability assessment in urban areas.

2.1 Urban Areas

The earth is populated by more than 7 billion humans (U.S. CENSUS BUREAU, 2014), whose accommodations are spread almost all over the earth in agglomerations of buildings, tents, or other constructions. In 2014 54% of the world's population live in cities (UN, 2014). Thereby, a rising tendency of the amount of people living in cities can be observed since years (cf. figure 2). The UNITED NATIONS (2003) prognosticated that 90% of the prospective demographic growth will be concentrated on urban areas (i.e., cities).

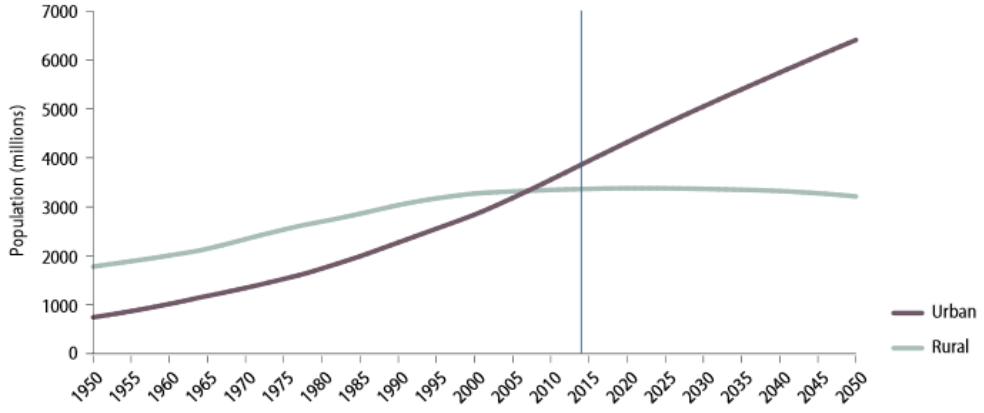

Figure 2: *Development of urban population (**Source:** UN, 2014).*

This process of migration to cities is called urbanization. In geography a city is a densely built-up area with a clear boundary to the hinterlands and of special relevance

for the hinterlands. Furthermore, a city is characterized by a certain population structure (so-called centre/periphery divide). Cities are also of a certain size. Especially mega-cities (e.g., Istanbul), cities with more than 10 million inhabitants (UN, 2003; MERTINS, 1992), register enormous urbanization with so far unpredictable regional and global consequences, which are only rudimentarily explored (HEINRICHS & KABISCH, 2006). Quantitative processes of growth whether population, infrastructure or economy and concurrency, complexity and overlaying distinct processes in megacities harbor unappreciable risk (TAUBENBÖCK, 2007) (cf. chapter 2.2).

2.1.1 Urban Structure Types

Urban areas are assembled of different urban structures types. Urban structure types are agglomerations of objects with similar physical (e.g., material), environmental (e.g., hydrology), and functional characteristics (e.g., land use) (PAULEIT & DUHME, 2000). Introduced in the 1990's in Germany, urban structure types were since then used for numerous applications of German cities especially in urban planning applications (e.g., PAULEIT, 1998; WITTIG ET AL., 1998; WICKOP ET AL., 1998; HEIDEN ET AL., 2012) and other countries (e.g., TANG, 2007). In addition, the idea of homogeneous urban structure types was inherited for a number of urban applications (e.g., BOCHOW ET AL., 2007; NIEBERGALL ET AL., 2008; BANZHAF & HOFER, 2008; WURM ET AL., 2009; BAUD ET AL., 2010; HELDENS ET AL., 2012; BECHTEL & DANEKE, 2012). However, the definition of urban structure types varies with respect to the application. Concerning this study, urban structure types were used to cope with the complex urban morphology of the study area by grouping them to homogeneous urban areas. Figure 3 schematically illustrates the agglomeration of varying types of buildings to homogeneous urban areas regarding similar land cover and land use.

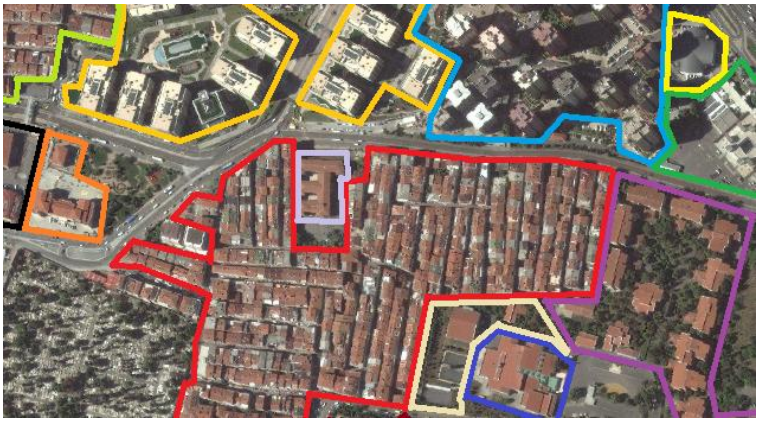

Figure 3: *Different urban structure types.*

MÜLLER ET AL. (2006) already proposed the application of urban structure types for seismic vulnerability assessment, particularly for areas with a large spatial extent. Therefore, agglomerations of single buildings with respect to certain conditions reduce the amount and complexity of information and consequently the processing time and costs. Hence, similar buildings (e.g., one family houses, storage depots etc.) were combined by means of optical remote sensing data and elevation information (i.e., nDSM) to homogeneous urban areas due to assumed similar seismic vulnerability. As already mentioned in chapter 1.2, WIELAND ET AL. (2012) and PITTORE & WIELAND (2013) used urban structures, derived by an image segmentation approach, for seismic vulnerability assessment. In this study the process of grouping similar objects was carried out by a framework of image segmentation (i.e., multi-scale segmentation) (cf. chapter 5.2).

2.2 Risk

In context of risk the term vulnerability is always present. Some definitions of vulnerability (cf. chapter 2.2.2) are even premised on risk. Thus, risk has to be expounded. Generally, risk is the probability to be tainted with certain positive or negative consequences, in other words chances or harm (BANSE, 1996; HOOD & JONES, 1996; FISCHHOFF ET AL., 1984). Hence, risk is fictive, prospective and associated with uncertainties (TAUBENBÖCK, 2007). BROOKS (2003) defined risk consequently as

$$Risk = Probability \cdot Consequences.$$

In the context of natural hazards or disasters, risk can be seen as the probability of damaging consequences (e.g., losses such as death, injuries, property, interrupted business operations, damaged environment) originated from natural or human-induced hazards and vulnerability (UNPD, 2004). The United Nations (UN, 1991) define risk, related to natural hazards as

$$Risk = Hazard \cdot Vulnerability.$$

The *probability* is linked with probability of occurrence and intensity of a hazard, for instance an earthquake. Risk is an inherent, existing, or originating circumstance in a social system (UN/ISDR, 2013). Therefore, the environment is at no time free of risk (BECK, 1986). Urban growth is such a fact and is associated with a high degree of risk (UNPD, 2004), for instance dangerous built constructions on hillsides due to excessive concentrations in urban areas. Relating to earthquakes, humans in countries with a rapid urbanization have a higher risk to die in case of an earthquake than in countries with a low urban growth (UNPD, 2004). The estimation of vulnerability in a certain region is crucial to induce countermeasures for risk minimization of prognosticated hazards (ZSCHAU ET AL., 2002). Subsequently the components of risk, hazards, especially earthquakes (cf. chapter 2.2.1), and vulnerability (cf. chapter 2.2.2) have to be defined.

2.2.1 Natural Hazards – Earthquakes

Natural Hazards are natural events allied with harms for humans and the environment. They can occur in different types of systems (e.g., atmospheric, hydrologic, oceanographic, volcanologic, seismic, and neotectonic) (GLADE ET AL., 2014) and varying intensity, which can constitute them to extreme events or disasters. In this chapter the emphasis was put on natural hazards of seismic origin, in particular earthquakes.

Worldwide 130 million humans are exposed by the risk of earthquakes every year (UNPD, 2004). Earthquakes are measurable and perceptibly sudden shocks of the earth surface. These shocks mostly occur due to moving processes of the tectonic plates, out of those the earth surface consist. Most of the earthquakes appear along the so-called fault lines of the plate boundaries due to collisions and subduction of the plates. Thereby, the intensity of ground shaking results from the magnitude itself (= intensity of an earthquake), distance from the fault (i.e., the more distant the lower the intensity of shaking), ground material and structure. Relating to the case study, Istanbul is located near one of these fault lines (North Anatolian Fault), thus the probability of an earthquake occurrence is high (i.e., high risk) in this region. The illustration below (figure 4) indicates the typical occurrence of earthquakes along the fault lines for one month (July, 2014).

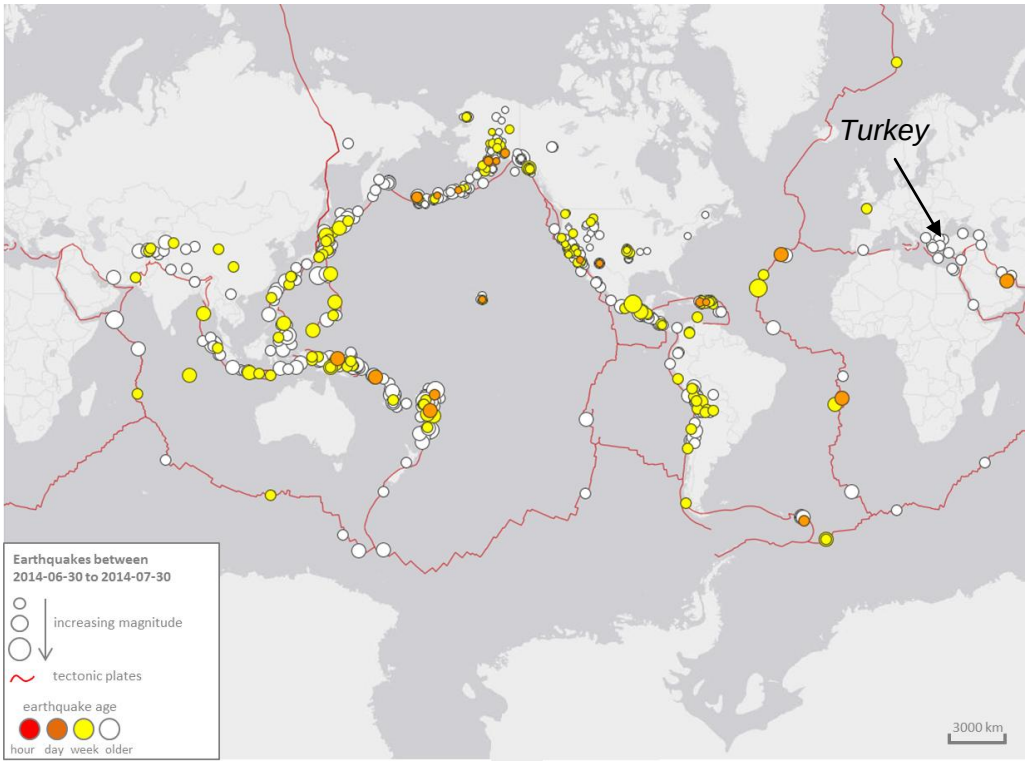

Figure 4: *Seismic activity along the tectonic plate boundaries during one month (**Source:** USGS, 2014; modified).*

Additionally, the level of seismic risk is still higher in densely populated regions, such as in megacities. In figure 5 an overview is given of the global spread of urban agglomerations. By comparing the locations of the urban agglomerations (figure 5) and the boundaries of the tectonic plates (figure 4), it is obvious that the majority of large urban agglomerations are located close to the faults. Therefore, the relevance of seismic vulnerability assessments in large urban areas is high.

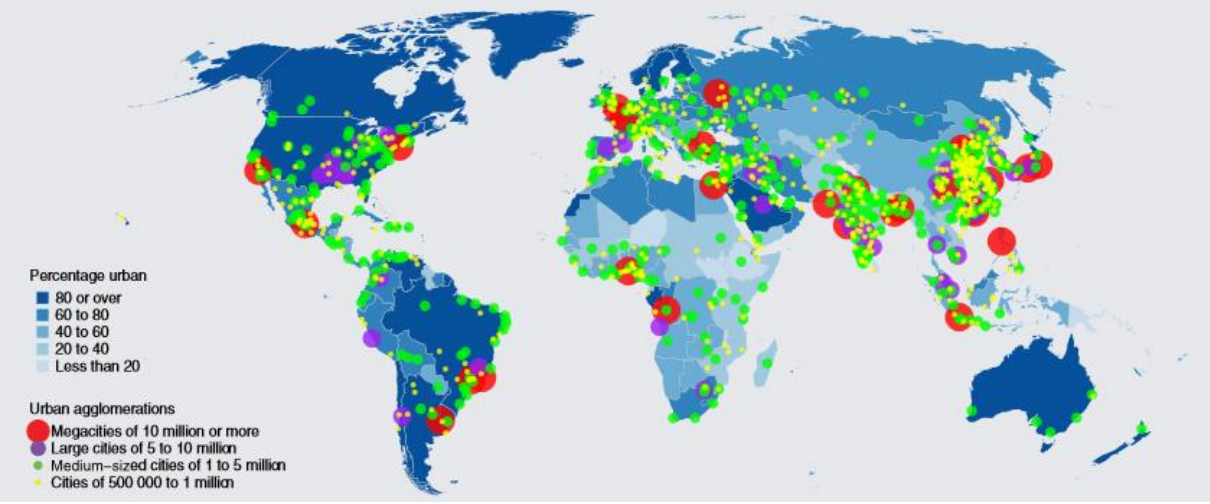

Figure 5: *Worlds urban agglomerations 2014 (**Source:** UN, 2014).*

2.2.2 Vulnerability

As a key component of risk (cf. chapter 2.2), and due to the aim of this study to assess seismic vulnerability, this chapter focuses on the definition of vulnerability. Furthermore, the assessment of ranking vulnerabilities is proposed by BIRKMANN (2006) due to the unsolved problem of earthquake prediction (ZSCHAU ET AL., 2002).

The term vulnerability is used in many disciplines (e.g., humanities, social sciences, economics, and natural sciences) and is therefore defined in many ways. In addition sub-disciplines of natural sciences characterize vulnerability regarding to the application context. TAUBENBÖCK (2007) gives an overview of the various interpretations of vulnerability.

With respect to natural hazards, such as earthquakes, vulnerability is defined as "*the condition determined by physical, social, economic, and environmental factors or processes, which increase the susceptibility of a community to the impact of hazards*" (UN/ISDR, 2004, pp. 16). Thus, vulnerability means the potential degree of loss regarding the occurrence of a hazard. The linkage between the degree of vulnerability and the impact of loss (i.e., risk) is illustrated in table 1.

	Vulnerability			
Loss (risk)	very high	high	medium	low
catastrophic				
intense				
noticeable				
slight				

Table 1: *Linkage between risk and vulnerability.*

CHAMBERS (1989) stated that vulnerability is composed of two principal elements, internal and external elements. The internal element comprises the potential of overcoming a natural hazard, that means realizing, cope with, and to recover from a natural hazard. On the other hand, the external element defines the danger of the structure with respect to the hazard. Hence, vulnerability can be formulated as

$$Vulnerability = \frac{Sensitivity \cdot Exposure}{Capacity\ \ of\ response}.$$

Thereby, sensitivity is the degree of danger and beside the exposure, which is the degree of duration of being imperiled, an external element of vulnerability

(BOHLE, 2001; CHAMBERS, 1989). The capacity of response (i.e., internal element) or coping capacity of a system is the ability to cope with the consequences of occurred hazards (GALLOPIN, 2006).

Therefore, to assess seismic building vulnerability, many vulnerability related factors (i.e., social, physical, economic,…etc.) have to be considered, such as the region itself, status of the society (i.e., poor or rich), development status (e.g., developing countries, industrial countries) etc. For instance, a physical factor is among others composed of location and structure (TAUBENBÖCK, 2009). Furthermore, development factors are directly associated with vulnerability (UN/ISDR, 2004), for instance high technical standards e.g. earthquake-resistant buildings decreases the seismic vulnerability. The knowledge and combination of vulnerability factors enable to measure the vulnerability and represents consequently the potential of coping (BIRKMANN, 2006). Therefore, initially the factors affecting vulnerability have to be determined (cf. chapter 6).

2.3 Seismic Building Vulnerability

Seismic building vulnerability means the vulnerability in the case of a seismic event (i.e., earthquake) for buildings and other dwellings. Therefore, seismic building vulnerability is the probability of failure of certain building types with respect to the magnitude of an earthquake (UNDP, 1994). Dwellings are connected with the highest seismic risk for humans (TAUBENBÖCK ET AL., 2009). Therefore, the physical vulnerability characteristics of buildings are seen as a measure for possible damages due to ground shaking processes of certain intensities during an earthquake (ERDIK ET AL., 2002). These physical indicators are mostly compiled by in situ surveys, where the principle weakness is the building material. In IAEE & NICEE (2004, pp. 4-5) some of these drawbacks of building materials are summed up:

- *Heavy weight and very stiff buildings, attracting large seismic inertia forces*
- *Very low tensile strength, particularly with poor mortars*
- *Low shear strength, particularly with poor mortars*
- *Brittle behavior in tension as well as compression*
- *Weak connection between wall and wall*
- *Stress concentration at corners of windows and doors*

- *Overall unsymmetry in plan and elevation of building*
- *Unsymmetry due to imbalance in the size and position of opening in the walls*
- *Defects in construction such as use of substandard materials, unfilled joints between bricks, not-plumb walls, improper bonding between walls at right angles, etc.*

Furthermore, information about the year of construction and building height (e.g., commercial, residential) affect seismic building vulnerability. The assessment of seismic building vulnerabilities by in situ surveys is due to time and money not applicable for large urban areas. Additionally, many studies did the assessment of seismic vulnerability only for small urban areas (e.g., districts). In this study the entire city of Istanbul is analyzed regarding their seismic vulnerability. To address this challenging task, remotely sensed data were used.

2.4 Remote Sensing

Remote sensing is the process of measuring or acquiring reflected or emitted electromagnetic emission of observed objects, without being directly in contact with them. These data are frequently acquired by satellites, aircraft or other aerial vehicles. Thereby, two types of remote sensing can be distinguished a) active remote sensing and b) passive remote sensing. Active remote sensing sensors emit and receive the backscattered emission of radar beams. Passive remote sensing sensors receive the reflected emission of an object and provide optical data. Generally optical remote sensing data provides spectral characteristics from objects, but are limited in weather conditions and can only work at daytime. Radar sensors, opposed to optical data work independently from weather conditions and time of day in consequence of the wavelength. Radar sensors receive complex information of intensity and phase of the backscattered radar beam. Radar data are commonly used for different applications such as measuring of moisture content, measurements of ice thickness, monitoring of deforestation, shifts of the surface in consequence of seismicity, erosion and mass wasting, relief maps,… etc. Furthermore, radar data provides also elevation data of the surface. With respect to this study a digital elevation model provided by the TanDEM-X mission (cf. chapter 3.2.1) (TanDEM-X is an active remote sensing sytem) was used to

derive building heights (cf. chapter 2.3) as expounded in chapter 4. A key advantage of this elevation data is the uniquely global availability from this satellite mission, and ensured therefore the transferability to other study areas. For a precise introduction to remote sensing the reader is referred to LILLESAND & KIEFER (2000); HILDEBRANDT (1996); JENSEN (2005); CAMPBELL (2002); MATHER (2004); RICHARDS & JIA (2006); SCHOWENGERDT (1997); and ALBERTZ (1991).

In contrast to in situ data, remotely sensed data are relative cost-effectively (partially free of charge), area wide available, and are characterized by a high repetition rate, which made them very efficient for different analysis. The provided context information is a further advantage of remotely sensed data (MÜLLER ET AL., 2006). It should be added that since the launch of very high spatial resolution (VHR) satellites detailed information on single building scale can be obtained. Therefore, remote sensing data provide a great opportunity towards in situ data for up-to-date analysis in rapid growing and dynamically urban areas. Furthermore, remote sensing data can be used for detecting structures, patterns and indicators of various scales (TAUBENBÖCK, 2007). That enables the derivation of vulnerability related features, as it is required for this study. The specific utilized remote sensing data for this study are outlined in chapter 3.2.1 and 3.2.2.

2.5 Remote Sensing and Seismic Building Vulnerability

As already mentioned, remotely sensed data were used in this study for the assessment of seismic vulnerability in urban areas. Due to the large spatial extent of the study area, single buildings were aggregated (cf. chapter 5) to homogeneous urban areas (cf. chapter 2.1.1) by means of image segmentation and subsequently feature to the calculation of seismic vulnerability properties. Remote sensing data were already used to observe the building stock and derive vulnerability related features (e.g., MÜLLER ET AL., 2006; BORFECCHIA ET AL., 2010; GEIß & TAUBENBÖCK, 2013). From multisource remote sensing data different features related to seismic vulnerability are derivable, such as height related features, spectral and spatial features, and shape etc.

In the following some seismic building vulnerability features which are derivable from remote sensing data, with respect to the applied urban structures in this study, are expounded:

Building shape:
More regular structures and symmetrical building shapes (i.e., rectangular shape) have a lower induced risk of seismic failure than irregular shaped buildings, such as L- or U-shaped building forms (FEMA310, 1998).

Building height:
Ideally a slight seismic vulnerability is composed to tall buildings, due to the relationship between building height, small floor area, and sophisticated structure with more steel in the concrete (EXPLORATORIUM, 2014).

Age of buildings:
Frequently new constructed buildings have to follow certain design codes, such as the earthquake design code of 1997 in Istanbul, which specify that all buildings built after 1999 have to follow the prescribed guidelines (CAKTI, 2013).

The specific features related to seismic vulnerability derived from the remote sensing data (cf. chapter 3.2.1 and 3.2.2) are outlined in chapter 6.

3. Study Area and Data Basis

This chapter outlines the study area Istanbul with its characteristics regarding the townscape and city structure, as well as its seismic activity while focusing on its seismic vulnerability. The rapid urbanization, which simultaneously induced a constantly changing and unorganized city structure within a few years, its geological setting along the north Anatolian fault, and the presumption of a major earthquake in the next years makes Istanbul to a relevant study area with respect to the assessment of seismic vulnerability. In addition, this chapter contains the data basis and relevant preprocessing steps for the assessment of seismic vulnerability of homogeneous urban areas.

3.1 Study Area - Megacity Istanbul

Since centuries the Bosporus built an important trade route for the entire trading operations between the Mediterranean Sea and the Black Sea. Simultaneously, this water connection between the two seas even forms the border between Europe and Asia. In consequence to the trading at about 660 BC, Greek settlers have built along the European seashore the first colony which was named Constantinople until renaming to Istanbul in 1930. Nowadays it is still an important international trade route particularly for the transportation of oil from the Black Sea.
The association of the Eastern and Western Roman Empire let Constantinople arose to the capital city in 330 AD. Since then the number of inhabitants increased constantly. In 1923 Constantinople lost the status of a capital city which was committed to Ankara. However, Istanbul kept its importance and the population numbers are steadily increasing. This is reflected in today's population of 14.16 million citizens (effective 2013) and depicts Istanbul as Turkey's largest city (TURKSTAT, 2014).

The province of Istanbul is located in the Marmara region in the northwestern Turkey. Istanbul expands along the eastern (Asian section) and western (European section) seashores of the Bosporus and is bounded by the Sea of Marmara in the south and the

Black Sea and woodlands in the north. An overview on the location of the study is given in figure 6.

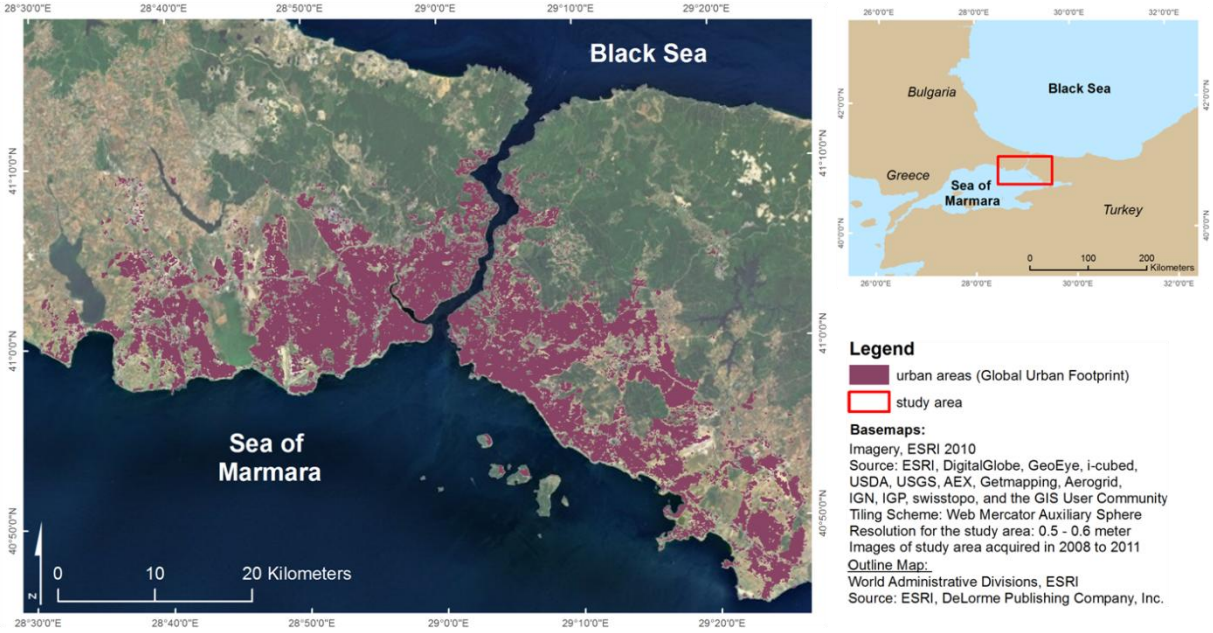

Figure 6: *Location of the study area Istanbul (Turkey).*

Already in the last century the number of inhabitants of Istanbul increased by an order of magnitude over less of decades. The population growth, mainly in the 1950s results from the domestic migration from other cities as well as from rural areas particularly as a consequence of the growing economy and industry (especially due to the textile industry, automobile industry, and tourism- and electronics industry (JINN.TV, 2012)), and therefore better employment- and income opportunities came up. This process of urbanization let Istanbul arose as a mega city (cf. chapter 2.1). Thereby, 18.47 % of the Turkish populations (76.67 million) live in Istanbul. In addition to the registered citizens of Istanbul, numerous illegal or unregistered people live in the city (cf. chapter 3.1.1). The amount of them can only be estimated and it is expected that the migration will persist (by estimated 400,000 per anno (JINN.TV, 2012)). The estimation of Istanbul's illegal living townsfolk runs into difficulties due to the hardly acquisition of Gecekondular (cf. chapter 3.1.1).

This enormous urbanization within the last decades changes the townscape and city structure of Istanbul which is described in chapter 3.1.1, and impacts the seismic vulnerability of the city (c.f. chapter 3.1.2).

3.1.1 Townscape and City Structure

The massive migration strained urban development and urban planning and lead to a complex and erratic city structure of Istanbul (CIRACI & KUNDAK, 2000). Triggered by the rapid urbanization, the townscape is greatly influenced by newly constructed buildings, but also illegal constructions, expansion of suburbs and illegal deforestation. Additionally, in Istanbul exist, as typical for the entire Turkey, so-called *Gecekondu* (literally translated “at night placed”) settlements and constructions. Gecekondular are squatter settlements without any permission, which have been built since the mid 1940s as improvised houses and shacks. Gecekondular do not only exist in peripheral areas, they also filled gap sites and do already exist as interurban socially deprived area (slum) (e.g., Tarlabaşı). The reason that the constructions were not immediately demolished, rely on a consuetudinary law from the Ottoman era. That implies that houses and shacks which were built overnight can not be demolished. Nowadays, the construction of Gecekondular is an on-going process, generally taking place in the marginal areas and extends the urban area of Istanbul by new districts. Today, Istanbul is divided in 39 districts with varying functions: residential areas, business and industry areas, suburbs, and mixed areas. They also differs in building types and building height, which are indicators for the afore-mentioned characterization of urban structure types (cf. chapter 2.1.1) and the subsequent characterization of seismic vulnerability features (cf. chapter 6).

Besides, many existing buildings were expanded without permission by new stories and extensions which leads to a changed static and therefore with conceivable consequences regarding the vulnerability in the case of a seismic event (JINN.TV, 2012). In addition, already authorized building projects had been modified, and extended even within its construction phase (JINN.TV, 2012). JINN.TV (2012) reveals that around 60-70% of Istanbul’s buildings raised without any regulatory supervision or investigation of its statics and with structural minimum standards. Hence, it is assumed that most of the buildings are not shake-resistant, although a law for earthquake engineering (since 1999) was issued. Despite of that, in 2008 197.000 of about 1,164,000 buildings were built after 1999, this means that 17% of Istanbul’s buildings were built between 1999 and 2008 (CAKTI, 2013).

Furthermore, the continuous increasing population development entails a densely built-up area, particularly vertical extensions (due to rising land prices and barely possible areal extent) and modernizing the city centers (JINN.TV, 2012). So Istanbul lost more

and more its typically traditional shaped oriental city structure and suppresses the traditional Turkish lifestyle, especially in the districts Levent and Maslak (GIRGERT, 2008). Beyond that, the insufficient and overloaded infrastructure will be further strained.

Related to the city structure the urban spatial structure of Istanbul depicts a new form regarding the migration (BERRY & KIM, 1993). CARACI & KUNDAK (2000) give a comprehensive overview of Istanbul's transformation since the 1950s from a monocentric to a polycentric city structure and its indicators. Resulting from the massive migration and affiliated construction boom of residential and commercial buildings, Istanbul was subject to underlying a permanently transformation with respect to its townscape. The different built-up structures lead to a varying seismic vulnerability in the case of a seismic activity as outlined in the subsequent chapter.

3.1.2 Seismic Activity

The dimension and rapidness of growth and change in urban areas lead to quickly outdated sources of information, ineffective control mechanisms of planning and therefore, a resulting unstructured and uncontrolled high-risk urbanization (TAUBENBÖCK, 2007). Due to an increased area of impervious surfaces, reduced open spaces, and buildings without any consideration of earthquake engineering, the region has lost much of its resilience (cf. chapter 2.2.2) against earthquakes, floods and other natural hazards (TERME, 2013). However, this study focuses on the seismic vulnerability, while Istanbul's vulnerability regarding other natural hazards should not be further discussed here.

Concerning the location, close to the North Anatolian fault, Istanbul is significantly exposed to earthquakes, because almost all earthquakes in Turkey and neighboring countries are related to tectonic movements (ERDIK ET AL., 1999). In the eastern Mediterranean the North Anatolian fault is a region with one of the most seismic events (ERDIK ET AL., 2002). Moreover, previous earthquakes along the fault (cf. figure 7) incline a westbound regime and give a possible forecast of the location (near Istanbul) of the next earthquake. According to PARSONS (2004), a 35-70% probability for the occurrence of an earthquake with a magnitude larger than 7 along the North Anatolian

fault within the next 30 years is expected. This fact and the spatial position of previous earthquakes along the North Anatolian fault in the 20th century can be obtained from figure 7.

Figure 7: *Historical earthquakes in the 20th century along the North Anatolian fault (**Source:** FRANCO & ALARCON, 2009).*

Date of historical earthquake	***Magnitude***
26.12.1939	*7.8*
20.12.1942	*7.3*
26.11.1943	*7.6*
01.02.1944	*7.4*
26.05.1957	*7.1*
22.07.1967	*7.3*
17.08.1999	*7.6*

Table 2: *Historical earthquakes in the 20th century along the north Anatolian fault.*

A considerable number of studies and organizations focused on the evaluated probability of an earthquake in Istanbul, and evaluated case scenarios, and the consequences for the population, the city, and the whole Turkish economy (e.g., ERDIK ET AL., 2004; UNITED NATIONS, 2007; FRANCO & ALARCON, 2009; ERDIK & DURUKAL, 2008; CAKTI, 2013). The high hazard potential (contiguity to the North Anatolian fault), the seismic vulnerability of infrastructure (e.g., buildings, bridges, supply lines), and the society cause a high seismic risk for the megacity (LÜHR ET AL., 2011). Despite of the high seismic risk for Istanbul, free spaces (i.e., possible evacuation areas) were obstructed. Also earthquake engineering related measures, anti-seismic building stock and infrastructure would minimize the damages for the city and its population (c.f. chapter 3.1.1). An earthquake in or close to Istanbul would provoke disastrous dimensions.

However, the seismic vulnerability is varying spatially over the municipal area due to different building types. This study focuses on the delineation of urban structure types and characterization of seismic vulnerability features by means of remotely sensed data. The applied remote sensing data and ancillary information derived from remote sensing data are introduced in the following chapter (cf. chapter 3.2).

3.2 Data Basis

This chapter introduces the utilized data sets and relevant preprocessing steps for this study.
By means of remote sensing the crucial characteristics of land cover and objects such as buildings with affiliated building height can be determined for the assessment of seismic vulnerability. This saves time-consuming and expensive fieldwork. For the assessment of seismic vulnerability of Istanbul's urban areas multi-sensor data, for various purposes were deployed.

3.2.1 Digital Surface Model from TanDEM-X

For the derivation of a normalized DSM (nDSM), which provides information about building heights, radar measurements were used. In contrast to optical systems (cf. chapter 2.4), which receive spectral information from objects on the surface (passive remote sensing), radar systems (active remote sensing) emit and receive radar backscatters which contain information about the ground topography and terrain by considering the time difference for emitting and receiving the radar beams. These measurements allow the generation of digital surface models (ASTRIUM, 2011).

In particular, DSM data from the TanDEM-X-mission were used. This mission is operated by the DLR since 2010 and based on two radar satellites, TerraSAR-X and TanDEM-X. These are scanning the earth in a formation flight with different viewing angles. TerraSAR-X and TanDEM-X are globally collecting very high resolution synthetic aperture radar (SAR) data (ESCH ET AL., 2012). The data are used for the creation of a digital surface model (DSM) with a high vertical resolution of up to 2 m and a horizontal resolution of 12 meters for the entire globe. The concepts and operating principles of the TanDEM-X mission is specified in KRIEGER ET AL., 2005, MOREIRA ET AL., 2004, ZINK ET AL., 2008 and ESCH ET AL., 2012. The TanDEM-X mission is the only one, since SRTM (Shuttle Radar Topography Mission), providing DSM data on a global scale with this high resolution (WEBER ET AL., 2006). Whereas SRTM data are only available with a resolution between 30 and 90 meters and only between 60°N and 56°S.

The appropriate intermediate DSM with a spatial resolution of ~11 m was used for the calculation of a nDSM, outlined in chapter 4, to derive the height of constructions. The applied DSM is composed of four tiles from the TanDEM-X Intermediate Digital Elevation Model (*N40E028, N40E029, N41E028, and N41E029*). Figure 8 illustrates the DSM data.

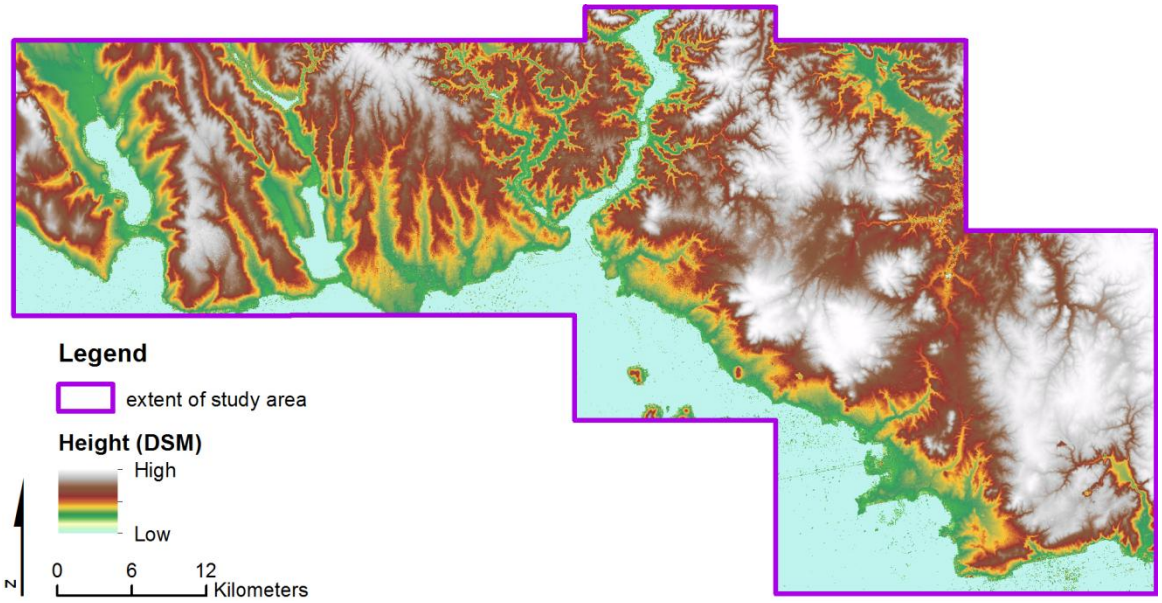

Figure 8: *Digital surface model for the study area.*

3.2.2 Multispectral Data from RapidEye

In contrast to radar data, multispectral remote sensing data provides information about the spectral characteristics of ground objects (cf. chapter 2.4). There exist a variety of different multispectral sensors with specific characteristics with respect to spectral and geometric resolution.

As explained in chapter 2.1.1 urban structure types are homogeneous urban areas containing aggregated single buildings of similar characteristics which were generated by a image segmentation procedure (cf. chapter 5). Hence, it is necessary that the spatial resolution of the multispectral data facilitates the detection of single buildings for the subsequent categorization of homogeneous urban structure types.

Accordingly, to cover the entire study area 6 RapidEye scenes with a spatial resolution of 5 meters (resp. 6.5 meters, dependent on the level), all acquired in 2009 were used. The product specifications of the commercial RapidEye data are illustrated in table 3.

RapidEye	
Number of satellites	5
Launch date	August 29th, 2008
Sensor type	Multi-spectral push broom imager
Operator	RapidEye AG, Black Bridge (renamed in November 2013)
Orbit Altitude	630 km, sun-synchronous orbit
Repetition rate	Daily (off-nadir), 5.5 days (nadir)
Swath width	77 km
Ground sampling distance (nadir)	6.5 m
Pixel size (orthorectified)	5 m
Spectral resolution	Blue: 440 - 510 nm Green: 520 – 590 nm Red: 630 – 685 nm Red Edge: 690 – 730 nm Near-Infrared: 760 – 850 nm

Table 3: *Specifications of RapidEye.*

During the further procedure the scenes were atmospheric corrected (cf. chapter 3.3.1) and a mosaic was generated (cf. chapter 3.3.2). The scene specific characteristics and the extent of the scenes are represented in table 4 and figure 9.

RE-Scene	553	556	606	609	610	613
Date of Acquisition	April 25, 2009	June 3, 2009	June 24, 2009	June 24, 2009	August 22, 2009	August 22, 2009
Satellite platform	RE-2	RE-3	RE-5	RE-5	RE-2	RE-2
Product Type/ Level	2A					
Upper Left (lat/long)	41.18702 / 28.42495	41.17852 / 28.99701	41.17321 / 29.28294	40.95718 / 29.27548	40.96246 / 28.99048	41.18313 / 28.71101

Table 4: *Characteristics of the applied multispectral data sets.*

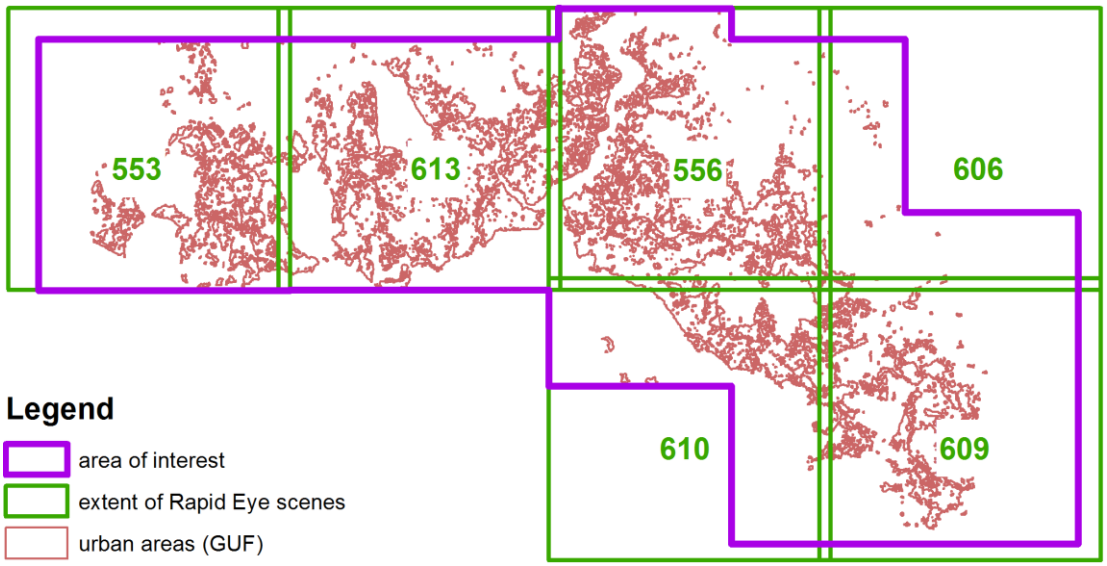

Figure 9: *Extents of RapidEye scenes.*

RapidEye disseminates data sets in different product types (levels), which define the already implemented processing steps on the scenes. The used scenes were allocated as Level 2A-data. Level 2A-data are radiometric and geometric corrected, resampled (from 6.5 to 5 m), and a coarse orthorectification is done. Nevertheless, the data were further geometric corrected for the process of mosaicing, as explained in chapter 3.3.2.

3.2.3 Ancillary Information derived from Remote Sensing Data

Earth observation data offers a vast number of area-wide information with a constant repetition rate and varying resolution and can be used as ancillary thematic geo-information for various studies. The subsequent two sub-chapters introduce two utilized products derived from remotely sensed data, the global urban footprint, a multi-temporal Landsat classification.

3.2.3.1 Global Urban Footprint (GUF)

The extent of the global urban footprint (GUF) for the region around Istanbul (illustrated in figure 6 and 9), constitutes the margin of the study area. The GUF is the result of a global analysis of urban areas by analyzing the texture information from SAR data (data from the TanDEM-X mission), followed by a pixel-based classification were the speckle intensity were examined to generate a binary mask, pointing out urban and non-urban areas (ESCH ET AL., 2012). The methodology of deriving urban footprints from SAR data is explicitly presented in ESCH ET AL. (2010), TAUBENBÖCK ET AL. (2011), and ESCH ET AL. (2012).

“The urban footprint mask primarily represents the location and distribution of man-made structures with a vertical component (strong scattering due to double bounce)” (ESCH ET AL., 2012, pp. 8). This does not contain only buildings - the GUF also comprises other constructions such as bridges located in a heterogeneous neighborhood (ESCH ET AL., 2012). The accuracy of the GUF-mask was tested on respectively 1500 random points on Ikonos and Quickbird images for 12 test sites (including Istanbul). A mean overall accuracy of 88.5% and a kappa value of 0.77 were found (ESCH ET AL., 2012). In Istanbul the quality of the GUF data set attained 95.8% in the accuracy assessment what represents the highest quality class (ESCH ET AL., 2010).

For this study the GUF was subject to some geometrical corrections with morphological operators such as growing and shrinking of the derived and classified GUF polygons, to obtain a generalized and homogeneous urban footprint mask. Furthermore, a

manual revision and refinement along the coast enhanced the accuracy of the applied GUF. Additionally, the GUF is used as thematic information for the procedure of segmenting the urban areas of Istanbul (cf. chapter 5) and builds therefore the extent of the study area.

3.2.3.2 Multi-temporal Landsat Classification

As mentioned in chapter 2.5, detailed information about the year of construction of buildings is a crucial physical parameter for seismic vulnerability assessment. This information can be derived by the long-term Landsat mission. Landsat satellites are providing constantly data since 1972 with a medium geometric resolution of a minimum of 30 m (multispectral) to 15 m (panchromatic), which can be used for temporal analysis. For instance, changes in the morphology of built-up areas can be analyzed.
For this study, an already existing time-series classification of Landsat imagery from 1975, 1987 and 2000 was used for the estimation of the overall period of construction of the urban structure types. The temporal classification carried out by TAUBENBÖCK ET AL. (2009), based on a spectral classification method, covering for each time frame the detected urban areas. TAUBENBÖCK ET AL. (2009) quote the accuracy of the entire classification to 90%. In figure 10 the detected urban areas in 1975, 1987 and 2000 are shown. How the information of the Landsat classification for this study is applied in practice is expounded in chapter 6.1.3, 8.2, and 8.3.

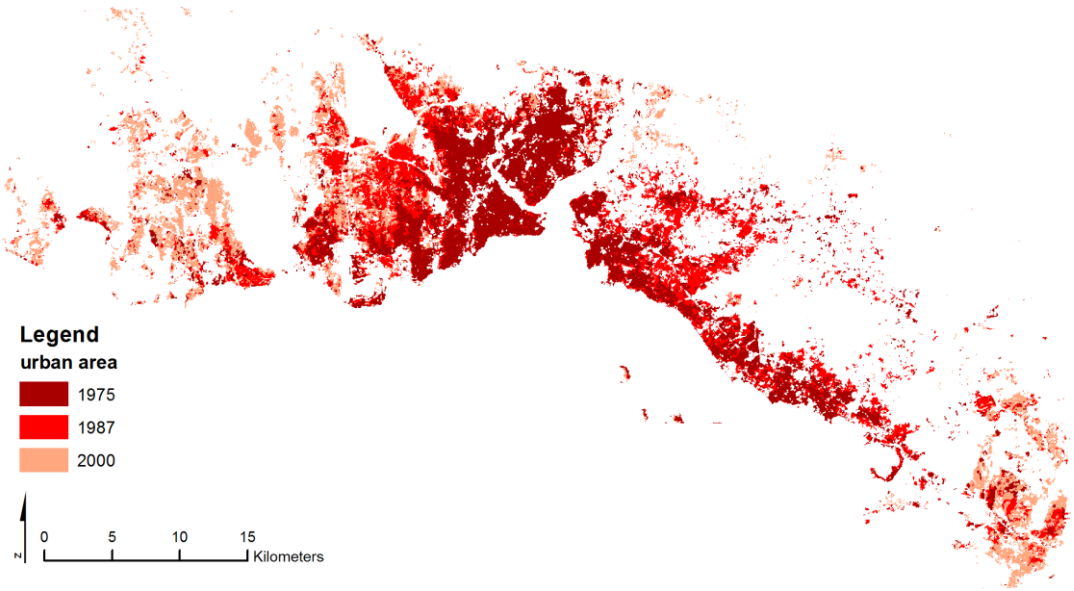

Figure 10: *Multi-temporal Landsat Classification extracted to the GUF.*

3.2.4 Reference Data

In TAUBENBÖCK ET AL. (2009) the damage grade on single buildings in the case of a seismic event for the district Zeytinburnu was examined. In their study they combined physical parameters derived from remote sensing data (e.g., height, roof type, age) and information gained by civil engineering (e.g., material). The spatial distribution of detected probable damage grades reveals commercial areas dominated by large factories as highly vulnerable areas, residential buildings of medium height as medium vulnerable and very high residential buildings as low vulnerable areas (TAUBENBÖCK ET AL., 2009). This relation was used as foundation for the assessment of seismic vulnerability for the entire city. Consequently this dataset is used as reference data. The single buildings were aggregated and represent the training data set for the regression technique Support Vector Regression (cf. chapter 7.2.1). In figure 11 the spatial distribution of probable damage grades of single buildings in Zeytinburnu explored by TAUBENBÖCK ET AL. (2009) is shown.

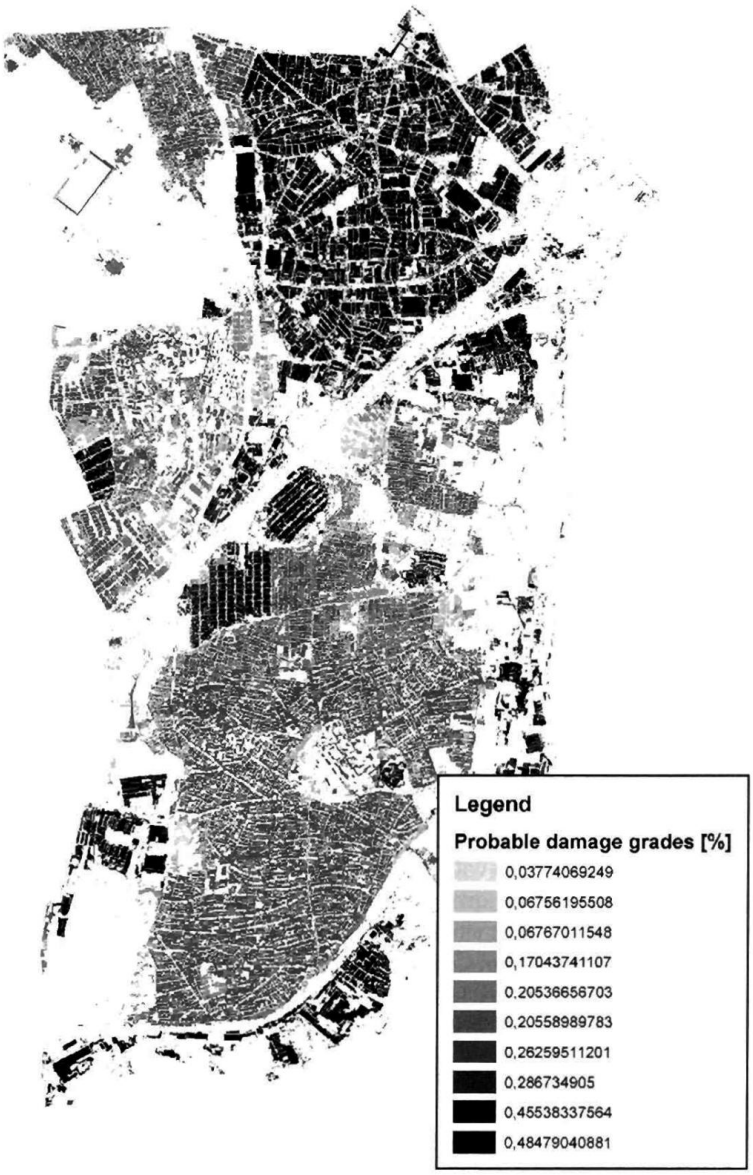

Figure 11: *Spatial distribution of expected building damage grades in Zeytinburnu (**Source:** TAUBENBÖCK ET AL., 2009).*

The determination of building material by civil engineering requires an indispensable in situ inventory which is not feasible for the large areal extent of the megacity. Thus, the assessment of single buildings by in situ surveys is not applicable for such large spatial extent. Additionally the assessment of seismic vulnerability of single buildings using information derived from remotely sensed data for the entire study area is especially due to processing time and resources not feasible. However, as previously mentioned in chapter 2.1.1 similar building types (e.g., building extent, building height) and its usage (e.g., commercial, residential) are aggregated to urban structures with similar

properties in respect of seismic vulnerability. Therefore, the single buildings of Zeytinburnu were aggregated to the final optimized multi-scale segmentation (cf. chapter 5.5.2) which is illustrated in figure 12.

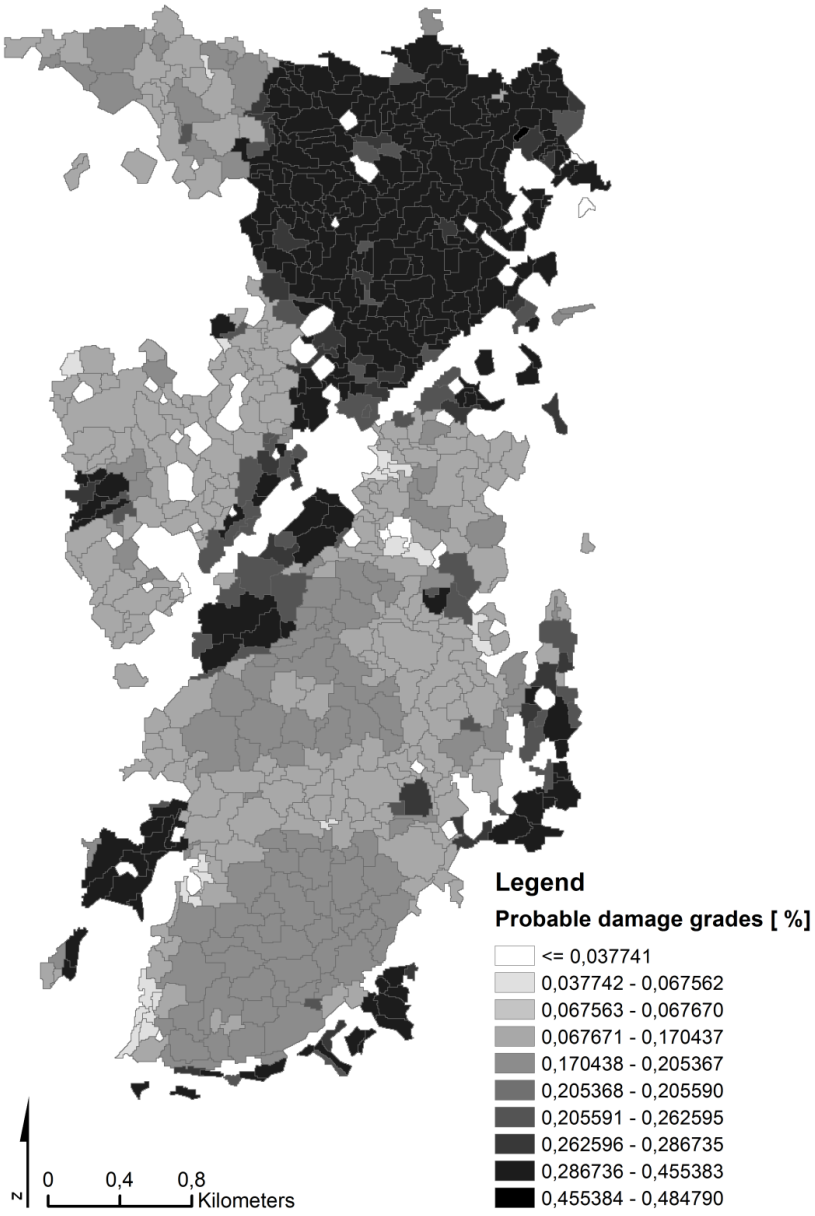

Figure 12: *Aggregated reference data set.*

Before the multi-scale segmentation was produced, some fundamental preprocessing steps on the optical data, outlined in the subsequent chapters (cf. chapter 3.3.1 and 3.3.2), followed by the derivation of building height information (cf. chapter 4) has to be done.

3.3 Pre-Processing of Optical Data

In this chapter the essential preprocessing steps on the optical data are outlined. This includes the atmospheric correction of the single RapidEye scenes, followed by stretching the histograms and co-registration for the subsequent process of mosaicing. The mosaiced scenes were then, beside the building height information (cf. chapter 4), used for the delineation of homogeneous urban areas (cf. chapter 5) and the determination of seismic vulnerability features (cf. chapter 6). Therefore, the preprocessing depicts a crucial step for the further analysis.

3.3.1 Atmospheric Correction

The acquisition of remote sensing imagery, especially with passive sensors (cf. chapter 2.4) is influenced by electromagnetic interaction caused by the atmosphere. Beside the effects of haze, clouds and water vapor the reflected spectra is exposed by scattering, absorption and reflection effects on aerosols (i.e., air particle). Additionally, variations of the viewing angle and diverse solar illumination angles lead to inconsistent reflectances, particularly at off-nadir records (MATHER, 2004). As a consequence, the reflected or emitted emission reaching the sensor differs from the spectral composition of an object on the earth surface. Furthermore, scattering and absorption processes also lower the intensity of the received reflections (NEUBERT & MEINEL, 2005).

An atmospheric correction is essential when more than a single image is subject to analyzes a region. In this study several features related to seismic vulnerability have to be derived from the optical remote sensing data for the entire city of Istanbul. With respect to the characterization of seismic vulnerability features (cf. chapter 6), uniform values of reflections were required. Besides, uniform reflection values can enhance the transferability of the classification algorithm. In this study the software package ATCOR (Atmospheric and Topographic Correction) (RICHTER, 1996) was used for atmospheric correction of the deployed RapidEye scenes (cf. chapter 3.2.2). ATCOR based on the MODTRAN-4 code (Moderate resolution atmospheric transmission) for transmitting electromagnetic radiation (BERK ET AL., 2003). The software provides, for multispectral remote sensing data, two general tools for atmospheric correction, ATCOR-2 and ATCOR-3. ATCOR-2 is basically used for flat terrain, whereas

ATCOR-3 is used for steep terrain, considering a DSM of similar resolution to the optical data. ATCOR-3 calculates slope, aspect, skyview factor, and topographic shadow (RICHTER & SCHLÄPFER, 2014) to compensate lightning effects from shading, tanning, terrain, and adjacency radiation (NEUBERT & MEINEL, 2005). Despite the availability of a DSM of ~11 m, the ATCOR-3 tool could not be used due to artefacts (especially in water surfaces) in the intermediate DSM. (RICHTER, 2014). Nevertheless, the focus in this study lay on urban areas which were mostly located in flat and moderate terrain, therefore ATCOR-2 could also attained valuable results. The atmospheric correction, applied with ATCOR-2, based on a uniquely sensor-specific calculated look-up table (LUT). Additionally, in the atmospheric correction the acquisition date (for different seasons), time (for different altitudes of the sun), altitude of the sensor, viewing angle, type of aerosol (was set to urban), and the mean visibility (is calculated automatically) was adjusted. With respect to these atmospheric- and scene-related parameters the atmospheric correction was carried out for all RapidEye scenes. The images are comprised by surface reflectances after the atmospheric correction (RICHTER & SCHLÄPFER, 2014). In figure 13 a RapidEye scene before and after the atmospheric correction is shown and illustrates the reduction of haze.

Figure 13: *Subset of a RapidEye scene before (left) and after atmospheric correction (right).*

3.3.2 Mosaicing

The histograms of the atmospheric corrected RapidEye scenes (cf. chapter 3.3.1) were stretched. The stretching of an image is applied to achieve an expanded range of grey-scale values for the entire image. More grey tones in an image enable a more precise analysis of objects. In addition, with respect to the subsequent process of mosaicing, it aims to represent similar objects (e.g., buildings) in different RapidEye scenes as equal (similar spectral properties) as possible. The histogram stretching for all RapidEye scenes was carried out with the software package ENVI 4.8 (Environment for Visualizing Images). At this, the range of reflectance values was specified to unsigned 8 bit, which depicts a range of 0-255 digital numbers. For stretching data values into a certain range linear and non-linear stretching methods can be applied. Linear stretching methods use arithmetical even functions for expand the data values over the defined range. In contrast to that, non-linear stretching methods are based on uneven operations such as logarithmic functions, and are deployed for stretching the atmospheric corrected images. However, in the literature there is no a priori suggestion for the selection of an ideal stretching method, it rather depends on the image itself. Hence, several methods and settings were tested. In general a linear stretching by a scene specific standard deviation was implemented. This method gained more contrast (SCHOWENGERDT, 2006), especially in extremely bright regions (e.g., streets). This change is shown in figure 14.

Figure 14: *Snippet of an atmospheric corrected RapidEye scene before (left) and after histogram stretching (right).*

Despite that the scenes were already georeferenced, but acquired from different platforms with varying orbital constellations. The scenes had shown a slight shift in latitude and longitude. Hence, the scenes were corrected in their position with respect to the neighboring scenes. Subsequently, the corrected RapidEye scenes were combined to a single composite image. This process is named mosaicing. Thereby, the difficulty is to avoid the visibility of the seam line between two scenes. Typically a cut-line along a natural border (e.g., streets, rivers etc.), covered by both images which should be combined, is used as seam. However, this necessitated major overlaps than only some pixels. Nevertheless, the RapidEye scenes had merely some pixels overlap, and as such a cut-line was not allocatable (cf. figure 9). Hence, the seam was blended and blurred (so called feathering) along the edges during the process of mosaicing of all RapidEye scenes in ENVI (EXELIS, 2014). The effects of the applied feathering technique can be seen in figure 15, which displays the seam for a subset of two mosaiced scenes. Due to the fact that the scenes were acquired between April (spring) and August (summer) (cf. chapter 3.2.2) the phenological state was differing and made it impossible to avoid hard seams. However, for the purpose of analyzing urban areas this can be largely neglected.

Figure 15: *Subset of the mosaic with blended and blurred (feathering) seam (right) and without (left).*

4. Extraction of Building Height Information

In chapter 3.2.1 it was mentioned that available DSM data allows to derive information about object heights (e.g., from buildings, trees etc.). For this study the extracted building height information should be considered as a feature related to seismic vulnerability. These information require further processing steps, which are specified in this chapter.

The DSM is a model of the earth providing the elevation of the earth surface comprising bare earth (fallow waste ground), vegetated objects (e.g., trees), and artificial objects such as houses, bridges, and other man-made structures. For the extraction of object heights (for this study the heights of buildings were of interest) the derivation of a digital terrain model (DTM) from the DSM is common. A DTM is a topographic model of the terrain relief without elevated objects. By applying the formula

$$nDSM = DSM - DTM$$

the terrain elevation (DTM) will be removed from the DSM to retrieve object heights stored in the normalized Digital Surface Model ($nDSM$). This calculation removes the elevation height (terrain) so that the objects of the nDSM stand on an elevation height of zero (VOZIKIS, 2004). Figure 16 graphically illustrates the characteristics of DTM, DSM and nDSM.

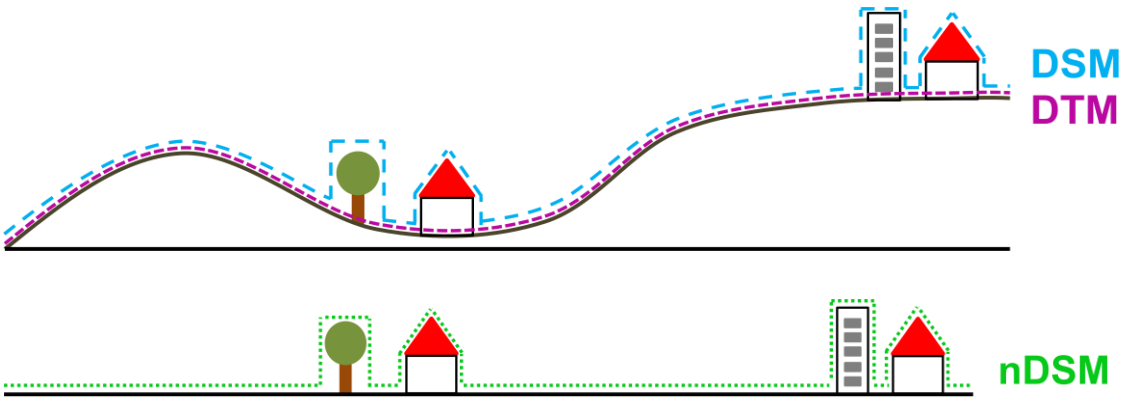

***Figure 16**: Characteristics of Digital Surface Model, Digital Terrain Model and normalized Digital Surface Model.*

Initially, the DTM has to be extracted from the DSM data, for which several approaches exist. Most of them are designed for DSM data with a much higher resolution than TanDEM-X data which were derived from laser scanning data (LiDAR), interferomentric SAR data, or from stereo images (GAMBA & HOUSHMAND, 2000; WURM ET AL., 2011; SIRMACEK ET AL., 2012). A large share of these approaches is based on filtering methods (KRAUS & PFEIFFER, 1998; AXELSON, 1999; ZHANG ET AL., 2003; SITHOLE & VOSSELMAN, 2004; LIU, 2000). In contrast to very high resolution DSM data not each filtering method is compatible with a DSM resolution of 10 m as it is the case of the utilized TanDEM-X DSM data. In this study morphological filters were used for the derivation of a DTM as proposed by GEIß ET AL. (2014c). On any number of occasions morphological filters were used to yield a differentiation of objects (non-ground objects) and bare earth (ground-objects) (ZHANG ET AL., 2003; CHEN ET AL., 2007; PINGEL ET AL., 2013).

In the subsequent chapter the morphological filtering and its application to the data set is described, followed by the normalization of DSM data (cf. chapter 4.2) to extract building heights. In addition the end of the chapter deals with the limitations of morphological filters.

4.1 Morphological Filtering

This chapter describes the utilization of morphological filters on a DSM data set to derive bare earth information for its generation of a DTM. As mentioned in the previous chapter (cf. chapter 4) for this study the proposed approach by GEIß ET AL. (2014c) was used. The approach is compounded by three main steps dedicated to GEIß ET AL. (2014c) as schematically illustrated in the flowchart in figure 17.

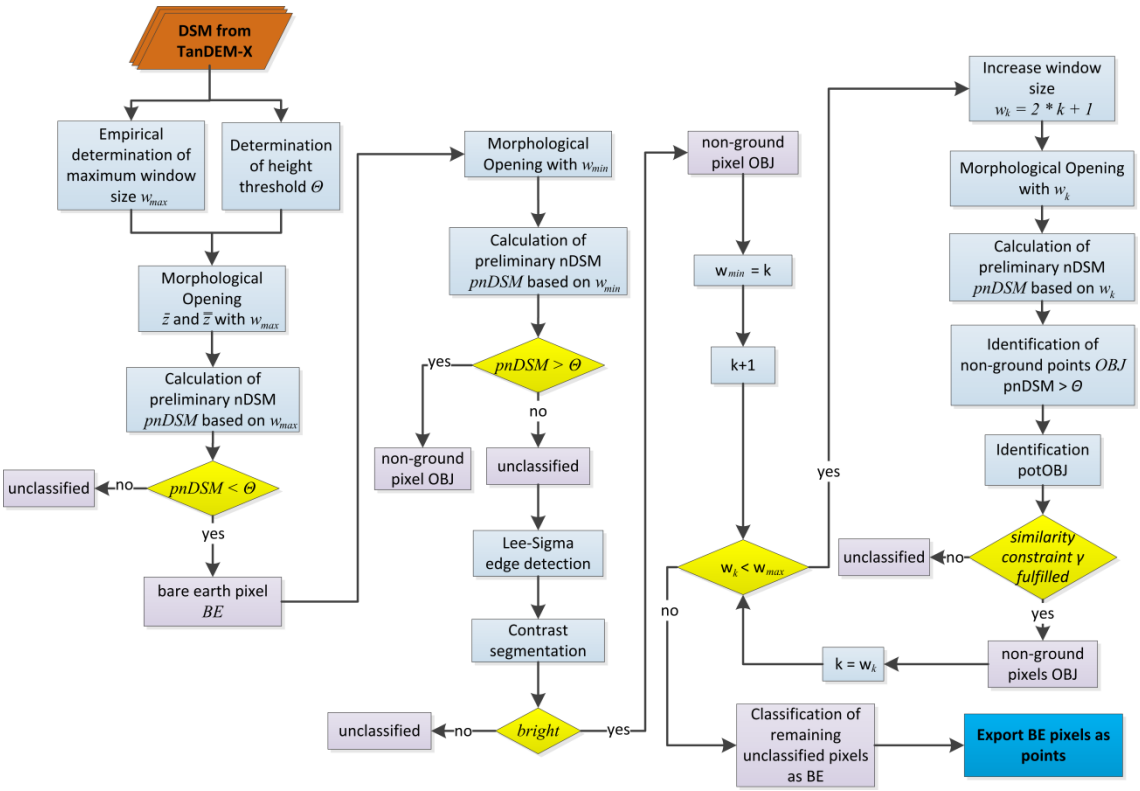

Figure 17: *Flowchart of the derivation of bare earth pixels (BE) and non-ground objects (OBJ).*

The application on Istanbul's DSM data was done using the software package eCognition Developer ® from Trimble which enables the development of object based image analysis (OBIA). However, the fundamental procedure of using morphological filters did not succeed the very common progress in OBIA to conduct segmentation first and followed by a classification. Due to the DSM resolution of ~11 m, it is possible that only one pixel represents a building, so the separation of non-ground objects (in this case 'buildings') and ground objects (bare earth) is based on a single pixel analysis. Thus, the analysis grounded on image objects which are represented by single pixels

derived by a segmentation technique where the image is split in squared image objects of equal size (e.g., Chessboard Segmentation).

Initially morphological opening operations on the DSM data were carried out to derive a DTM. Morphological opening operations enfolds a minimum and maximum filter with a structuring element w, which operates as sliding windows over the data set to derive the maximum values of the minimum elevation values z of the DSM. In mathematical morphology the minimum filter is known as special erosion operation with a constant z for w. The morphological minimum filter is described by

$$\bar{z} = min_{(x,y)\in w}\left(z_{x,y}\right)$$

where $z_{x,y}$ is the surface elevation at x and y. Correspondingly the maximum morphological filter, also known as dilation based on $\bar{z}$ is defined as

$$\bar{\bar{z}} = max_{(x,y)\in w}\left(\bar{z}_{x,y}\right).$$

To ensure that all non-ground objects in the opened surface $\bar{\bar{z}}$ can be removed, the size of the moving window has to be set to

$$w_{max} = 2 \times d_{max} + 1.$$

Thereby, w_{max} represents the maximum size of the moving window, and d_{max} depicts the “largest number of pixels between an object of interest pixel and the next ground pixel” (GEIß ET AL., 2104c, p. 5), or in other words that w exceeds the non-ground object itself. Due to the processing time and in consequence to the accuracy regarding the chosen kernel size, as described at the end of this chapter, the DSM data set was split into 14 tiles on which the entire procedure was implemented. Hence, w_{max} was chosen empirical for the largest identifiable building respectively for each tile, as graphical illustrated in figure 18.

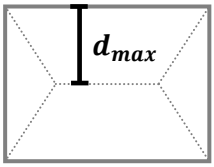

Figure 18: *Empirical determination of d_{max} for the largest identifiable non-ground object.*

Thus the minimum and maximum morphological filtering opening operations for each tile of the DSM data set was calculable. During each iteration a preliminary nDSM (*pnDSM*) is computed by subtracting the surface obtained by the maximum morphological filter from the DSM data. On the basis of this, ground objects (bare earth) could be identified if the pnDSM values were smaller than a certain height threshold θ. In regard the height threshold θ has to be chosen as the minimum height that a building can have. For this study it was assumed that buildings have a minimum size of 2.6 m. Therefore, pnDSM values lower θ = 26 dm were assigned to the bare earth class, so that small objects such as cars or bushes were removed.

In the subsequent step the morphological kernel size k was set to a minimum of 3, so that the morphological opening filters (w_{min}) could comprise an area of ~900 m² of the study area to analysis the remaining pixels regarding their belonging to the class non-ground objects (pnDSM > θ). For that purpose a pnDSM was generated again, this time using the maximum filter composed of the initial morphological kernel size. Additionally a region growing procedure was implemented to identify non-ground objects (OBJ). This procedure focuses to identify border pixels of buildings which could not covered by the minimum window size w_{min} and were therefore not included in the pnDSM. For the detection of these pixels a Lee-Sigma edge detection filtering (LEE, 1983) was integrated in the procedure. This filter uses “sigma probability of a Gaussian distribution to smooth variations in the image by averaging only those neighborhood pixels which have intensities within a fixed range of standard deviations o the center pixel” (GEIß ET AL., 2014c). The filter was used to extract bright edges by subtracting $\bar{z}_{w_{min}}$ from $\bar{\bar{z}}_{w_{min}}$. These edges generally represent border pixels of building which were not considered by w_{min}. After that a contrast segmentation was applied to separate bright and dark pixels for their subsequent classification of bright pixels as OBJ. In the next steps the procedure was repeated with a constantly increasing

morphological kernel size k until w_{max} was reached. The linear ascent of the sliding window size w_k is defined by

$$w_k = 2 \times k + 1$$

with k = 1, 2,…, d_{max} . In this way different sized objects could be analyzed by the iteratively process of increasing the window size for filtering the surface. While this process the pnDSM was frequently calculated with respect to k from which the pixels were assigned as OBJ if they were greater than θ and a similarity constraint towards already classified OBJ is fulfilled. The similarity constraint is used for analyzing a potential OBJ pixel $potOBJ$, to identify if it is part of a building or not. A pixel represents a potOBJ if an adjacent pixel depicts an OBJ pixel and shares a boundary with this OBJ pixel (e.g., pixels on building with varying height and a height difference $< \theta$ to its neighboring pixels can be mistakenly recognized as BE pixel). Thus these pixel represents potOBJ and were analyzed by

$$sim(potOBJ, OBJ) = \begin{cases} 1, & \left|\mu\left(\Delta Z_{OBJ}\right) - \Delta Z_{potOBJ}\right| \leq \gamma \\ 0, & else. \end{cases}$$

Where ΔZ represents the value of the respective pnDSM, μ its mean and γ the user defined threshold. In this study the γ-threshold was set to 0.8 m. This procedure of identifying OBJ is illustrated in the figure 19.

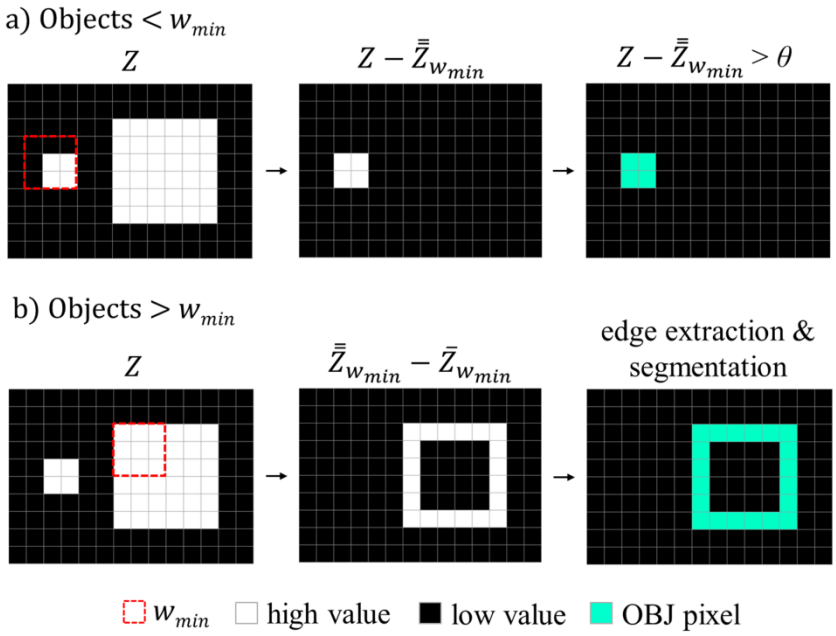

Figure 19: *Idealized procedure for the identification of initial OBJ pixels that represent the basis for the region growing procedure. (a) Objects that are exceeded by the minimum window size (w_{min}) can be identified by the application of a threshold θ on the pnDSM (Z - $\bar{\bar{z}}_{w_{min}}$). (b) Border pixels of objects that are not exceeded by w_{min} are identified by subtracting $\bar{z}_{w_{min}}$ from $\bar{\bar{z}}_{w_{min}}$. They are classified as OBJ by combining edge extraction filter and segmentation. Section a) of this figure visualizes the identification of initial OBJ pixels that are above elevation difference threshold θ and yet unclassified and section b) visualizes the subtraction of $\bar{z}_{w_{min}}$ from $\bar{\bar{z}}_{w_{min}}$ and identification of unclassified initial OBJ pixels by applying edge extraction and contrast segmentation. (**Source:** GEIß ET AL., 2014c).*

In the end all pixels which could not identified as buildings were classified as bare earth. The pixels classified as bare earth were exported as points for the subsequent step of generating a DTM (cf. chapter 4.2). Figure 20 illustrates a snippet of the separation procedure of BE and OBJ pixels within the eCognition environment.

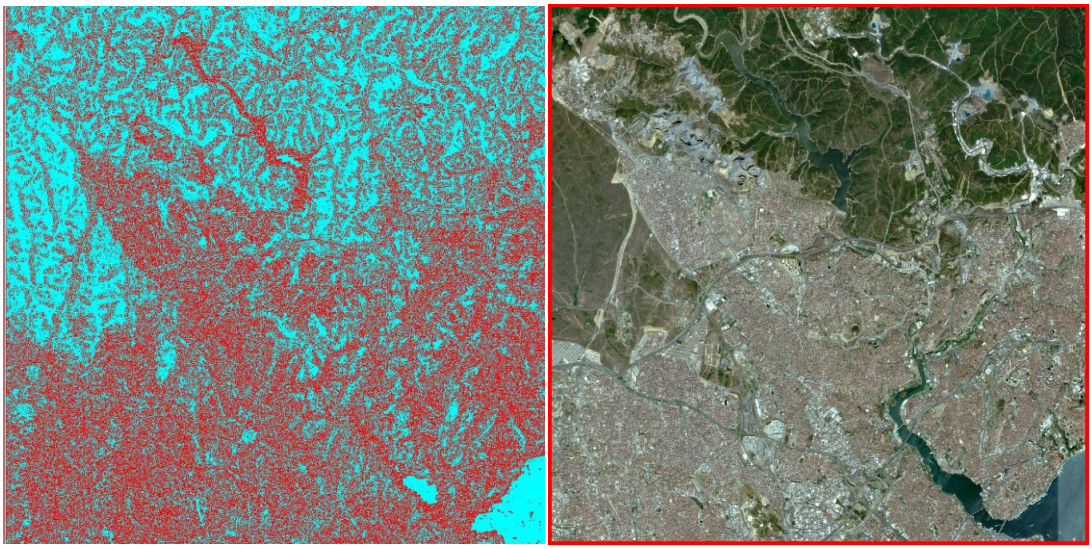

Figure 20: *Separation procedure (left) of bare earth pixels (blue) and building objects (red) for a snippet of the study area (right).*

However, as already mentioned before, the utilization of morphological filters to extract a normalized DSM is also attended with some limitations and drawbacks. As can be seen from the classification result a large number of OBJ pixels in mountainous areas were mistakenly founded (omission error). This may result from rock overhangs were the elevation strongly increases or decreases, and therefore the constraint to classify pixels as OBJ if the pnDSM > θ was complied. However, it is generally known that the utilization of morphological filters work well in flat terrain (KRAUSS ET AL., 2011) and exhibits errors in steep surfaces (MENG ET AL., 2010; MAGUYA ET AL., 2013). Hence, the GUF (cf. chapter 3.2.3,1) was used as a mask to extract subsistent urban areas from the subsequently calculated nDSM (cf. chapter 4.2) so that these errors could be avoided.

It should be added that due to the resolution of the DSM data small single buildings were not included in the data. However, the nDSM information was completely used for homogeneous urban areas (cf. chapter 2.1.1 and 5.2) and not only the information of each single building.

4.2 Normalization of DSM

This chapter outlines the computation of a DTM from the extracted BE points and the calculation of a nDSM to derive building height information. For generating a continuous terrain surface the BE pixels of all scene tiles were used for interpolating a DTM. In the spatial context, interpolation describes the process of estimating unknown values whilst taking into account known data values. This process comprises different methods. Generally it can be categorized into global and local interpolation techniques. Where global interpolation methods consider all available known data points for the estimation of unknown data values. Therefore, global interpolation methods depend on a single function for estimating unknown values for the entire region. Thus, changes in the applied data points (known values) will affect the interpolation result. In contrast, local interpolation methods use only adjacent values for the estimation of an unknown value. Hence, the function of local interpolation methods will be iteratively used on a defined range with known data values for the interpolation of unknown values.

It was assumed, that an unknown point will be similar to its nearest neighboring points. This is what Tobler's first law of geography implies that "everything is related to everything else, but near things are more related than distant things" (TOBLER, 1970, pp. 236), too. Therefore, a local interpolation method was chosen for the estimation of unknown points. Thus, the inverse distance weighting (IDW) interpolation technique was applied in this study to interpolate the terrain surface (DTM) analogous to ANDERSON ET AL. (2005). This method used the weighted distance average of an unknown point to adjacent observer points for its interpolation. The IDW is a commonly used interpolation technique with reliable accuracies (LAM, 1983). The mathematical function for the IDW interpolation of an unknown value ϑ is given by

$$\vartheta = \frac{\sum_{i=1}^{n} \frac{1}{d_i} \tau_i}{\sum_{i=1}^{n} \frac{1}{d_i}}.$$

Where τ_i represents the known value and d_i the distance to ϑ. In the GIS software package ArcMap, the IDW approach was already implemented and known as a fast interpolation method compared to other local methods (i.e., Kriging). Especially for large data sets such as for the study area of Istanbul, where over 21 million BE points have to be interpolated, the computation time depicts a crucial aspect. Furthermore, IDW is an exact interpolation method and does not manipulate the values of the input

points, only the values “between” were calculated. However, IDW is also afflicted by limitations, such as, that estimations can not exceed the minimum or maximum value of neighboring adjacent points. Therefore, this lead to the fact of flatting mountain peaks and valleys, if IDW is applied as interpolation technique for estimating elevation values of a terrain surface. In WATSON & PHILIP (1985) the limitations of the interpolation method IDW are specified. However, LLOYD & ATKINSON (2010) and ANDERSON ET AL. (2005) stated that simple interpolation methods such as IDW mostly provide sufficient results.

For all BE points, detected from the DSM, an IDW interpolation with adjusted power of 2 and a variable search radius of 12 was carried out. The power defines the distance exponent, where the larger the value, the less influence have distant points on the estimation. The search radius indicates a variable search radius around an unknown point to determine a certain number of points which were used for the interpolation. In the next step obvious erroneous negative values (e.g., -32.000 especially along the coastline) of the IDW interpolation outcome (DTM), as well as for the DSM dataset were set to zero. Subsequently, the nDSM was calculated by using the formula mentioned in chapter 4. Afterwards the GUF was used as a mask to extract building heights from the nDSM. So errors in mountainous areas, as previously mentioned in chapter 4.1 can be avoided. In figure 21 the utilized data set and the outcomes for the extraction of building heights is shown.

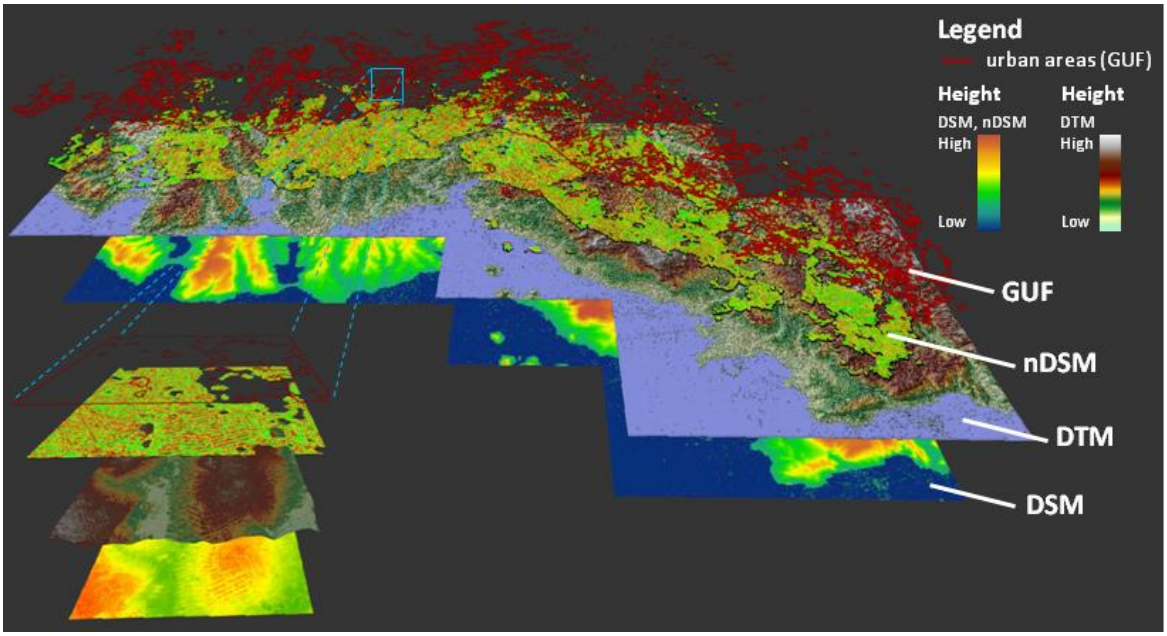

Figure 21: *Applied data sets for the extraction of building heights.*

For the further segmentation procedure, which based on the optical data and the nDSM, the nDSM data set was resampled to a resolution of 5 m, consistent to the resolution of the optical data. The pixels of the resampled nDSM and the pixels of the mosaiced RapidEye data had to correspond in size (resolution) and positional precision. Otherwise, during the segmentation procedure, sliver polygons would appear (cf. chapter 5.2.1) as a result of different pixel sizes.

5. Delineation of Urban Structure Types

In this section of the study the focus lies on the delineation of homogeneous urban structure types. This procedure was carried out with the software eCognition and includes the utilization of a multi-scale segmentation algorithm (ESCH ET AL., 2008; MARTHA ET AL., 2011). Initially a theoretical overview on image segmentation, its techniques as well as an outline of multi-scale segmentation introduces this process. After that the segmentation approach for the study area is described.

5.1 Segmentation Techniques

Since the launch of satellites which deliver very high spatial resolution remote sensing imagery, object-based image analysis gains more and more importance in image processing (BLASCHKE & STROBL, 2001; BLASCHKE, 2010). Traditional methods of pixel-based image analysis are exclusively based on pixel statistics and not involve form, texture and spatial context. This may tread to dissatisfaction to any classification result of high-resolution images. The smallest unit of an image is called pixel (pictorial element) and is also frequently representing a small portion of a classified high-resolution imagery, and does often not transmit significant image semantics (BAATZ & SCHÄPE, 2000). This is related to heavily varying spectral characteristics of single pixels in high-resolution images (e.g., gaps in streets caused by vehicles and shadow etc.) (YU ET AL., 2006).

Object-based image analysis is based on two main pillars, segmentation and 'objectivation' e.g. classification (BLASCHKE ET AL., 2014). Segmentation depicts the initial step of object-based image analysis and aims at generating meaningful objects in the image by grouping neighboring pixels based on distinct homogeneity criteria. PEKKARINEN (2002) defined image segmentation as the division of images "into spatially continuous, disjoint and homogenous regions" (PEKKARINEN, 2002, pp. 2818).

For segmenting an image several techniques are available which were briefly revealed. The focus of the section was put on the applied region-growing segmentation technique, due to the fact that this segmentation technique is most common used one

in remote sensing (ESPINDOLA ET AL., 2006). The categorization of image segmentation techniques is not strict however, some may discriminated:

- *Region based segmentation*
- *Edge based segmentation*
- *Threshold based segmentation*
- *Clustering techniques*

Moreover, the region based segmentation technique rest upon splitting and merging (UNIVERSITY UTRECHT, N. D.). Both operations are based on a previous conducted initial segmentation. The merging operation can be used to merge similar adjacent objects when the image is over-segmented, or splitting inhomogeneous segments into smaller homogenous ones (splitting operation), if the initial segmentation achieved an under-segmentation. The terms over- and under-segmentation will be defined later in this chapter.

In general the segmentation technique applied in this study is based on a region-growing segmentation algorithm deployed on the fractal net evolution approach (BAATZ & SCHÄPE, 2000) with the software product eCognition® to build image object primitives (BAATZ & SCHÄPE, 2000). The fractal net evolution approach in eCognition is the most commonly used approach in remote sensing applications (BAATZ ET AL., 2005). This algorithm is called “multiresolution segmentation” (BAATZ & SCHÄPE, 2000) and is a bottom-up approach by starting at the pixel-level (‘one-pixel objects’) (BENZ ET AL., 2004). Afterwards pixels are merged to objects in an iterative process until some user-defined homogeneity criteria are fulfilled. The homogeneity criterion is compounded by compactness, shape, and scale (so-called ‘scale parameter’). With the scale parameter the average object size can be influenced - the object size increases with increasing scale parameter and vice versa.
The major weakness in region-growing image segmentation techniques is the appearance of different sized real world objects which leads to an over-segmentation and/ or under-segmentation. Over-segmentation is defined as the generation of too many segments for a real world object and under-segmentation as the computation of too less segments, whereby the boundaries of the real world object were dispersed. The subsequent categorization of different object types (e.g., landcover types) may lead to their misclassification. One opportunity to overcome this issue is the generation and utilization of different segmentation levels (segmentations with different sizes of

generated segments) which can be used for the subsequent categorization (using splitting and merging). These segmentation levels should be linked to each other as a hierarchy of super-objects and sub-objects. Thereby, sub-objects are objects with a smaller scale factor and are contained in their super-objects. Consequently super-objects can be defined as the aggregation of finer image objects (sub-objects). Another option, as applied in this study, is the combination of different scales to a final segmentation by their optimization. With respect to the research question, which comprises the delineation of homogenous urban structure types, these categories can be varying in their spatial extent (e.g., large agglomeration of terraced houses and small areas with commercial buildings). Thus single segmentation levels would not be sufficient, and for this reason the approach of combining different segmentation scales is believed to represent the most efficient approach for this study. For that purpose the multiresolution segmentation algorithm was implemented in several consecutive automated segmentation steps to generate an optimized multi-scale segmentation for the subsequent characterization of urban structure types. In the following, the concept of the multi-scale segmentation and its application for the study area is delineated.

5.2 Multi-scale Segmentation

Multi-scale segmentation or multi-level segmentation represents an advanced approach to image segmentation as it was implemented in this study to categorize miscellaneous homogeneous urban areas for the further assessment of seismic vulnerability. This segmentation approach was inspired by the human visual perception synthesizing to the gestalt law (founded by WERTHEIMER, 1923; KÖHLER, 1929; and KOFFKA, 1935), which describes the behavior to isolate objects in their entirety. So the human eye perceives various scales of grouped objects consisting of inherent scale domains.

Related to object-based image analysis this approach is dealing with the links between interrelated objects (object hierarchy) of different size and scale (e.g., single trees, types of tree, forest) derived from one of the standard segmentation techniques mentioned in chapter 5.1. In other words different segmentation levels provide different levels of detail which do not appear in other levels (BRUZZONE & CARLIN, 2006). This results from varying landcover types and therefore also varying sizes

(JOHNSON & XIE, 2011). However, each object on a level is hierarchically linked with other objects on the level above and below (BRUZZONE & CARLIN, 2006). Additionally the usage of multi-scale segmentation enables a more precise distinction of objects in heterogeneous scenes compared to the usage of a single segmentation scale (JOHNSON & XIE, 2011; JOHNSON & XIE, 2013). Furthermore the utilization of a multi-scale approach aims for avoiding over-segmentation or under-segmentation, which have influences on the subsequent classification accuracy (decreases with over- and under-segmentation) (LIU & XIA, 2010; DORREN ET AL., 2003; KIM ET AL., 2009).
Nevertheless the process of aggregating various segmentation levels requires experience-based knowledge in manual interpretation and feature delineation (LANG & BLASCHKE, 2003) for the determination of appropriate segmentation levels. According to JOHNSON & XIE (2011) a high-quality multi-scale segmentation can be done by a) visually inspection and selection of segmentation levels to perform multi-level segmentation by the user, by b) supervised methods, which compares segmentation levels by involving references produced by the user or ground truth (ZHANG, 1997), or by c) unsupervised methods which includes quality criteria to score and rank the segmentation levels (CHABRIER ET AL., 2006).
DRAGUT ET AL. (2010) developed a tool for the automated estimation of scale parameters (ESP-tool) for the multi-scale segmentation in the eCognition® software. This tool is based on a bottom-up multiresolution segmentation by a constantly increasing scale factor (scale-parameter) until a local variance value is reached (DRAGUT ET AL., 2014). The successor enables the implementation of multi-spectral data as opposed to the ESP-tool (which only works on single layers) developed 2010 (DRAGUT ET AL., 2014), however image layer weighting is not supported. Thus this tool could be not used in this study.

In conclusion, multi-scale segmentation is the combination of various segmentation scales from a single resolution remotely sensed image to a final segmentation and avoids over- and under-segmentation. The multi-scale segmentation procedure in this study relies on the computed nDSM and the mosaiced optical data (RapidEye) for the entire study area.

5.2.1 Determination of appropriate Segmentation Scale

As mentioned in the previous chapter urban structure types are differing in their size and necessitated a multi-scale segmentation as proposed by ESCH ET AL. (2008). In this process distinctive segments were compared and used for the generation of multiple segmentation scales. Generally in region-growing segmentations user-defined parameter settings are required. The selection of appropriate parameters to obtain qualitative high segmentation results is a challenging task (ESPINDOLA ET AL., 2006) and does often imply a time-consuming trial-and error process (ZHANG ET AL., 2010). Consequently, some studies were concerned with the evaluation of segmentations (STEIN & DE BEURS, 2005; CHABRIER ET AL., 2006; ESPINDOLA ET AL., 2006; KIM ET AL., 2008, 2009; RADOUX & DEFOURNY, 2008). GAO ET AL. (2007) used the objective function proposed by ESPINDOLA ET AL. (2006) and showed the efficiency for the determination of the best segmentation scales. This approach based on the assumption that an optimal segmentation maximizes intrasegment homogeneity and intersegment heterogeneity, which are components for the measure of intrasegment variance (v) and Moran's I (I) (GEIß ET AL., 2014d). Accordingly in this study the procedure of computing a multi-scale segmentation proposed by ESCH ET AL. (2008) followed by the objective function by ESPINDOLA ET AL. (2006) for the finding of the best segmentation scale was utilized. The entire process is schematically illustrated in the flowchart (cf. figure 22) below. Additionally the fundamental processing steps are illustrated as subsets at the end of the optimized procedure in figure 26.

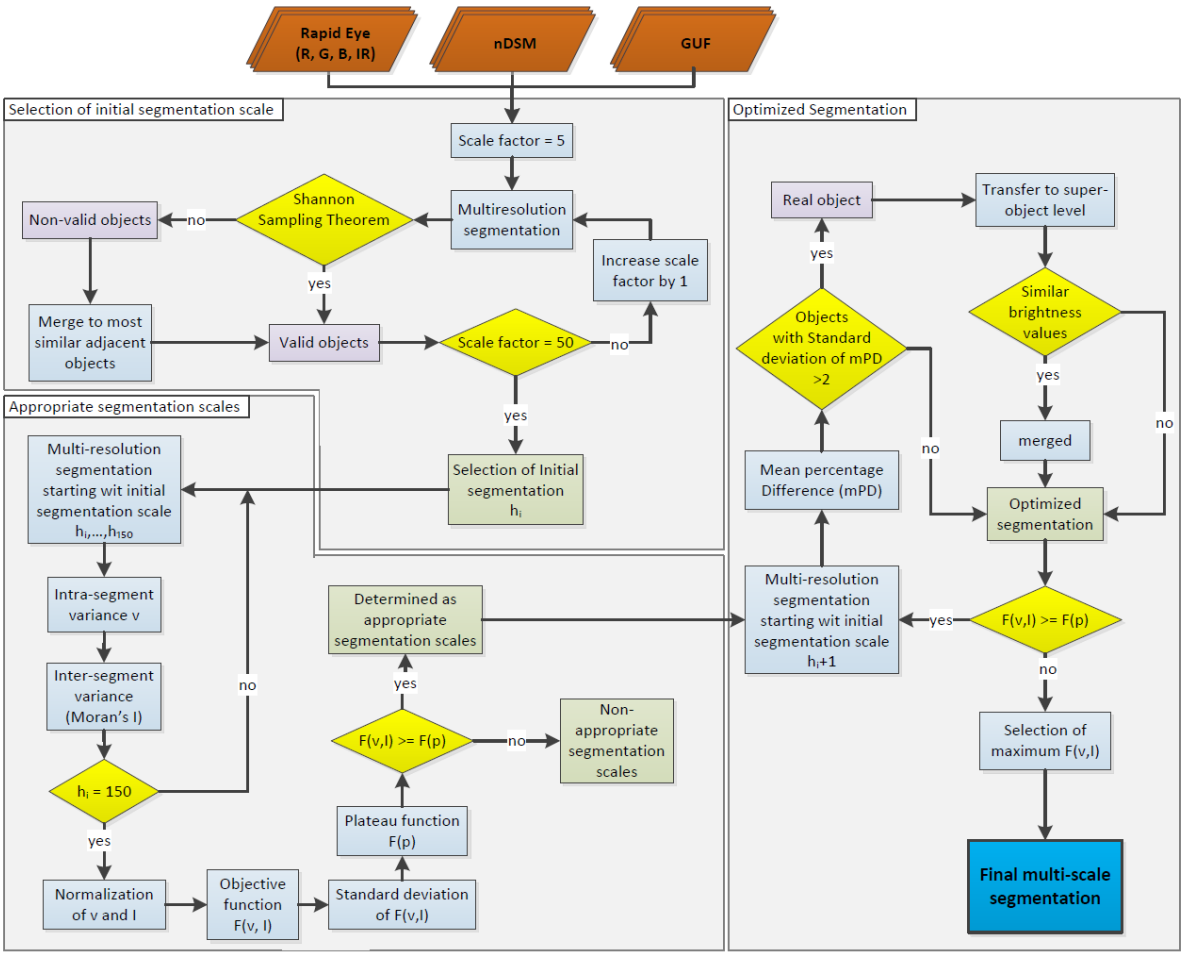

Figure 22: *Flowchart of the multi-scale segmentation process.*

As mentioned in the previous chapter the multi-scale segmentation was implemented on the mosaiced optical data, the nDSM and supplementary bounded by the GUF for a segmentation of only urban areas. Due to the fact that the optical data and the height information (nDSM) were used to compute the segmentation both data sets should be available with the same pixel size and should exactly fit on top of each other to avoid the generation of sliver polygons (cf. chapter 4.2). Sliver polygons are defined as small slim polygons typically occurred along the borders of polygons (ESRI, N.D.) due to dissimilar levels of data and are manipulating the topology. Therefore, sliver polygons should be avoided. Thus the nDSM dataset was resized (as mentioned in chapter 4.2) to the same pixel size as the optical data (5m).

The entire process of determining the initial multiresolution segmentation scale based on constant parameter settings of 0.7 for the shape heterogeneity criterion and 0.5 for the compactness heterogeneity criterion. These parameter setting was selected due to

the fact that buildings and other man-made structures have distinct size and shape characteristics (i.e., more emphasize was put on the shape parameter than on compactness) rather than grey-value heterogeneity. To ensure the transferability at the best possible rate for other multi-spectral data sets the most standard bands red, green, blue, and near-infrared (red-edge was skipped) were used for the segmentation and also for the succeeding feature calculation (cf. chapter 6). Even the red edge band is primarily used for vegetation analysis and so not actually relevant for this study. The weighting of the image layer bands (red, green, blue, near-infrared, and nDSM) relies on an empirical process of delineating meaningful segmented objects.

During the process of generating multiple segmentations the segments of each scale were verified to fulfill the Shannon sampling theorem. This defines that “an object should be of the order of one tenth of the dimension of the sampling scheme - the pixel - in order to ensure that it will be completely independent of its random position and its orientation relative to the sampling scheme” (BLASCHKE, 2010, pp. 3). According to that an object has to consist of at least ten pixels to represent a valid object in terms of size and five pixels in terms of width:

$$val_{ob} = \begin{cases} \dfrac{\sqrt{a_{ob}}}{\dfrac{g}{10}}, & S < 3 \\ \dfrac{w_{ob}}{\dfrac{g}{5}}, & S \geq 3 \end{cases}$$

with a_{ob} defining the area of the object, the geometric resolution of the image is determined by g, w_{ob} represents the object width and S is a shape complexity index. S is calculated as the perimeter to boundary ratio:

$$S = \frac{P}{2 \cdot r \cdot \pi}, \qquad r = \sqrt{\frac{a_{ob}}{\pi}}$$

where P depicts the object perimeter, a_{ob} the area of the object and r the radius of a circle with the same surface area. The shape complexity index S was set to 3 to distinguish compact and narrow/ long objects as proposed by HENGL (2006).

The series of segmentations for detecting the initial segmentation scale ranged between 5 and 50 with an interval of 1. For each segmentation the number of objects,

the number of non-valid objects, the percentage of non-valid objects towards the number of objects, and the delta value of two consecutive segmentation scales were calculated (cf. appendix A). Thereby the number of non-valid objects represents the amount of objects which did not fulfill the Shannon sampling theorem. The percentage of non-valid objects represents the share of non-valid objects against the total number of objects representing the urban areas (classified as GUF). The percentage of non-valid objects (γ) from the initial scale h_i is calculated by

$$\gamma_{h_i} = \frac{\sum_{i=0}^{n} \mu_{h_i} \cdot 100}{\sum_n \varphi_{h_i}}$$

where μ is a non-valid object of h_i, and φ the total number of objects from h_i. Additionally required for the determination of the appropriate starting scale constitutes the delta, which is the difference of the number of non-valid objects between two consecutive segmentation scales. This is specified by

$$\Delta\delta_{h_i} = \gamma_{h_i} - \gamma_{h_{i+1}}.$$

The segmentation scale which entails a relatively small proportion of non-valid objects and a local maximum of non-valid objects with respect to adjacent segmentation scales was selected as initial starting scale for the subsequent procedure. This condition was satisfied for $h=24$, as can be seen in figure 23.

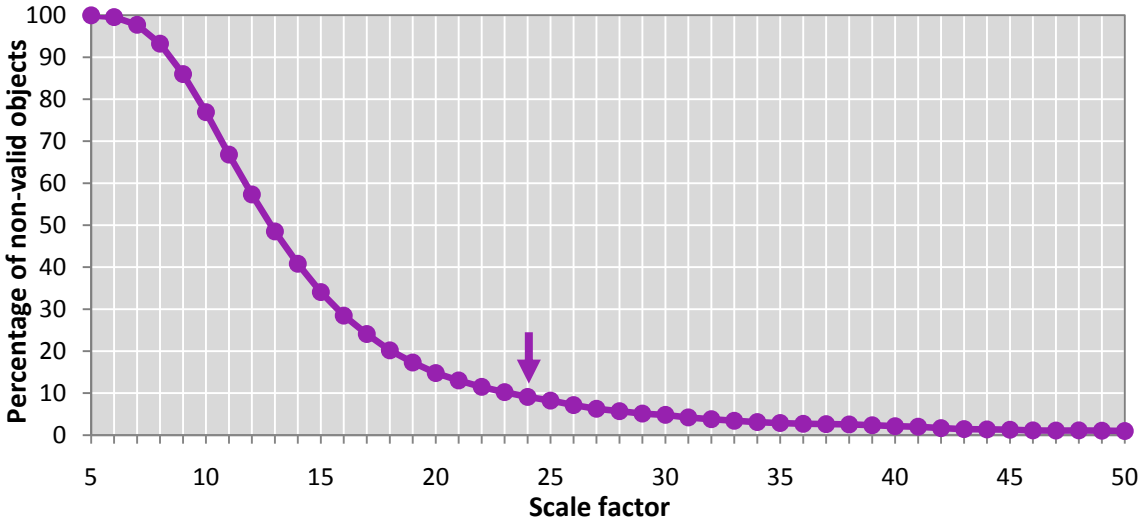

Figure 23: *Determination of initial segmenation scale (marked by the arrow).*

In the following ESPINDOLA ET AL.'s (2006) proposed objectiv function is implemented. The function assumes that a maximizing intrasegment homogeneity and intersegment heterogeneity represents the optimal segmentation scale. For that purpose multiple segmentation scales starting with the determined initial segmentation $h=24$ to a scale factor of 150 with at an interval of 1 were calculated. The objective function is composed by measuring the intrasegment variance v and the Moran's I (I). Therefore the intrasegment variance is a global measure over the entire scene weighted by the area of each segment. Thus larger regions have more influence than smaller ones and avoid therefore instabilities caused by small segments (ESPINDOLA ET AL., 2006). The intrasegment variance was calculated by the formula:

$$\mathrm{v} = \frac{\sum_{i=1}^{n} a_i \mathrm{v}_i}{\sum_{i=1}^{n} a_i}$$

where a_i represents the area of segment i and v_i is its variance. In the process the variance is computed with the spectral brightness values calculated from the optical band information of red, green, blue and near-infrared and additionally the building height information derived from the nDSM.

Before measuring the intersegment heterogeneity all scales were exported as shapefiles with the information of the brightness value and the intrasegment variance of each segment. The further calculation of the Moran's I, which is a spatial autocorrelation index (FOTHERINGHAM ET AL., 2000) was implemented with the software ArcGIS. The Moran's I is determined by

$$I = \frac{N}{\sum_i \sum_j w_{ij}} \cdot \frac{\sum_i \sum_j w_{ij} (X_i - \bar{X})(X_j - \bar{X})}{\sum_i (X_i - \bar{X})^2}$$

where N represents the total number of segments indexed by i and j, X defines the brightness value from the before mentioned spectral bands for a segment, and $\bar{X}$ the mean brightness of all segments. In addition w_{ij} defines the spatial weighting of spatial adjacency of the segments i and j. Thus w_{ij} is defined as:

$$w_{ij} = \begin{cases} 1, & if\ segment\ i\ and\ segment\ j\ are\ adjacent\ neighbour\ segments \\ 0, & else. \end{cases}$$

The Moran's I measures the divergence from the averaged mean brightness values of each segment to the averaged mean values of its neighboring segments. For the

image segmentation a high intersegment heterogeneity and therefore low Moran's I values (low spatial autocorrelation) are preferable which means adjacent segments are statistically distinguishable (JOHNSON & XIE, 2011; ESPINDOLA ET AL., 2006).
The proposed objective function was calculated for all scales h_i by using the intrasegment variance and the Moran's I calculation and is defined as:

$$F(\mathrm{v}, I) = F(\mathrm{v}) + F(I)$$

Where $F(v)$ an $F(I)$ represent normalized functions specified by:

$$F(x) = \frac{X_{max} - X}{X_{max} - X_{min}}$$

Where X_{max} and X_{min} are the maximum and minimum value of the intrasegment variance or the Moran's I over the range of all calculated scales h_i. With the normalization of the functions the Moran's I and intrasegment variance were rescaled to range between 0 and 1. The optimal initial multiresolution segmentation is represented by the maximum value (identified for $h_{i=24}$) of the objective function $F(\mathrm{v}, I)$ ranging over all computed scales h_i and represents a balance between over- and under-segmentation (ESPINDOLA ET AL., 2006). In figure 24 the trend of the objective function is shown and additionally the single calucation steps for all segmentation scales are appended (cf. Appendix B).

However as already mentioned a single-scale segmentation is not efficient to represent homogenous urban structure types. Therefore multiple scales should be combined to a multi-scale segmentation. For that purpose a plateau objective function $F(p)$ defined as

$$F(p) = F(\mathrm{v}, I)_{max} - \sigma$$

introduced by MARTHA ET AL. (2011) was implemented to achieve the best scales for their usage in the process of optimizing the segmentation. $F(\mathrm{v},I)_{max}$ depicts the maximum value of the objective function and σ represents the standard deviation of the objective function for all scales. Scales located above the plateau objective function, which can be obtained from figure 24, were identified as optimal scales for the subsequent optimization procedure (cf. chapter 5.2.2) due to the fact that these scales persist by low internal and high external heterogeneity similar to the maximum value of the objective function. Thus, these scales also fulfill the balance between over- and

under-segmentation. Thereby the optimized procedure was carried out for all scales above the plateau function. From figure 24 the relevant scales from $h=24$ to $h=38$ can be obtained.

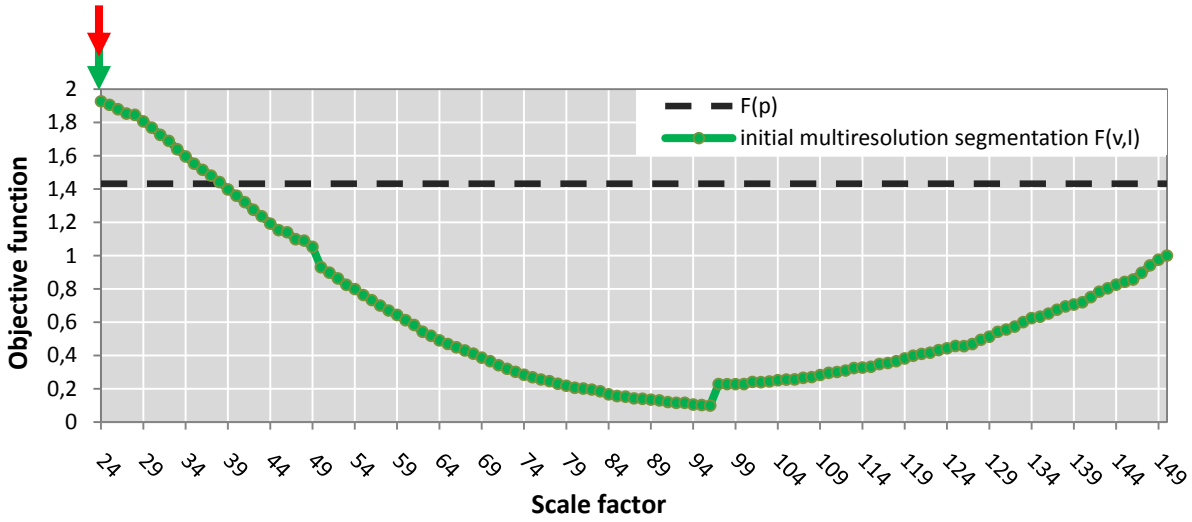

Figure 24: *Objective function for determining the optimal segmenation scale (marked by the green arrow) and plateau objective function F(p) to obtain multiple scales for the multi-scale segmentation with the detected initial scale for the multi-scale segmentation (marked by the red arrow).*

5.2.2 Optimization Strategy

As previously mentioned, the multi-scale segmentation should be used for the delineation of homogenous urban areas by combining the determined segmentation scales selected by the objective function (cf. chapter 5.2.1). Despite that the determined segmentation scales ($h=24$ to $h=38$) represent a balance of over- and under-segmentation, some segments are still over- or under-segmented. In the following the optimization of the initial segmentation scale is presented to enhance the segmentation accuracy by refining the over- and under-segmenation, employing clipping and merging of these segments (ESCH ET AL., 2008). As previously mentioned, the basic processing steps (cf. figure 22) of the computation of a multi-scale segmentation are graphically illustrated by using an example of a study area snippet in figure 26.

This process starts with the initial segmentation h_i, appointed in the preceding chapter and contains the smallest objects in the subsequent multi-scale segmentation. As well as for the determination of the appropriate initial segmentation scale (cf. chapter 5.2.1), also here the Shannon sampling theorem was adopted for the identification of non-valid objects. These were consequently merged to those neigboring object which exibits the minimum difference of the brightness value. Analogous to the calculation of the intrasegment variance, the brightness is based on the intensity values of red, green, blue, near-infrared and the nDSM. Subsequently a second multiresolution segmentation for urban areas atop of L_1 (= segmentation level of initial segmentation) with increased scale factor (by 1) was generated (L_2). In this segmentation hierarchy L_1 represents sub-objects towards L_2 (which is the super-object level of L_1) with different spectral characteristica. A measure for the spectral similarity between sub-objects (L_1) and super-objects (L_2) was calculated by the Mean Percentage Difference (mPD),

$$mPD = \frac{|\bar{X}_{L1} - \bar{X}_{L2}|}{\bar{X}_{L2}}$$

where $\bar{X}$ represents the mean brightness value of the super- (L_2) and sub-objects (L_1). Ensuing from sub-objects exceeding the mPD of all sub-objects by a standard deviation of two and larger, sub-objects are representing “real” sub-objects and were consequently transferred to the super-object level (LU ET AL., 2011). These objects

depict exceedingly distinct characteristics toward the objects with a standard deviation of the mPD lower two, and thus representing meaningful objects (real-objects)

$$real_{ob} = \begin{cases} 1, & mPD > 2\sigma_{mPD} \\ 0, & else. \end{cases}$$

Consequently, the transferred adjacent sub-objects (ob_1 and ob_2) to its super-object level were evaluated regarding their similar mean brightness values ($sim_{ob1,ob2}$), and were merged if they had similar brightness values

$$sim_{ob1,ob2} = \begin{cases} 1, & |Mean_{ob1} - Mean_{ob2}| \leq 5 \\ 0, & \text{else.} \end{cases}$$

For all segmentation scales atop of $F(p)$ (cf.fig. 24) the process of calculating the mPD, generating “real”-objects, transfering these objects to their super-object level and merging them if the $sim_{ob1,ob2}$ condition is fulfilled was repeated. While for each step of increasing the scale factor (by 1) the prior last generated segmentation level will become sub-object level of the newly created segmentation scale.

This process aims to integrate larger and smaller scales of differently scaled objects in one final multi-scale segmentation. Concurrent to the determination of appropriate segmentation scales the generated optimized segmentation levels (multi-scale segmentation) with transferred and partly merged distinctive sub-objects were analyzed by a plateau function, analogous to the chapter before (cf. chapter 5.2.1) and illustrated in figure 25. Analogous to the determination of appropriate segmentation scales the maximum value of the optimized function represents the best balance between over- and under-segmentation (ESPINDOLA ET AL., 2006). Therefore, this combination of several scales specifies the best multi-scale segmentation and defines therefore the final segmentation (in the figure marked with the blue arrow). For the further calculation of possible seismic vulnerability features as outlined in chapter 6 the final multi-scale segmenation was used. The calculated values for generating the optimized segmentation function is listed in the appendix (cf. Appendix C).

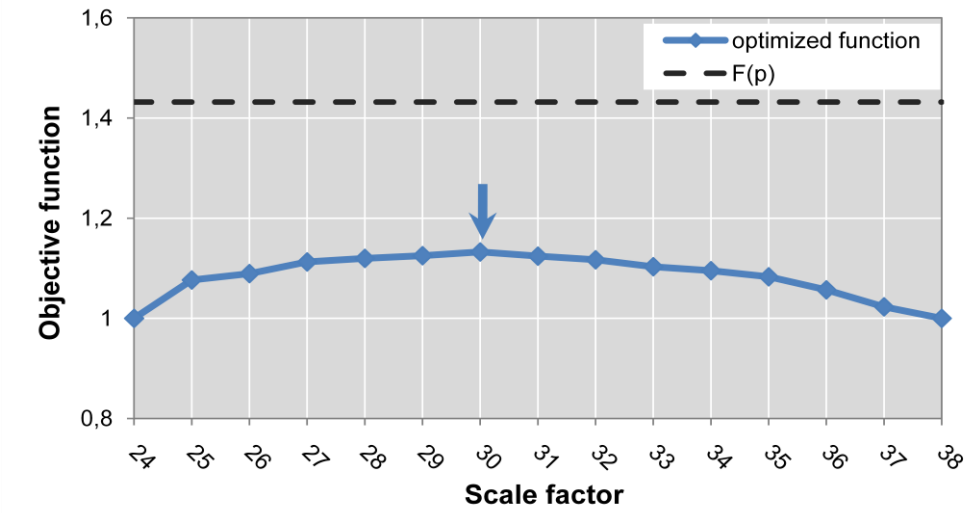

Figure 25: *Optimized function for determining the optimal multi-scale segmenation (marked by the blue arrow).*

A visual inspection of the result reveals a reduced, but already present over-segmentation especially in industrial areas. This may results from the extremely inhomogeneous spectral characteristics (e.g., various colors of roofs). However, in the next chapter this fact was compensated by calculating features with respect to seismic vulnerability on two further segmentation scales.

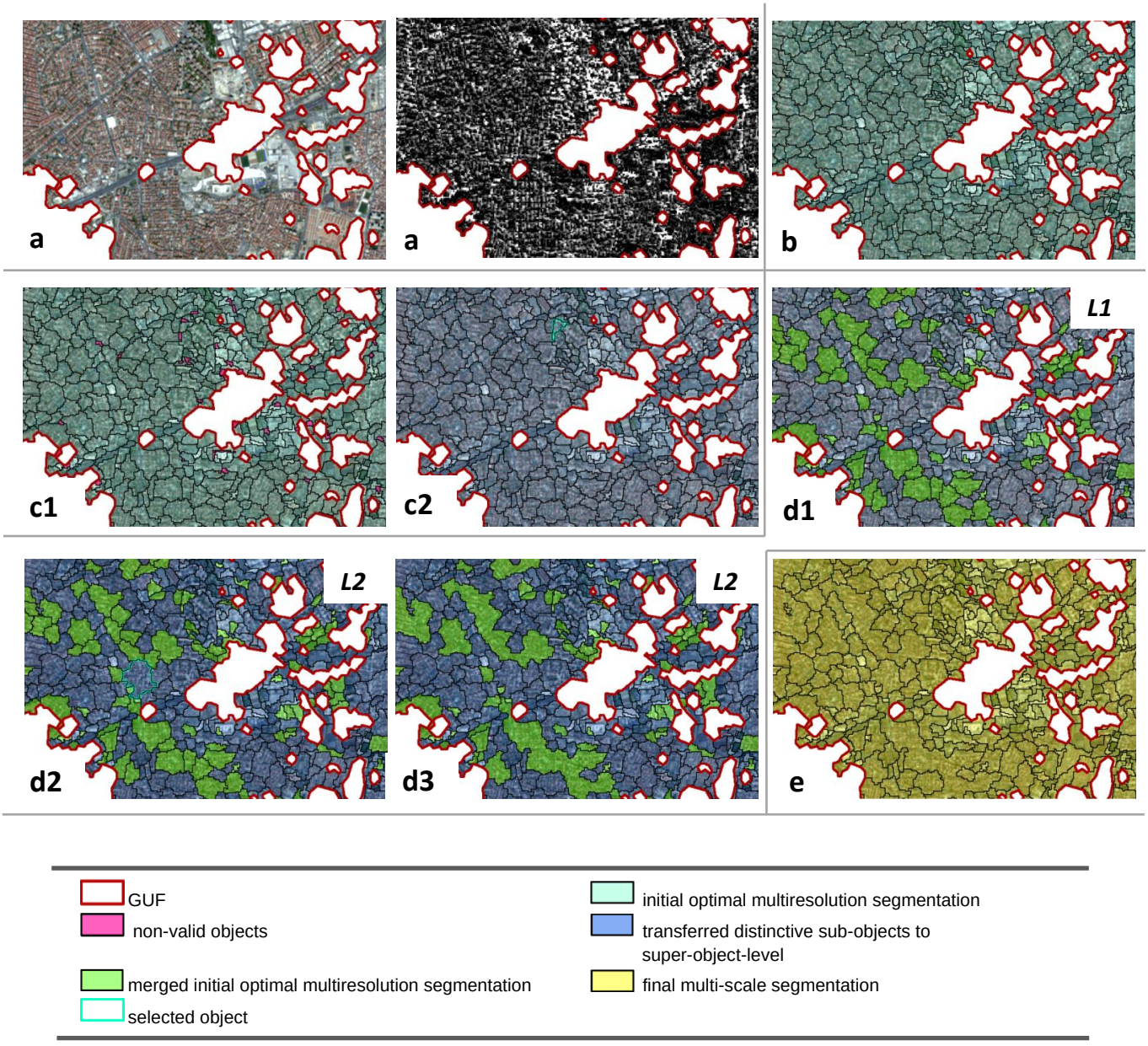

Figure 26: *Fundamental processing steps for the generation of a multi-scale segmentation, initiating with a basic segmentation level based on the GUF and weighted input data sets (a). By analyzing a plateau function the segmentation scales for the optimization procedure (b) were determined. Non-valid objects (pink) identified by considering the Shannon sampling theorem (c1) were merged to their most similar adjacent objects (c2). The optimized procedure includes the determination of distinctive sub-objects (L1) (green) (d1), its transfer to the super-object level (L2) (d2) and its merging to similar adjacent objects (d3). Finally the identification of a final multi-scale segmentation (e) by assessing the objective function of the produced multi-level segmentation results.*

6. Characterization of Seismic Vulnerability Features

To assess the seismic vulnerability of the discriminated homogeneous urban areas, the extraction of several parameters is necessary. In this study parameters which can be derived from the applied remote sensing data (optical data, elevation data, and multi-temporal classification data) were calculated. In the following sections the calculation of these parameters will be explained and listed (cf. table 5).

6.1 Calculation of Seismic Vulnerability Features

In the segmentation section (cf. chapter 5) urban areas with similar building types were grouped to represent homogeneous urban units, assuming that homogeneous urban areas exhibit similar vulnerability characteristics. However, the elevation values as well as its spatial and spectral properties are differing between segments. In relation to the assessment of seismic vulnerability a wide range of parameters (during the further procedure named “features”) based on the optimized segmentation were derived and later on selected upon their relevance to assess seismic vulnerability in Istanbul. With the derived features the seismic vulnerability for each homogeneous urban area should be assessed. In this study the features were derived from the utilized remotely sensed data, mentioned in chapter 3.2.2, 3.2.3.2, and 4. The extraction of useful seismic vulnerability features by remote sensing enables towards in situ inventory a time-saving and cost-effectively rapid assessment of seismic vulnerability. Additionally up-to date inventories especially for large-areas (cf. chapter 3.2.4) were not present and reflect the general status quo. The operability and accuracy are some further advantages for remote sensing data.

Especially the situation in Istanbul (cf. chapter 3.1.1) where the major part of the building stock was illegal built and no reliable plans of buildings exist, required a

balance between thematic detail and feasibility. Therefore remote sensing provide a comprehensive overview of the existing building stock and enables the derivation of features associated with building vulnerability such as height, roof material, year of construction, spatial context, structure type and shape (GEIß & TAUBENBÖCK, 2013). Besides in several studies it was found that the extraction of features from remote sensing data for vulnerability assessment especially in urban areas can be valuable (FRENCH & MUTHUKUMAR, 2006; MÜLLER ET AL., 2006; SARABANDI ET AL., 2008; TAUBENBÖCK ET AL., 2009; BORFECCHIA ET AL., 2010; SAHAR ET AL., 2010; BORZI ET AL., 2011; DEICHMANN ET AL., 2011; WIELAND ET AL., 2012; GEM, 2013; GEIß ET AL., 2014a). These studies are either based on a) combining remote sensing data with inter- and extrapolated in situ surveys or on b) finding correlations of vulnerability curves with extracted features from remotely sensed data (GEIß ET AL., 2014a). However, it should be taken into account that remote sensing data can not supply directly measures about construction type (reinforced, unreinforced), masonry material (except roof material) and construction quality of buildings. However, regarding time, money, and transferability, the consideration of all features influencing the vulnerability of built structures is impracticable. Accordingly, the assessment is done by using main vulnerability features deducible by remote sensing data. Supplementary the literature review has shown that seismic vulnerability assessment can also be done by utilizing remotely sensed data. In this study the calculated features are mostly consistent on the study by GEIß ET AL. (2014a) where the potential of remotely sensed data for the assessment of seismic vulnerability on single buildings were evaluated.

In the following sections features related to seismic vulnerability by available remote sensing data for the optimized segmentation were introduced and extracted. The sub-chapters are split into the utilized remote sensing data (optical = RapidEye data, nDSM, and ancillary geo-information = multi-temporal Landsat classification). Furthermore, equivalent to the optimized segmentation the same features were computed on two separable larger multi-resolution segmentation scales (h=80 and h=120) due to compensate remaining over- and under-segmentation (especially in industrial areas) of the optimized multi-scale segmentation. The idea of using super-segmented information has also been exploited in BRUZZONE ET AL. (2006) and has shown that those features can enhance the classification accuracy. However, both multi-resolution segmentations did not imply the optimization procedure (cf. chapter 5.2.2) which leads to the fact that these segmentation levels represent super-objects as well as sub-objects in respect to the optimized segmentation. In figure 27 the applied

segmentation scales (optimized segmentation, $h=80$, and $h=120$) and the characteristics of $h=80$ and $h=120$ to be super- and sub-objects towards the optimized segmentation scale are displayed.

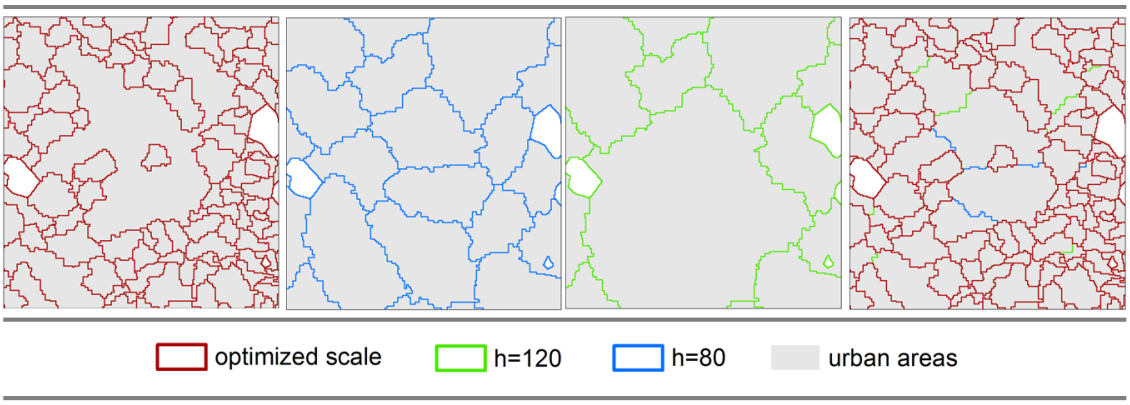

Figure 27: *Snippets of the utilized segmentation scales.*

In the following sub-chapters the calculation of seismic vulnerability features derived from optical data (cf. chapter 6.1.1), nDSM data (cf. chapter 6.1.2), and from the Landsat classification (cf. chapter 6.1.3) for the three segmentation scales were outlined.

The allocation of the calculated features on larger scale to the objects of the optimized segmentation necessitated some further transformation steps. At this, the objects of $h=80$ and $h=120$ with its calculated features (cf. chapter 6.1.1, 6.1.2., 6.1.3) were used for a further splitting into smaller objects related to the optimized segmentation to produce sub-objects with the assigned features from their respective scales ($h=80$ and $h=120$). Afterwards the sub-objects were transferred as points for their averaging and assignment (spatial join) to the optimized segmentation scale. Thus the optimized segmentation scale is finally composed of the features derived for this scale as well as the features from $h=80$ and $h=120$. Accordingly, each homogeneous urban area is represented by a 198-dimensional feature vector.

6.1.1 Seismic Vulnerability Features derived from Optical Data

This chapter describes the calculation of features derivable from optical remote sensing data (by using the eCognition software). The derivation of vulnerability features were carried out on the optimized multi-scale segmentation bounded by the GUF, as well as for the segmentation scales $h=80$ and $h=120$ as mentioned before (cf. chapter 6.1).

Due to the complex urban morphology of Istanbul the entire study area was divided in irregularly shaped spatial units (segments) instead of uniform segments. Therefore these segments depict were most qualified for the calculation of vulnerability related features of homogeneous urban areas. In general the segments represent similar aggregated single buildings, for which it is assumed that they comprise similar seismic vulnerability. The mosaiced multispectral remote sensing data (RapidEye scenes) was applied for the calculation of several statistical values and texture measures similar to GEIß ET AL. (2014a). The spectral information on this scale can be used for the distinction of diverse urban areas (HEROLD ET AL., 2003; STEINIGER ET AL., 2008).
In table 5 the calculated features derived from optical data, nDSM, and multi-temporal Landsat classification, as outlined in the following were summed up. As previously mentioned (cf. chapter 5.2.1) the spectral bands red, green, blue, and near-infrared represent the general standard in multispectral remote sensing. Those were used for the feature calculation consistent to the segmentation procedure which based on these spectral bands beside of the nDSM values.

Initially some common basic descriptive statistic parameters like the measures of central tendency and measures of spread for the spectral bands R, G, B, and NIR were calculated. The measures of central tendency comprises the arithmetic mean which is defined as

$$\bar{x} = \frac{1}{n}\sum_{i=1}^{n} x_{\mathrm{i}} = \frac{x_1 + x_2 + \ldots + x_n}{n}$$

where the pixels x_i of an analyzed segment were summed up and divided by the number of involved pixels n. In addition, the median (50th percentile) of and ordered dataset (i.e., from low to high values) specified by

$$x_{med} = \begin{cases} \frac{x_{n+1}}{2}, & for\ n\ uneven\ number \\ \frac{1}{2}\left(x_{\frac{n}{2}} + x_{\frac{n}{2}+1}\right), & for\ n\ even\ number \end{cases}$$

were calculated; where x represents the pixel value of the total number of pixels n. Thus the median represents the middle of the dataset, if n is an uneven number. If n is an even number the median delineates the mean of the dataset. In addition the mean brightness was calculated, which represents the arithmetically averaged intensity of the spectral bands R, G, B, and NIR. Furthermore, for each segment the maximum difference between the mean values of the spectral bands were derived. Additionally, the minimum and maximum values of the embedded pixels in an image object (segment) were extracted.

Variance, standard deviation, range, and interquartile range for the spectral bands R, G, B, and NIR were derived as measures of spread. At that, the variance is a measure for the degree of spread around the mean value, defined by

$$\sigma^2 = \frac{1}{n}\sum_{i=1}^{n}(x_i - \bar{x})^2$$

with n representing the number of pixel of a segment is based. The calculation of standard deviation for each of the spectral values is given by

$$\sigma = \sqrt{\sigma^2} = \sqrt{\frac{1}{n}\sum_{i=1}^{n}(x_i - \bar{x})^2}$$

where the standard deviation is determined as the square root of the variance. The measures of mean and standard deviation of spectral bands were primarily used to point out spectral dissimilarities of different urban structures (GEIß ET AL., 2014a).

For the calculation of the range, the minimum pixel value was subtracted from the maximum pixel value

$$R_{(max\ -\min)} = x_{max} - x_{min}$$

where x_{max} and x_{min} are units of the measures of tendency and were calculated before.

Finally the calculation of measures of spread, the difference between the upper (3rd quartile) and lower quartiles (1st quartile), defined as interquartile range was ascertained via

$$IQR = Q_{.75} - Q_{.25}$$

where $Q_{.75}$ constitutes the upper quartile (75% of the data set) and $Q_{.25}$ the lower quartile (25% of the data set). Thus the interquartile range comprises the 50% of the data set.

Beside the calculation of statistical features some texture measures on the brightness value (compounded by the spectral values of R, G, B, and NIR) using the grey level co-occurrence matrix (GLCM) (HARALICK ET AL., 1973) were calculated. Texture measures can be used to distinguish urban structures (HEROLD ET AL., 2003). Furthermore, texture measures were regularly used to overcome lacks of spectral information (PACIFICI ET AL., 2009). The calculation of GLCM texture features list the occurrence of various gray levels (intensity of each pixel) in tabular form and gives information about the variations of spectral intensity in an image (ECHOVIEW, 2014). The calculated GLCM features were:

- *Homogeneity*
- *Contrast*
- *Dissimilarity*
- *Entropy*
- *Angular 2nd Moment (= Energy)*
- *Mean*
- *Standard Deviation*
- *Correlation.*

In the following a general short description of the eight GLCM features is given:

- *Homogeneity: Measure for the closeness of distributed GLCM elements to the diagonal elements.*
- *Contrast: Measure for the intensity contrast (difference between lowest and highest pixel value) by exponentially weighting of the diagonal (similar to Dissimilarity).*

- *Dissimilarity: Measure for the intensity contrast by linear weighting of the diagonal (similar to Contrast).*
- *Entropy: Measure of randomness of the elements.*
- *Angular 2nd Moment (Energy): Measure for the uniformity of elements.*
- *Mean: Pixels were weighted by the frequency of their occurrence in combination with a certain adjacent pixel value (TRIMBLE, 2011).*
- *Standard Deviation: Measures the dispersion of pixel values around the mean value (similar to Contrast and Dissimilarity) (TRIMBLE, 2011).*
- *Correlation: Measurement for linear dependencies of pixels (correlation between rows and columns).*

For more details about GLCM texture it is referred to the literature (HARALICK ET AL., 1973) at this point.

The next group of features, which were derived from optical remote sensing data focuses on the involved amount of vegetation in each homogeneous urban area as a proxy to distinguish different urban structures (e.g., industrial structures, residential structures). Its relevance as important feature for assessing the seismic vulnerability in Istanbul was examined in the chapter dealing with the selection of appropriate features (cf. chapter 6.2). The vegetation was determined on pixel-level (i.e., sub-object level) by using the Normalized Differenced Vegetation Index (NDVI) introduced by ROUSE ET AL. (1974) as

$$NDVI = \frac{NIR - RED}{NIR + RED}$$

where NIR and RED characterize the reflectance of the spectral bands near-infrared (NIR) and red. In this analysis all pixels with an $NDVI \geq 0.3$ were interpreted as vegetation. Afterwards the proportion of vegetated and non-vegetated areas was calculated by

$$\alpha = \frac{\sum_{i=0}^{n} p_i \cdot 100}{\sum_{i=1}^{n} g_i}$$

where p_i represents a pixel with $NDVI \geq 0.3$ (i.e., vegetation) on the pixel-level and g_i the total number of pixels embedded in on image object.

Features with assumed relation to seismic vulnerability were additionally derived from the nDSM data as outlined in the subsequent chapter.

6.1.2 Seismic Vulnerability Features derived from nDSM

Building heights have an effect on the seismic building vulnerability (FEMA310,1998; IEE NICEE, 2004). Therefore, the nDSM data were used to extract supplementary possible vulnerability parameters.

The feature type calculation from nDSM data were mostly similar to the features derived from optical data. Descriptive statistical parameters like the measures of central tendency and measures of spread were derived for the nDSM values, where high nDSM values characterize high objects and low brightness values flat objects. Similar to the feature calculation of optical remote sensing data the texture measures were calculated (cf. chapter 6.1.1). As opposed to the calculation of the proportion of vegetated features by using multispectral information, the nDSM provides information about the elevation of surface' objects (e.g., buildings, bridges, trees etc.) which can be similarly used to derive the amount of buildings with a certain height in homogeneous urban areas (segments). This type of feature calculation based on the analysis of embedded single pixel values (i.e., pixel-level). The amount of elevated objects gave a measure of covered areas (in percentage) with objects over a defined threshold (from a certain object height). Uniformly to the extraction of building height information (nDSM calculation), mentioned in chapter 4, the threshold for identifying elevated objects (OBJ) on pixel-level were set to 2.6 meter, assumed that buildings have a minimum height of 2.6 m. This threshold enables the separation between ground and elevated object. Therefore the proportion of elevated objects in the segments were extracted by

$$\beta = \frac{\sum_{i=0}^{n} p_i \cdot 100}{\sum_{i=1}^{n} g_i}$$

where p_i represents a pixel with a $mean_{nDSM} \geq 2.6\ m$ (i.e., elevated object) on the pixel-level and g_i the total number of pixels embedded in one image object. Beyond, the calculation of the amount of elevated objects the highest object of each segment was extracted by exploring the maximum nDSM value on pixel-level. The same was done for the analysis of the flattest object in the image objects by extracting the minimum nDSM value atop of the threshold for the identification of elevated objects. In addition, the average building heights of all elevated objects were derived as an additional feature by calculating the mean value of all elevated objects. Furthermore, the range of the elevated objects which was calculated by the difference of the

maximum elevated object (i.e., highest elevated object) and the lowest (i.e., minimum elevated object) object of each segment was computed. Afterwards the standard deviation and the variance of the elevated objects were generated as a further possible seismic vulnerability feature derivable from altitude values.

In table 5 an overview of the calculated features derived from optical data (cf. chapter 6.1.1), elevation data, and ancillary geo-information (cf. chapter 6.1.3) is given.

Based on / Feature type	Optical Data	Elevation Data (nDSM)	Ancillary geo-information
Measures of central tendency	$Mean_{R,G,B,NIR}$ $Mean_{brightness}$ $Mean_{max.\ diff}$ $Median_{R,G,B,NIR}$	$Mean_{nDSM}$ $Median_{nDSM}$	-
Measures of spread	$Variance_{R,G,B,NIR}$ $Standard\ Deviation_{R,G,B,NIR}$ $Minimum_{R,G,B,NIR}$ $Maximum_{R,G,B,NIR}$ $Range_{R,G,B,NIR}$ $Interquartile\ Range_{R,G,B,NIR}$	$Variance_{nDSM}$ $Standard\ Deviation_{nDSM}$ $Minimum_{nDSM}$ $Maximum_{nDSM}$ $Range_{nDSM}$ $Interquartile\ Range_{nDSM}$	-
Texture (GLCM)	$GLCM\ Homogeneity_{brightness}$ $GLCM\ Contrast_{brightness}$ $GLCM\ Dissimilarity_{brightness}$ $GLCM\ Entropy_{brightness}$ $GLCM\ Angular\ 2nd\ Moment_{brightness}$ $GLCM\ Mean_{brightness}$ $GLCM\ Standard\ Deviation_{brightness}$ $GLCM\ Correlation_{brightness}$	$GLCM\ Homogeneity_{nDSM}$ $GLCM\ Contrast_{nDSM}$ $GLCM\ Dissimilarity_{nDSM}$ $GLCM\ Entropy_{nDSM}$ $GLCM\ Angular\ 2nd\ Moment_{nDSM}$ $GLCM\ Mean_{nDSM}$ $GLCM\ Standard\ Deviation_{nDSM}$ $GLCM\ Correlation_{nDSM}$	-
Vegetated Objects (Pixel-Level)	$Proportion\ of\ Vegetation_{NDVI\ \geq 0.3}$	-	-
Elevated Objects (Pixel-Level)	-	$Proportion\ of\ Elevated\ Objects_{nDSM\ >26}$ $Maximum\ of\ Elevated\ Objects_{nDSM\ >26}$ $Minimum\ of\ Elevated\ Objects_{nDSM\ >26}$ $Mean\ of\ Elevated\ Objects_{nDSM\ >26}$ $Range\ of\ Elevated\ Objects_{nDSM\ >26}$ $Standard\ Devation\ of\ Elevated\ Objects_{nDSM\ >26}$ $Variance\ of\ Elevated\ Objects_{nDSM\ >26}$	-
Period of Construction	-	-	*unknown* *until 1975* *1975 – 1987* *1987 - 2000*

Table 5: *Calculated features derived from remotely sensed data on the optimized segmentation scale, h=80, and h=12.*

6.1.3 Seismic Vulnerability Features derived from Landsat Classification

Another derived feature related to seismic vulnerability depicts the construction phase of the building stock. For this analysis supplementary data such as the available multi-temporal Landsat classification (TAUBENBÖCK ET AL., 2009) were necessary (cf. chapter 3.2.3.2). The Landsat classification provides a time series from three different time steps, 1975, 1987, and 2000. For each of them urban areas were classified. So the extension of the city can be investigated over these time frames. However, this data can not give information about new renovated or rebuild constructions if its location was already assigned to a certain construction phase. Furthermore, it should be taken into account that the Landsat classification features a geometric resolution of 30 meters. Nevertheless, the Landsat classification can quote the general year of construction of certain homogeneous urban areas. Due to the uncertainties of this ancillary information this feature was leave out of consideration in the feature selection (cf. chapter 6.2) and model learning procedure (cf. chapter 7.2.1, 7.2.2, and 7.2.3). Albeit, this information was added as further information to the results of seismic vulnerability assessment (cf. chapter 8.2 and 8.3). Furthermore, this feature is represented as a categorical character in distinction to all other derived vulnerability features which are characterized by numerical characters. Therefore, this feature could not be used for the classification procedure regarding its affect to the classification result.

The analysis and assignment of the general construction phase to its homogeneous urban areas on the three different segmentation scales was carried out with the software eCognition. At this, the segments were identified as been built before 1975, between 1975 and 1987, or between 1987 and 2000, by the dominated area of the respective class of the Landsat classification. Objects which could not obvious assigned to a class due to the same portion of a Landsat class were allocated to this constructions phase which is dominated in adjacent objects. Furthermore, objects were classified as unknown construction phase if there is no information from the Landsat classification (unclassified) or the proportion of Landsat classes is lower than the proportion of unclassified areas. This results from the dissimilar Landsat classification extent and the extent of the study area. Objects classified as unknown construction phase primarily occurred in marginal areas where since 2000 new buildings were built

(segmentation based on the RapidEye (2009) and TanDEM-X data (2010-2012)) and in the northern portion from the study area where no Landsat classification was available. In the figure below (figure 28) the recognized construction phase for the optimized segmentation scale is displayed.

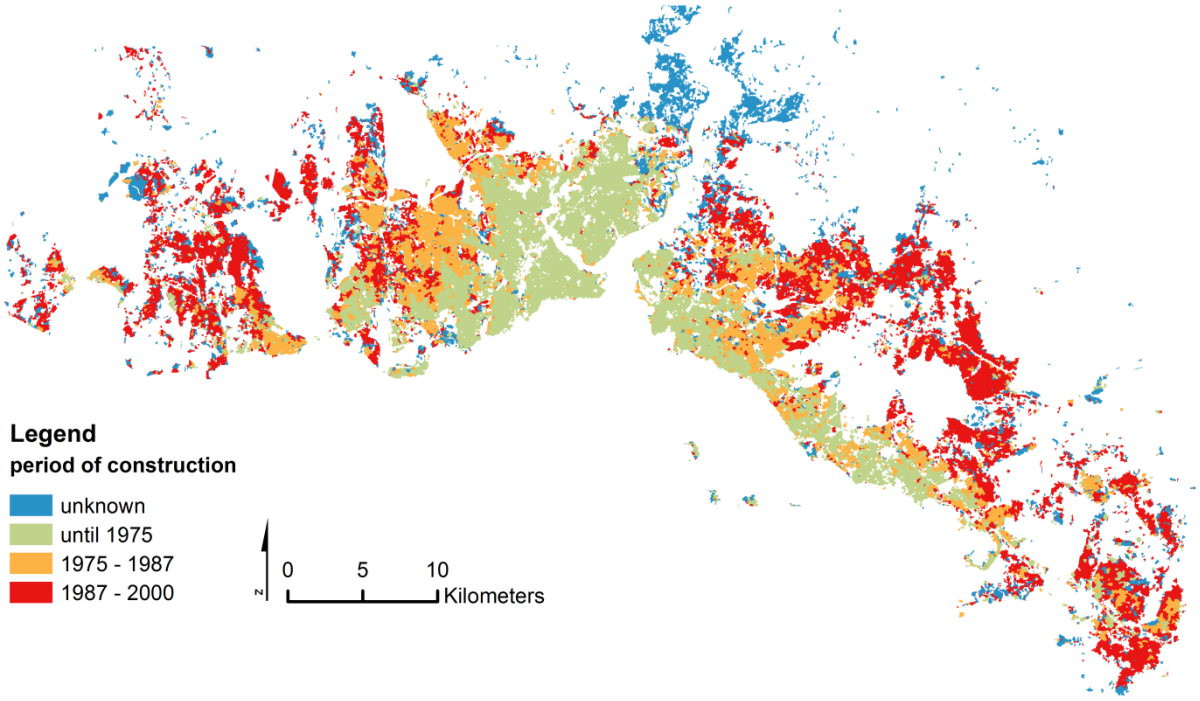

Figure 28: *Identified construction phase for the optimized segmentation.*

6.2 Evaluation and Selection of Seismic Vulnerability Features

This chapter describes the procedure of selecting features to create various feature sets which were used for the further process of regression and classification analysis with SVM (cf. chapter 7) to assess seismic vulnerability. Hence, the feature selection was applied separately with respect to the three utilized learning techniques (SVR, C-SVM, OC-SVM), expounded in the following chapter (cf. chapter 7). Fundamentally the feature selection followed quantitative and qualitative criterions. The quantitative selection of features based on the underlying thematic remotely sensed data (optical and nDSM) and the levels of segmentation (optimized segmentation, $h=80$, and $h=120$). Six qualitatively selected feature sets were compiled. Initially feature sets were built by using all features from all segmentation levels derived from optical data, all from elevated data (nDSM), and all features from optical and elevated data. After that, the same feature sets were generated, but at this time only for features from the optimized segmentation scale (optical, elevated, and all). These feature sets were used to evaluate and quantify the different remote sensing data on which the feature calculation based on, as well as the segmentation levels.

The quantitatively feature selection was used to avoid redundant and strong correlated features, which frequently occurs in data sets composed of a large number of features. Additionally, this feature selection strategy was applied to avoid “Hughes phenomenon” which stated that with increasing feature vector dimensionality the accuracy decreases (HUGHES, 1968). For reducing the dimensionality of the feature sets two filtering methods for selecting appropriate features with respect to the utilized learning approaches (SVR, C-SVM, and OC-SVM; cf. chapter7.2.1, 7.2.2, and 7.2.3) an the respectively given sample data were conducted. These filtering procedures were realized within the *Waikato environment for knowledge analysis* software (WEKA). WEKA is an open source java-programmed software, developed for machine learning techniques and data mining processes. For identifying the most suitable features in terms of the SVM approach (SVR, C-SVM, and OC-SVM), the respective entire training data sets (sample data set) with the respective labeled instances were used. In chapter 7.2.1, 7.2.2, and 7.2.3 the respective sample data sets are introduced for the distinct SVM approaches.

The first applied filtering method is called 'Correlation-based Feature Selection' (CFS), proposed by HALL (1999). This method relies on detecting the most uncorrelated features from a matrix of feature classes using a best first search algorithm. Thereby, the correlation between each feature X and the class Y is measured within a range of [0,1] by

$$r_{X,Y} = 2.0 \times \left[\frac{gain}{H(Y)+H(X)}\right].$$

Where $gain$ is a symmetrical measure between X and Y and is defined by $H(X) + H(Y) - H(X,Y)$, where $H(X)$ represents the entropy of the feature (HALL, 1999; LIU ET AL., 2002). To assign a numerical score, which indicates the value of a subset of features S, a measure

$$M_S = \frac{kr_{cf}}{\sqrt{k + k(k-1)r_{ff}}}$$

is computed. Where k represents the number of features of S, r_{cf} the mean feature-class correlation, and r_{ff} the average feature-feature inter-correlation. Therefore, CFS analyzes each feature of the entire feature set independently. At this, the numerator is an indicator of how predictive a feature set is. The denominator gives information about the redundancies of the feature set. Subsequently, features with a low feature-class correlation and features with a high feature-feature correlation (high redundancy) were identified as inappropriate features. The stopping criterion parameter was set to five to consecutive fully expanded non-improving subsets before the search is completed. Hence, the outcomes offer a suitable feature subset (with the highest M_S during the search) for the respective regression or classification technique.

The second applied filtering method enables the ranking of features according to adjacent instances. This strategy is implemented in the Relief-F approach from KONONENKO (1994). It works with the assumption, that useful features representing a certain class should have similar values, but differ between distinct classes (LIU & SCHUMANN, 2005). For the utilization of the Relief-F procedure, instances of the sample data set were randomly drawn and k nearest neighbors for each class determined. With respect to k and the sample class, the neighbor features were compared and a score for each feature was assigned. This process was repeated m times, where m is a

user defined free variable, which is typically set to the number of instances to achieve a more reliable approximation (KONONENKO, 1994; LIU & SCHUMANN, 2005). For this study k was set to 10 analogous to GEIß ET AL. (2014a) and GEIß ET AL. (2014b), where it was found that the results for different settings of k were hardly sensitive. The outcome after applying the Relief-F approach is a ranked list of all features with a respective relevance value w. Out of this, 4 feature sets were generated for the 10, 20, and 50 best ranked features as well as for all positive ranked features ($w > 0$). Negative ranked features ($w < 0$) have no relevance for a class.

The feature selection methods were applied with respect to underlying data sets, segmentation scales, and classification techniques (cf. chapter 7). In figure 29 the eleven feature sets, generated by quantitative and qualitative feature selection criterions are schematically summed up.

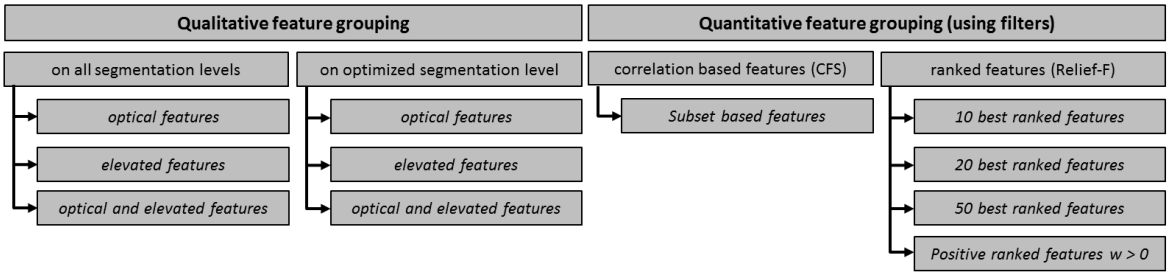

Figure 29: *Feature subsets from quantitative and qualitative feature selection methods.*

Accordingly, the respective features sets of CFS (cf. figure 30) and Relief-F (cf. figure 31) for each classification method is represented in the following illustrations. For each of the three learning approaches, different feature sets for Relief-F and CFS originated due to varying labeled reference instances (e.g., probable damage grades for SVR, three classes of in interest for C-SVM, and only one class label for ν-OC-SVM). The corresponding naming key for the features is attached in appendix D.

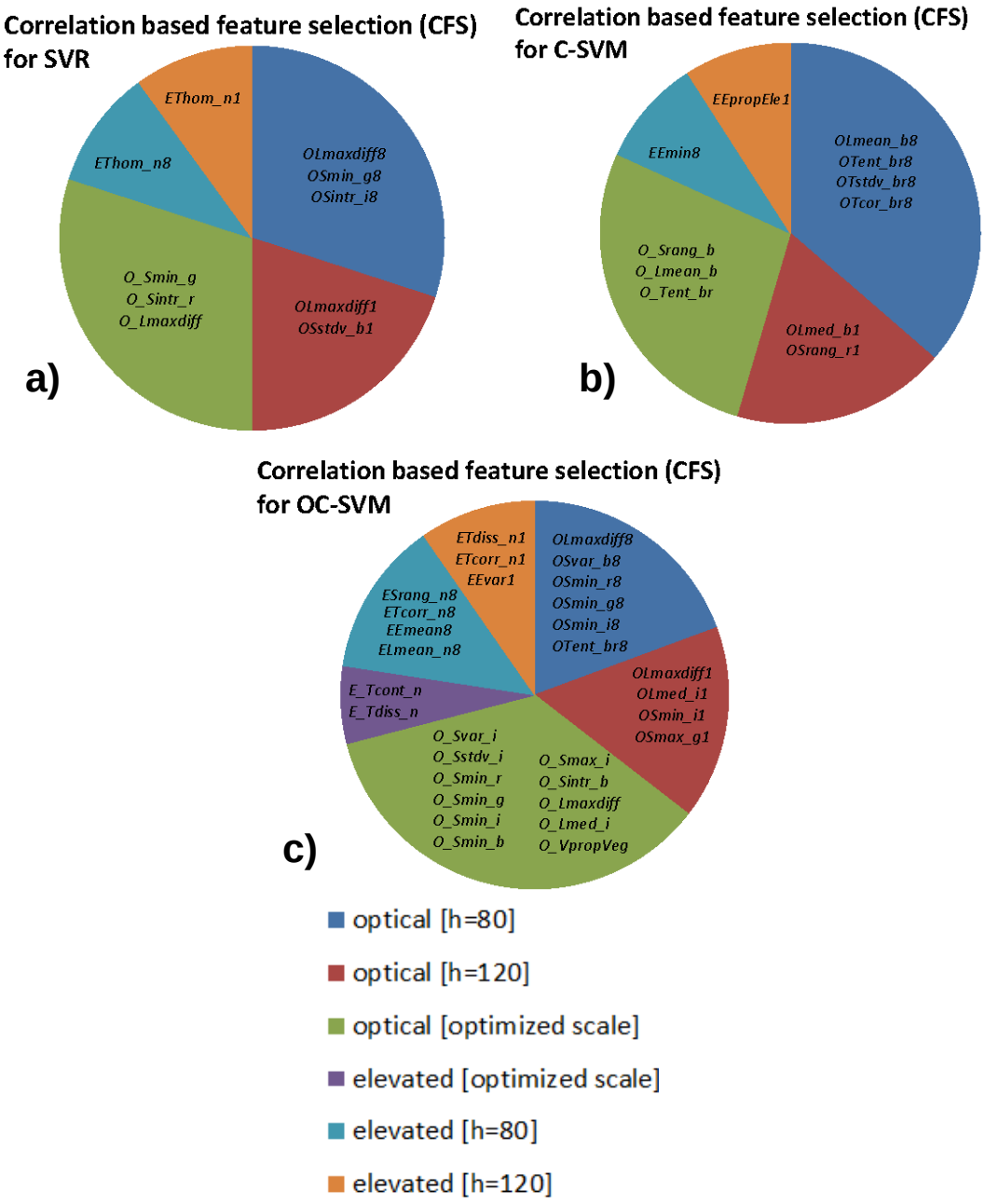

Figure 30: *Feature sets using CFS for applied classification methods SVR (a), C-SVM (b), and OC-SVM (c).*

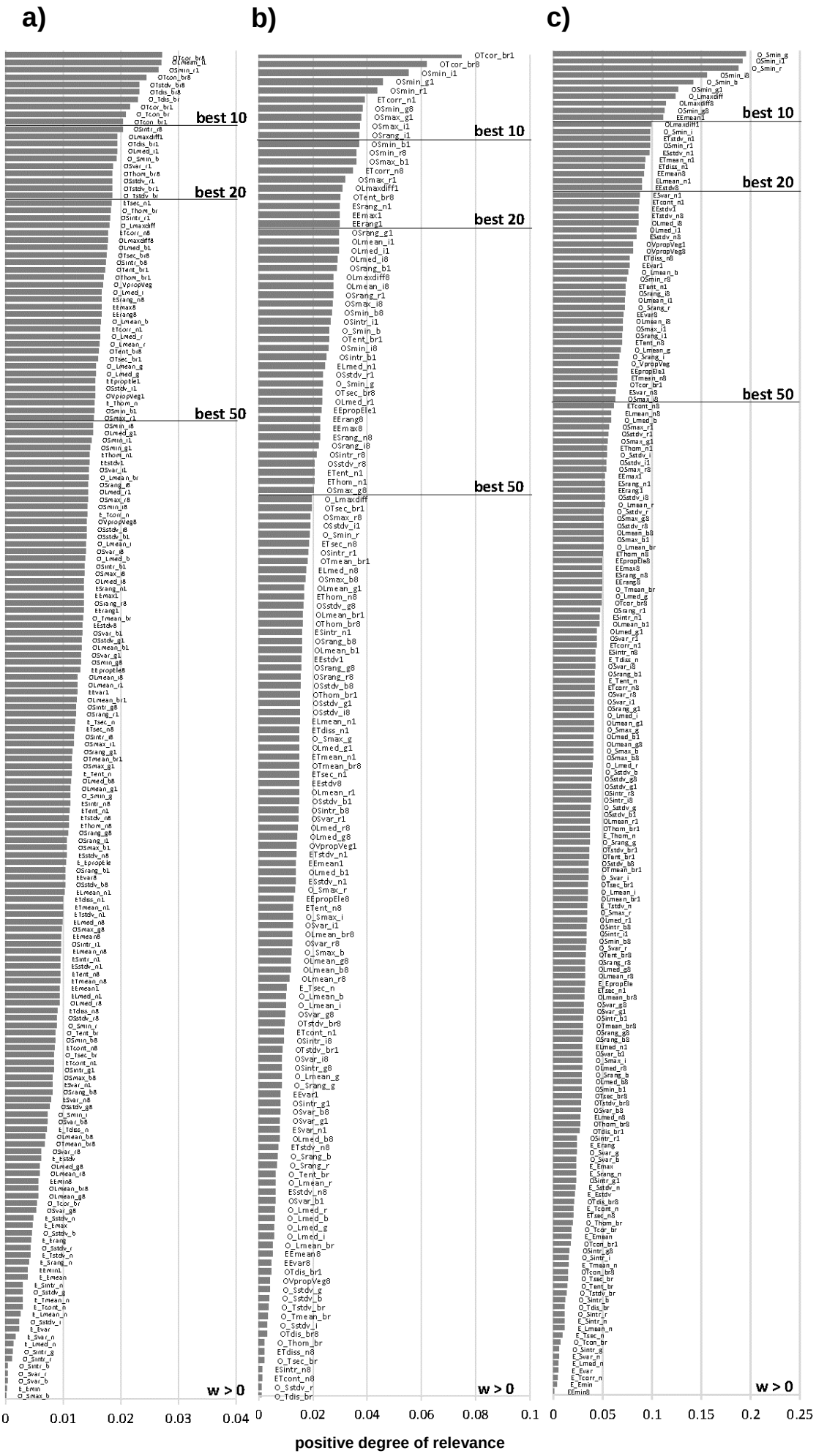

Figure 31: *Feature sets using Relief-F feature selection for applied SVR (a), C-SVM (b), and ν-OC-SVM (c).*

7. Identification of vulnerable Urban Areas

In this chapter the assessment of seismic vulnerability with respect to homogeneous urban areas of Istanbul is elucidated. This firstly comprises the description of methodological principles of Support Vector Machines (SVM), since they were applied for supervised classification and regression, in this study. More precisely, the utilized SVM methods Support Vector Regression (SVR), soft margin SVM (C-SVM) for Multi-Class problems, and One-Class SVM (OC-SVM) are introduced. The experimental setup and the application of the three approaches of SVM are indicated.

7.1 Supervised Methods for Classification and Regression: Support Vector Machines

For remote sensing data classification techniques are commonly used for pattern recognition. Generally, classification methods can be subdivided in supervised and unsupervised techniques, independently from the image analysis type (e.g., pixel-based, object-based). Thereby, supervised classification techniques are the mostly often used classification techniques for image analysis (RICHARDS & JIA, 2006). The decision for a supervised or unsupervised classification technique is especially controlled by the availability of training data, i.e. reference data or sample data. A further division of supervised classification techniques is constituted by the given form of the density function. Those can be of parametric or non-parametric character. The categorization of classification methods is given in figure 32.

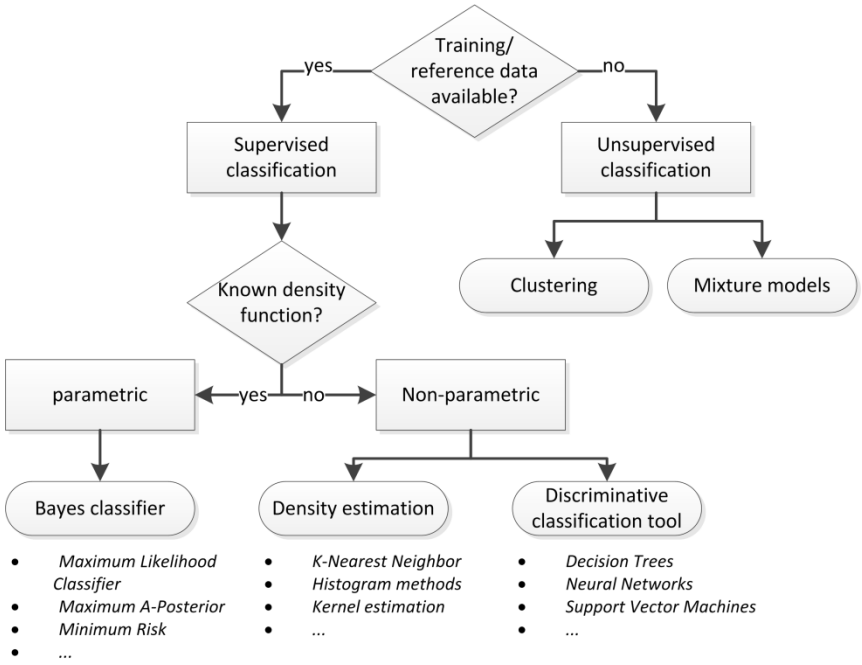

Figure 32: *Categorization of classification methods (**Source:** WASKE & BRAUN, 2009; modified).*

Due to the given complexity of assessing seismic vulnerability by the availability of a huge number of features related to seismic vulnerability, it was decided to use the classification approach of Support Vector Machines (SVM). Support Vector Machines arose from the field of machine learning and were introduced as a non-parametric supervised classification technique (RICHARDS & JIA, 2006) to remote sensing by GUALTIERI & CROMP (1998). The SVM approach based on the process of learning rules from a training set composed of labeled samples (i.e., classes) for the ensuing generation of a model.

During the further classification procedure, the generated models are used for estimating the respective class from the entire data set. Hence, that technique does not necessitates prior knowledge for the description of a class, as opposed to knowledge based classification techniques assembled by logical rules. Beside the utilization of SVM for classification purposes, it can be also used for regression analysis (VAPNIK, 1995).

A more detailed description of SVM is given in VAPNIK (1995), CORTES & VAPNIK (1995), VAPNIK (1998), SCHÖLKOPF & SMOLA (2002), SCHÖLKOPF & SMOLA (2004), BURGES (1998), CHRISTIANINI & SHAWE-TAYLOR (2000), CHANG & LIN (2001), and ABE (2005). Nowadays in many studies in the field of remote sensing the SVM approach was applied (e.g., MELGANI & BRUZZONE, 2004; TZOTSOS & ARGIALAS, 2008; MUÑOZ-MARI ET AL., 2010; MARCONCINI ET AL., 2014). Comprehensive information about SVM in

remote sensing is provided in MELGANI & BRUZZONE (2004), CAMPS-VALLS & BRUZZONE (2005), CAMPS-VALLS & BRUZZONE (2009), MOUNTRAKIS ET AL. (2011), and SALCEDO-SANZ ET AL. (2014). In the following the SVM principles after the just mentioned citations of training a model are outlined.

The training set S can be defined by

$$S = \{(x_1, y_1), \dots, (x_k, y_k)\} \subseteq (X \times Y)^{\mathrm{n}}.$$

At this, a single labeled training instance is compounded by x_i and y_i. Where x_i represents a n-dimensional vector of the feature space X, and y_i the associated output label. If S is used for classification, y_i delineates a certain attribute. If S is used for regression, y_i delineates a real number of the output domain.

The aim of training a model means the assignment of an appropriate class to each element of X. During the training stage, the training instances were separated with respect to the associated class label of the n-dimensional feature space. This procedure of deciding about the separation is determined by a so called hyperplane, which can be mathematical represented for a linearly two-class separation by

$$f(x) = \langle w, x \rangle + b = \sum_{i=1}^{N} w_i x_i + b \qquad w \in \mathbb{R}^N, b \in \mathbb{R}\ .$$

Where $\langle\ \rangle$ depicts the dot product, w the normal vector perpendicular to the hyperplane and b the bias. The separation of the data enables different hyperplane functions (i.e., different options of hyperplanes). Whereby the optimal hyperplane on a given sample set represents the best possible generalization process with respect to unseen data. Therefore, the optimal hyperplane is those hyperplane with the maximum margin between the instances. To minimize the risk of misclassifications of unseen instances, the hyperplane separates the instances with respect to the associated class label. Although a perfectly adjusted hyperplane to a specific distribution of instances in a training set without any outliers is the optimum. However, that is defined by a very complex decision function and entails poor results for unseen data. Therefore, SVM tackle this problem by an automatic optimization procedure of structural risk minimization. This is the process of finding a tradeoff between the accuracy of best fitting and the complexity, and overcomes the traditional empirical risk minimization (GUNN, 1998). At this, the marginal hyperplanes defined by the border instances of the

respective separated class are named support vectors (SV) (BURGES, 1998). In figure 33 the optimal separation of a linearly two-class problem is visualized.

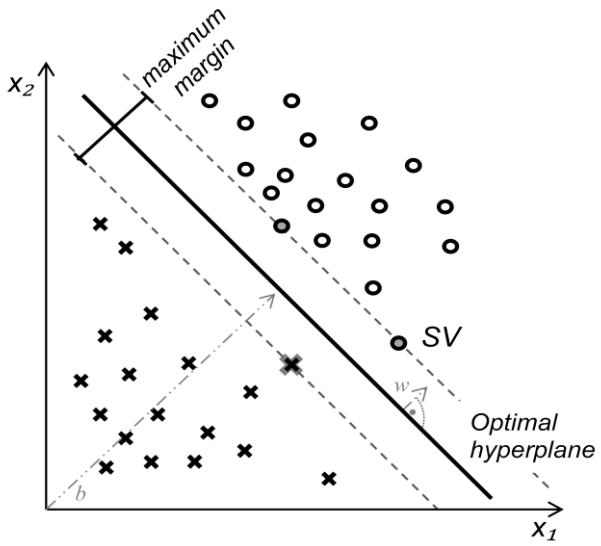

Figure 33: *Optimal separating hyperplane for two classes*
*(**Source:** SCHÖLKOPF & SMOLA, 2001, modified).*

However, in most cases the data set is not linearly dividable as figure 34a illustrates. Hence, the SVM approach overcomes this problem by mapping the training data $x_1, \dots, x_n$ into a higher-dimensional feature space H. This transformation procedure is defined by the kernel function Φ:

$$x = (x_1, \dots, x_n) \rightarrow \Phi(x) = \big(\Phi_1(x), \dots, \Phi_N(x)\big).$$

Subsequently, the training instances are then linear separable within the higher-dimensional feature space H. This enables the application of SVM not only on linearly distributed training instances. The SVM principles are graphically illustrated in figure 34.

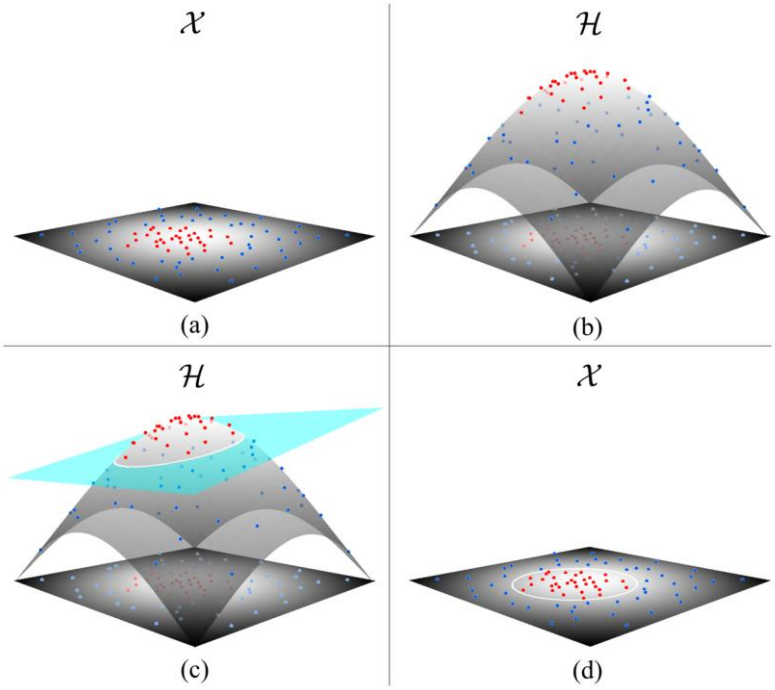

Figure 34: *Idealized procedure for generation of a nonlinear decision function by SVM. (a) Dataset with two classes (red and blue dots) that are non-linearly separable in X are mapped through a nonlinear transformation $\phi(\cdot)$ into a space of higher dimensionality H (b). A linear separation becomes possible in that space and a hyperplane (cyan) with maximum margin is fitted (c), what corresponds to a nonlinear decision function in X (d) (**Source:** GEIß ET AL., 2014d).*

Thereby the applied kernel function determines the shape of the decision surface (SCHÖLKOPF & SMOLA, 2002; CHRISTIANINI & SHAWE-TAYLOR, 2000). The kernel function can be of linear, polynomial, radial or sigmoid type (ABE, 2005; HSU ET AL., 2010). A commonly used kernel function in environmental applications is the Gaussian Radial basis function (RBF) (BURGES, 1998; VOLPI ET AL., 2013) with

$$K(x_i, x_j) = e^{-\gamma \|x_i - x_j\|^2} \quad \gamma > 0.$$

Where the free parameter γ is responsible for the smoothing of the function and is inversely proportional to the kernel width (MELGANI & BRUZZONE, 2004). The effects of oversmoothing and overfitting are results from a too large or too small kernel width (MOUNTRAKIS ET AL., 2011).

Furthermore, SVM can be used for distinct prediction problems with respect to the type of the sample data set by using diverse SVM approaches, such as a) Support Vector Regression (SVR) b) One-Class SVM (OC-SVM) or c) Soft-margin SVM (C-SVM). These three SVM approaches were applied for different experimental settings in this study and are therefore further expounded.

7.1.1 Function Estimation with Support Vector Regression

SVM provides an approach for regression analysis, so-called Support Vector Regression (SVR). This method can be applied for problems when the instances to be estimated features samples to an interval or ratio scale. At this a linear model (regression) is used on the mapped samples of the higher dimensional feature space, as it is defined in *f(x)*, mentioned in chapter 7.1. The linear regression of samples in a higher dimensional feature space is consistent to a non-linear regression in the feature space of lower dimensionality. SVR aims to find a certain function for the estimation of all training instances (x_i, y_i), where a specified deviation threshold ε is not exceedable (SCHÖLKOPF & SMOLA, 2004). ε can be seen as a kind of margin around the hyperplane ($\pm\,\varepsilon$), which is extendable by a loss-function. This function is composed by so-called slack variables ξ, which are used for measuring the deviation of sample instances towards the hyperplane for except outliers (TZOTSOS, 2006). In figure 35a the $\pm\,\varepsilon$ margin of a hyerplane for a linear SVM problem is shown. Figure 35b represents the proposed ε-insensitive loss function.

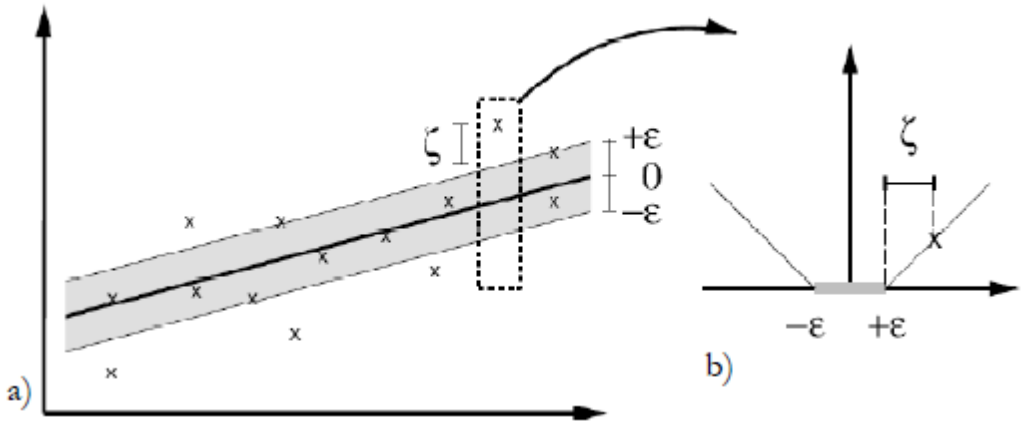

Figure 35: *Soft margin loss setting for a linear SVM (**Source**: SCHÖLKOPF & SMOLA, 2004).*

The ε-insensitive loss function enables the definition of a reliable generalization border. Thus, if the training instances fall inside the $\pm\,\varepsilon$ margin the instances are not affected. Then the ε-insensitive loss function is 0. Otherwise, the training instances are linearly penalized by the degree of the distance to ε. For this, weights w are defined for minimizing the complexity of the model by

$$\min_{\mathbf{w},\xi_i,\xi_i^*,b}\left\{\frac{1}{2}\|\mathbf{w}\|^2 + C\sum_i(\xi_i + \xi_i^*)\right\}$$

and is subject to

$$y_i - (\langle\phi(\mathbf{x}_i),\mathbf{w}\rangle + b) \le \varepsilon + \xi_i \qquad \forall i = 1, \ldots, n$$

$$(\langle\phi(\mathbf{x}_i),\mathbf{w}\rangle + b) - y_i \le \varepsilon + \xi_i^* \qquad \forall i = 1, \ldots, n$$

$$\xi_i, \xi_i^* \ge 0 \qquad \forall i = 1, \ldots, n$$

where ξ_i and ξ_i^* are the slack variables and C a regularization variable between the function flatness (complexity) and a tolerated error $\sum_{i=1}^{n}\xi_i$ of incorrectly estimated sample instances. The optimal parameter settings for C and ε have to be defined empirically and are the decisive factors for the generalization performance (training errors) and the model complexity. A transformation of the optimization objective can solve the dual problem when introducing the Lagrange multipliers α_i and α_i^* by the regression estimation function of

$$f(\mathbf{x}_*) = \sum_{i=1}^{n}(\alpha_i - \alpha_i^*)K(\mathbf{x}_i,\mathbf{x}_*) + b.$$

where K is the kernel function (e.g., RBF) and n the number of support vectors. The Lagrange multipliers were used to solve the minimization objective by quadratic programming techniques (DRUCKER ET AL., 1997; SCHÖLKOPF & SMOLA, 2002; VERRELST ET AL., 2012; SALCEDO-SANZ ET AL., 2014).

7.1.2 Targeted Classification with One-Class-SVM

Another SVM approach for classification depicts the One-Class SVM (OC-SVM). This approach is used for problems, where only labeled samples of one class (target class) are available. The fundamental idea of OC-SVM based on the process of separating origin labeled training instances (i.e., where the density is large) in the n-dimensional feature space with a maximum distance where outliers (instances on the other side of the hyperplane) are allowed. The region of the hyperplane, where the dominant share of sample instances is located, is called support region. For the separation of the support region, which covers the target class, no prior assumption of the data distribution is needed (GEIß ET AL., 2014d). Such a function can describe the target class. For that, two formulations of OC-SVM exist, the single class SVM (ν-SVM) after SCHÖLKOPF ET AL. (2000, 2001) and the support vector data description (SVDD) after TAX & DUIN (1999). These OC-SVM methods can be used for clustering and outlier detection (ABE, 2005). For the separation of the training instances the minimization objective for ν-OC-SVM, the applied OC-SVM method in this study is given by

$$\min_{\mathbf{w},\xi_i,p} \left\{ \frac{1}{2} \|\mathbf{w}\|^2 + \frac{1}{\nu l} \sum_i \xi_i - p \right\}$$

dependent on

$$\langle \mathbf{w}, \phi(\mathbf{x}_i) \rangle \geq p - \xi_i \qquad \forall i = 1, \ldots, l$$
$$\xi_i \geq 0 \qquad \forall i = 1, \ldots, l.$$

where "(w,p) are a weight vector and an offset parametrizing a hyperplane in the feature space associated with the kernel" (SCHÖKOPF ET AL., 2000, p. 1446). The parameter $\nu \in (0,1]$ controls the tradeoff between the amount of training samples and the model complexity (MUÑOZ-MARI ET AL., 2010). Analogous to C-SVM and SVR the introduction of Lagrange multipliers and a kernel function lead to the final decision function of

$$f(\mathbf{x}_*) = \operatorname{sgn}\left(\sum_i \alpha_i K(\mathbf{x}_i, \mathbf{x}_*) - p \right),$$

to classify unlabeled instances $\mathbf{x}_*$.

This approach can be further used for problems composed by more than one class. Therefore, the model has to be trained for each class separately. For the final result, comprising all classes, some heuristics (e.g., prior or posterior probability) have taken into account to determine final class membership for instances assigned to more than one class (MARCONCINI ET AL., 2014). Generally, the performance of this approach is sensitive to the selected kernel function (e.g., RBF) and the tuning of free parameters analogous to the C-SVM approach (cf. chapter 7.1.3). The separation of the data set, using the ν-OC-SVM approach is illustrated in figure 36.

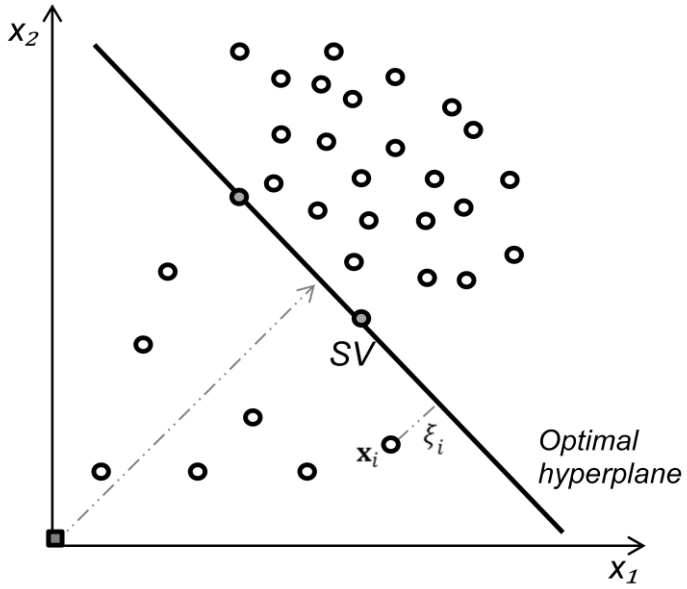

Figure 36: *ν-OC-SVM approach, where the hyperplane is used to separate with a maximum margin all target data from the origin. Whereby outliers are located in the lower side of the hyperplane and samples of the assigned target class in the upper side of the hyperplane.*

7.1.3 Multi-Class Classification with C-SVM

To tackle problems with class overlaps or noise in the training data, CORTES & VAPNIK (1995) introduced the soft margin SVM (C-SVM). This approach depicts a modified approach of the maximum margin problem. Thereby distinct labeled and distributed sample instances can be separated with relaxed constraints and enables therefore a multi-class classification. The labeled sample instances can be indicated as $\{\mathbf{x}_i, y_i\}_{i=1}^{n}$, with $\mathbf{x}_i \in \mathbb{R}^d$ and $y_i \in \{-1, +1\}$. As typical for SVM methods, the training sample instances are mapped from a linear feature space X via a non-linear transformation function $\Phi(\cdot)$ into a higher n-dimensional feature space H. Accordingly, the transformed training instances are then linearly separable (CAMPS-VALLS & BRUZZONE, 2005). For C-SVM the minimization objective is given by

$$\min_{\mathbf{w},\xi_i,b} \left\{ \frac{1}{2} \|\mathbf{w}\|^2 + C \sum_{i=1}^{n} \xi_i \right\}$$

and depends on

$$y_i(\langle \phi(\mathbf{x}_i), \mathbf{w} \rangle + b) \geq 1 - \xi_i \qquad \forall i = 1, \ldots, n$$
$$\xi_i \geq 0 \qquad \forall i = 1, \ldots, n.$$

The established variables were already described in chapter 7.1, 7.1.1, and 7.1.2. The application of this function enables the separation of various labeled sample instances with a maximum margin by the prevention of over-fitting ensured by means of slack variables. As well as the minimization objective function of SVR and ν-OC-SVM (cf. chapter 7.1.1 and 7.1.2), the C-SVM minimization objective function can be solved by means of Lagrange multipliers and quadratic programming techniques (SCHÖLKOPF & SMOLA, 2002). Thus, the decision function for the assignment of instances to a labeled class can be rewritten as

$$f(\mathbf{x}_*) = \operatorname{sgn}\left(\sum_{i=1}^{n} y_i \alpha_i K(\mathbf{x}_i, \mathbf{x}_*) + b\right).$$

Where $\mathbf{x}_*$ represents an instance of unknown class membership, K the kernel (e.g., the commonly used Gaussian RBF kernel) and α_i the Lagrange multipliers analogous to the variable description in the preceding chapters. The C-SVM approach enables a very reliable decision of estimating $\mathbf{x}_*$ in higher dimensional feature spaces.

7.1.4 Measures for Accuracy Assessment

Generally, the quality of classifications (cf. chapter 8.2 and 8.3) can be identified by means so-called confusion matrices. At that the classification results are compared with the labeled reference data for each class in tabular form. Out of this, a couple of accuracy measures can be calculated (e.g., κ-statistics, overall accuracy, user's accuracy and producer's accuracy), which are in the following outlined.

A measure of global accuracy is the κ-statistics and is commonly used for classification accuracies (FOODY, 2002). κ-statistics range from -1 to 1 and was introduced by COHEN (1960). A κ of 1 represents the highest possible accuracy, where all reference data correspond to the classification results. In contrast a, κ of -1 defines the lowest accuracy, at that the accordance of classification and reference data is randomized. Very high accuracies are quoted by a κ-statistic > 0.8 (GREVE & WENTURA, 1997).
κ is defined by

$$\kappa = \frac{n \sum_{i=1}^{r} x_{ii} - \sum_{i=1}^{r} x_{i+} \cdot x_{+1}}{n^2 - \sum_{i=1}^{r} x_{i+} \cdot x_{+i}}$$

where n is the sum of all objects from the calculated confusion matrix (i.e., total number of observations), r the number of lines from the confusion matrix (i.e., number of classes), x_{ii} the quantity of correctly classified objects (i.e., element of main diagonal of the confusion matrix), x_{i+} the sum of all objects in a line (i.e., classified values), and x_{+i} the sum of all object from a column (i.e., reference data). Therefore, κ-statistics considered commission and omission errors (cf. OA below) and is therefore not biased concerning the distribution of samples (FOODY, 2004).

The overall accuracy defined by

$$OA[\%] = \frac{\sum_{i=1}^{r} x_{ii}}{n} \cdot 100$$

is a measure for the proportion of correctly classified segments with respect to the total number of considered objects. By means of OA the error of commission

(i.e., mistakenly assigned objects of another class) as well as the error of omission (i.e., non recognized objects of a class) is considered in the accuracy evaluation.

User's and Producer's Accuracy are indicators for the classification precision of single classes calculable out of the confusion matrix. The User's Accuracy

$$UA[\%] = \frac{x_{ii}}{x_{i+}} \cdot 100,$$

defines the amount (in percentage) of ascertained classes agree with the reference samples. Whereas the Producer's Accuracy defines the percentage share of covered reference samples by

$$PA[\%] = \frac{x_{ii}}{x_{+i}} \cdot 100.$$

These accuracy measures are used for ν-OC-SVM and C-SVM for evaluation of the classifications (cf. chapter 8.2 and 8.3).

7.2 Seismic Vulnerability Assessment of Istanbul

In this chapter the three SVM methods, described in chapter 7.1.1, 7.1.2, and 7.1.3 were applied for the assessment of seismic vulnerability for different scenarios of available training data. As previously mentioned (cf. chapter 7.1), a sample data set is required for supervised classification techniques, such as SVM. This type of data set is often compiled by in situ surveys. Relating to SVM classification, the sample data is used for training a model which is then applied for estimating the respective class of instances in an area of interest. Generally, each SVM approach was applied on respectively 11 feature sets for qualitatively and quantitatively selected features, with respect to the SVM method as mentioned in chapter 6.2. Furthermore, the procedure of regression (SVR) and classification (ν-OC-SVM, C-SVM) of a certain feature set was repeated five times for different randomized samples. This enables to made a robust statement about the prediction accuracy and avoid skewed results of the utilized feature set. In addition, each randomized feature set, for SVR and C-SVM, was applied for 25%, 50%, 75%, and 100% of the sample data. For that, feature sets contained by a lower number of labeled samples of the data were completely covered by the

respective feature set with a larger number of labeled samples (e.g., the feature set based on 50% of the data completely contained the same feature set composed of 25% of the data). This was utilized to test the sensitivity of different numbers of applied samples, and to avoid a biased quantification of the sample data, which should be used for the assessment of seismic vulnerability.

In general, the procedure of learning models and the implementation of them on the entire study area was carried out within the WEKA software. The three SVM approaches were deployed with the *LibSVM* package (library for support vector machines) by CHANG & LIN (2001) and the proposed RBF kernel (BURGES, 1998). Furthermore, all features were normalized to obtain normalized kernel functions (GRAF ET AL., 2003). A detailed description of the applied sample data set, the training of models, and the utilized parameter settings for the respective SVM method is given in the subsequent chapters.

7.2.1 Estimation of Damage Grades with Support Vector Regression

The sample data, for the district Zeytinburnu emerged by fieldwork during the study by TAUBENBÖCK ET AL. (2009), was used for the generation of a reference data set for this study. Therefore, the data set, composed by single building objects provided with probable damage grades (labeled samples), was aggregated to the optimized segmentation scale according to the capacity spectrum method (cf. figure 12). The description of this data set and its aggregation, to make it usable as reference data for this study, was given in chapter 3.2.4. During the SVR procedure (with the LibSVM approach and the RBF kernel), labeled sample data were used for the estimation of probable damage grades for unlabeled urban structures. For this, a different number of labeled sample data (25%, 50%, 75%, and 100%) with varying randomizations (i.e., 5 differently randomized sample data sets) was used (cf. figure 37).

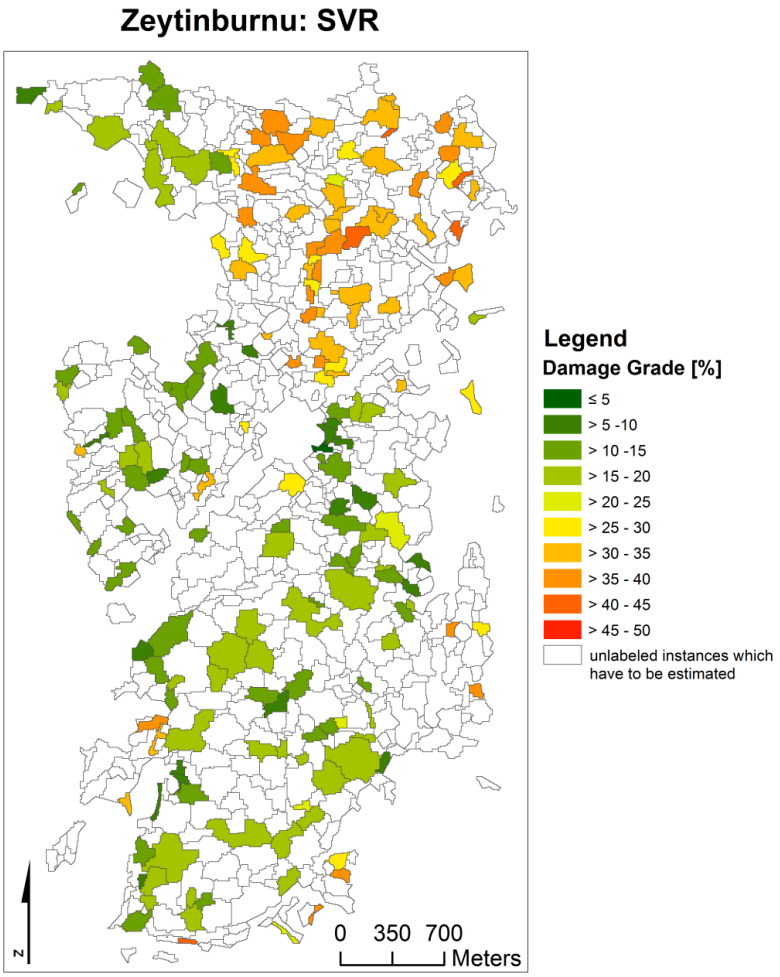

Figure 37: *Sample data for SVR.*

Furthermore, this setting of a different amount of labeled sample data and different randomizations was applied on the eleven feature sets (cf. chapter 6.2). Hence, the SVR was carried out for 220 distinct settings of the sample data set. These data sets were used as training sets for learning the models by using a 5-fold cross validation for each feature set. At this procedure the generalization capabilities can be evaluated as the average of three independent trails by reference to the mean absolute percentage error (MAPE) (GEIß ET AL., 2014d). The parameter tuning for finding the optimal settings based on the MAPE for ranges of $\sigma = \{10^{-1},\ldots,10\}$, $C = \{1, \ldots, 100\}$, and $\varepsilon = \{10^{-6}, 10^{-3}\}$. Figure 40 (cf. chapter 8.1) represents the respective MAPEs as functions for distinct training set sizes (25%, 50%, 75%, and 100% of the sample data) of each feature set, composed of their respectively randomized sample data. With respect to the seismic vulnerability assessment, the MAPE is a measure for the accuracy of the applied feature sets. Furthermore, the associated maps of estimated damage grades for Zeytinburnu, using SVR are represented in figure 41 and are discussed in chapter 8.1.

7.2.2 Assignment of Vulnerability Classes with ν-OC-SVM

Due to the fact that only reference data for Zeytinburnu exist (cf. chapter 3.2.4), the SVM approaches of C-SVM and OC-SVM necessitates sample and reference data for the entire study area. This kind of data is normally acquired in the field, as already mentioned in chapter 7.2.1. However, for such size of a study area in situ surveys were too costly and time-consuming. Therefore, the generation of reference data is grounded on expert knowledge about urban structures. For that, the available reference data of Zeytinburnu was used to derive information about seismic vulnerability with respect to different urban structures.

The comparison of the reference data of Zeytinburnu (cf. figure 11 and 12 in chapter 3.2.4) with the optical remote sensing data shows that especially large commercial and industrial urban structures were identified as highly vulnerable urban areas. Thereby, low damage grades were assigned to tall detached residential buildings which indicate a rather slightly seismic vulnerability for this urban structure type. This relation of building types was also used for seismic vulnerability assessment in WIELAND ET AL. (2012). For the residual urban areas medium damage grades were principally recognized and indicated therefore a medium seismic vulnerability. As a consequence, these three types of urban structures have to be found in the study area by a reliable source. For that, Google Street View, a technology of Google where real panoramic views from the position of a car was taken to create a virtual reality, provides the opportunities to unambiguously categorize certain urban structures by having a look on the images from a building. However, Google Street View is actually not provided for Istanbul. Hence, ground-based GPS photos from Google Earth (i.e., Google Panoramio™) were taken to generate a reference data set. Segments of the optimized segmentation scale were labeled as one of these certain classes if a ground-based GPS photo was available for this urban structure type.

Analogous to TAUBENBÖCK ET AL. (2009), detached buildings with more than 7 floors and a primarily residential usage represent the class ‘tall detached buildings’. Commercial/ industrial urban structures are composed of buildings with a large spatial extent like storage houses, usually with brightly flat roofs not higher than 4 stories. The class residual urban structures involves single detached and terraced houses primarily for residential usage or mixed usage, and all other buildings which could be not identified as tall detached buildings or commercial/ industrial buildings.

The OC-SVM method is used for the classification of one class of interest (cf. chapter 7.1.2). However, as already mentioned in chapter 7.1.2 the ν-OC-SVM approach can be applied separately for a respective classification procedure (i.e., calculation of two single OC-SVM classifications) of the class of interest which is then combined. This experiment was a realistic task for real-life situations, for instance when not all information for a class of interest are available. Therefore a reference data set with the two types of urban structures (i.e., large industrial/ commercial buildings and residential high-rise buildings) is required. For that, only samples of these two classes were used as samples as illustrated in figure 38 (i.e., 191 samples for commercial/ industrial urban structures and 305 samples for tall detached residential buildings). Thereby commercial/ industrial buildings represent highly vulnerable structures, whereas high-rise buildings depict low vulnerable urban structures. For assigning a label to unlabeled samples, 50% of each class of the sample data was used for computing the models composed of different feature sets (cf. chapter 7.2). Whereas the other 50% were restrained for validating the classification accuracy (cf. chapter 8.2). However, with OC-SVM only one class of interest can be assigned a label, thus the result of OC-SVM is binary (i.e., estimated class of interest and the negative class).

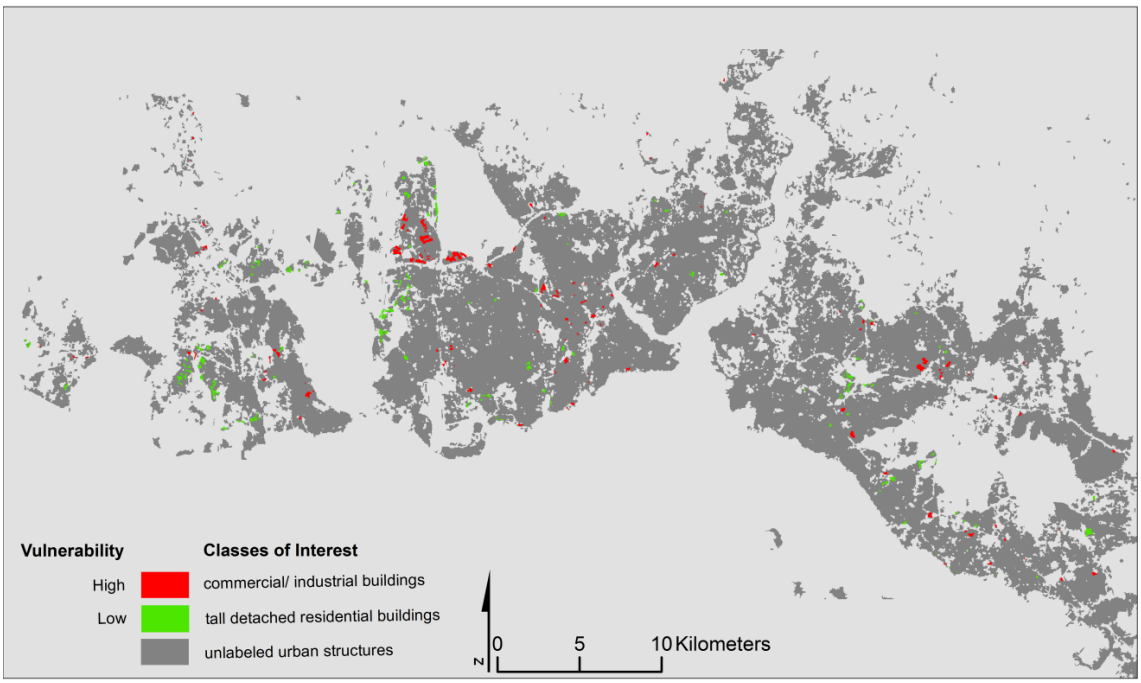

Figure 38: *Sample data for OC-SVM.*

The application of the ν-OC-SVM method was carried out with the RBF kernel, which requires the adjustment of two free parameters ν (i.e., tradeoff between the share of outliers and the model complexity) and γ (i.e., kernel width). The free parameter tuning procedure is a difficult task, if only labeled samples of one class are available. So that only true positive rates (i.e., sensitivity) can be calculated. The negative class can not be calculated in respect to its specificity (errors). In MUÑOZ-MARI ET AL. (2010) and MARCONCINI ET AL. (2014) a heuristic of

$$\arg max_{\theta} \left\{ \frac{OA[\%]}{\#SV} \right\}$$

is used to overcome this problem. Where θ is the set of free parameters, OA the overall accuracy and $\#SV$ the number of support vectors. Therefore, a high OA and a simultaneously low model complexity, composed of a low number of SV, reveals a high value for the heuristic. Therefore, the optimal settings of the free parameters ν and γ is given for the highest value of the evaluation heuristic. Regarding the parameter tuning a grid search for the range {0.01,…, 0.1} for ν in 0.01 steps and a range of $\{10^{-2}, \dots, 10^{1}\}$ for γ in power of $\sqrt{10}$ steps was applied. The calculation of OA used a 5-fold cross-validation, analogous to the C-SVM approach (cf. chapter 7.2.3).

For the assessment of seismic vulnerability the respective classification results (i.e., for each feature set) of ν-OC-SVM were combined. Thereby a segment could be assigned to both classes, in this case the segment is assigned to the negative (i.e., residual) class, due to the reason that this segment was not indiscernible (i.e., this segment was classified as tall detached residential buildings in the first OC-SVM classification, and in the second OC-SVM classification aiming to identify industrial/ commercial as this class). The evaluation of the models accuracy (i.e., κ-statistics, OA, UA, and PA) and the respective best results for each feature set (i.e., for five independently randomized sample data), represented as maps are outlined in chapter 8.2.

7.2.3 Assignment of Vulnerability Classes with C-SVM

For this classification method, data acquired from ground-based GPS images (cf. chapter 7.2.2) were used as reference data for learning the models and validating three types of urban structures, related to seismic vulnerability. Thereby, the reference data set is composed of 696 samples (191 for commercial/ industrial urban structures, 305 for tall detached residential buildings, and 200 samples of the residual class). The distribution of the sample data (i.e., reference data) over the entire study area can be obtained from figure 39. In the classification procedure 50% of the reference data were used as sample data set for training the model and the other 50% for validation purposes.

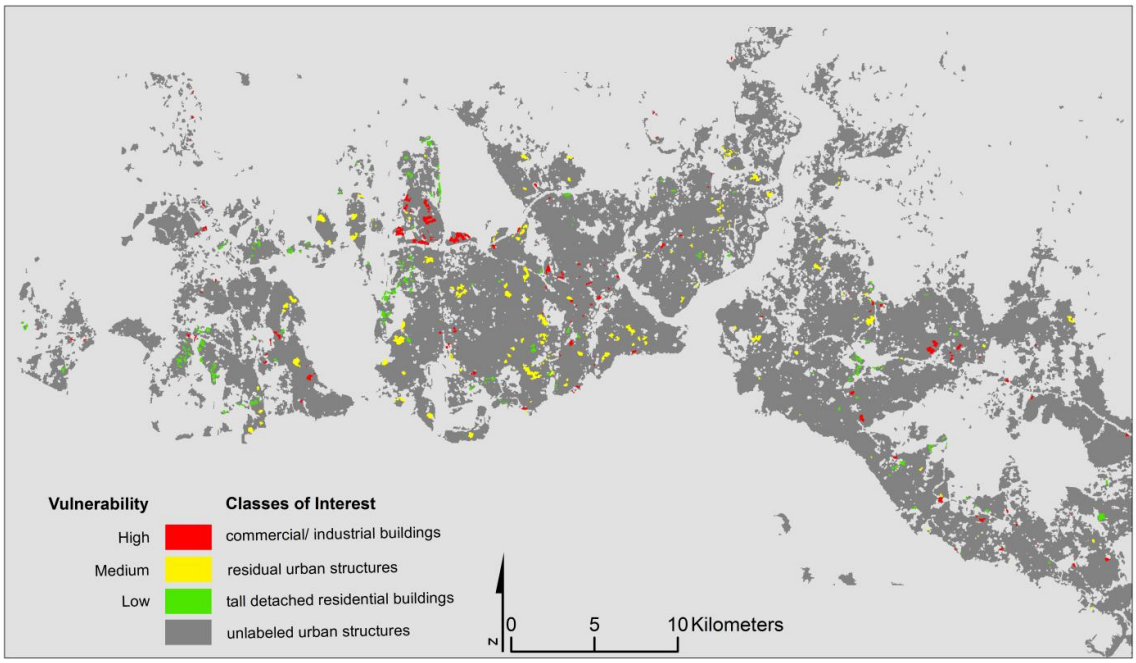

Figure 39: *Sample data for C-SVM.*

For the classification of these three classes with the fully supervised classification approach of C-SVM, a one-against-one scheme was selected (HSU & LIN, 2002). The most qualified model generated with the RBF kernel for C-SVM requires the tuning of the free parameters C (cost-parameter) and γ (kernel width). For tuning these parameters the grid search method enables to avoid an exhaustive trial-and-error procedure. Thereby, the grid search strategy based on a 5-fold cross-validation was carried out for HSU ET AL.'S (2010) proposed settings of $C = \{2^{-4}, 2^{-3}, \ldots, 2^{12}\}$ and

$\gamma = \{2^{-5}, 2^{-4}, \ldots, 2^{3}\}$. The evaluation of the generalization accuracy deploys the estimated κ-statistics for three independent trials, similar to SVR. This procedure was done for each feature set (i.e., thematically selected and by using filters) with different randomizations of the samples (i.e., five variations so that the result is not biased due to the distribution of the labeled instances (FOODY, 2004)) and a varying amount of labeled samples (i.e., 25%, 50%, 75%, and 100%). Analogous to the SVR approach the generalization capabilities are represented as a function of the feature sets and are displayed in figure 45. The corresponding discussion and the maps are given in chapter 8.3.

8. Results and Discussion

In this chapter the results of the applied SVM methods (SVR, C-SVM, and ν-OC-SVM) are represented and discussed with respect to the utilized feature sets and their accuracies (cf. chapter 7.1.4). At that, the respective quantitatively selected features (i.e., feature selection using filters) for each SVM method can be obtained from figure 30 (CFS) and 31 (Relief-F) in chapter 6.2.

8.1 Evaluation: Estimation of Damage Grades with SVR

The regression analysis with SVR was carried out with different training set sizes and randomizations of these samples, as already mentioned in chapter 7.2.1. The illustrated MAPE functions for these feature sets, given in figure 40, shows differences in their accuracies. Especially the feature set compounded by features derived from elevation data only (i.e., nDSM) perform a higher MAPE than corresponding features from optical data (cf. figure 40a and 40b). More precisely, when considering the MAPE values from elevation features from the optimized segmentation scale, it decreases from 20.76% ($\pm$ 0.94) and a respective correlation coefficient R of 0.16 (i.e., goodness of model fit) to a MAPE of 16.23% ($\pm$ 0.36; R=0.54), for the feature set composed by optical features (figure 40a). Furthermore, the graphs indicates better results (i.e., lower MAPEs) for feature sets derived from all segmentation levels, where super- and sub-object information are considered, than to feature sets derived from the optimized segmentation level only. For this type of feature sets (cf. figure 40b) the MAPE value of elevation features decreases from 14.54% ($\pm$ 0.41; R=0.60) to 11.64% ($\pm$ 0.30; R=0.75) for optical features. Thus, it can be said that feature sets considering feature information from further segmentation scales (i.e., h=80 and h=120) achieve better accuracies than feature sets only from the optimized segmentation scale. Figure 40a and 40b also depicts, that a combination of optical and elevation features does not increase a notable accuracy against the optical features (GEIß ET AL., 2014d). This can

be noticed by observing the MAPEs for these feature sets. For that, the combined features (all = elevation and optical) on all segmentation levels obtained lowest MAPE value of 11.85% ($\pm$ 0.30; R=0.74) and for the same feature set based on the optimized segmentation only a value of 16.34% ($\pm$ 0.36; R=0.52). In figure 40c the MAPEs from selected feature sets by using filters (i.e., Relief-F and CFS) are represented. From this, the lowest MAPE value of 10.74% for the ranked feature set with the best 50 features can be depicted. This feature set gained therefore the highest accuracy of the applied SVR method.

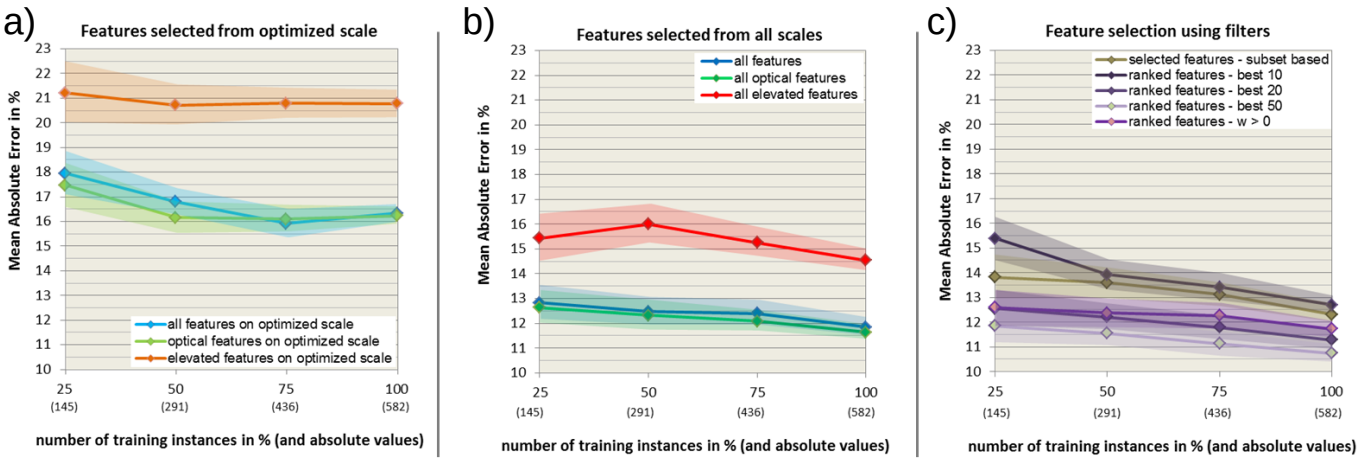

Figure 40: *Functions of the mean absolute percentage errors (MAPE) for different training set sizes of the applied feature sets with SVR. a) MAPEs for feature sets derived from the optimized segmentation scale; b) MAPEs for feature sets derived from the optimized segmentation scale, h=80, and h=120 and c) MAPEs for feature sets selected by filter methods.*

Basically it was found that feature sets derived from elevation data only (i.e., height information from nDSM) can not achieve suitable accuracies. The highest accuracies could be gained for thematically derived features by more than one segmentation scale, analogous to BRUZZONE & CARLIN (2006) and JOHNSON & XIE (2013). That indicates that one segmentation scale is not enough to achieve high accuracies. Despite that the multi-scale segmentation integrates more than one scale, but with still present over-segmentation as mentioned in chapter 5.2.2. The over-segmentation is most notable in regions characterized by large industrial complexes. Ideally similar industrial complexes should be represented by one segment (i.e., homogeneous urban area) and not by multi-segments (i.e., over-segmented). However over-segmentation is not completely avoidable. With respect to classification, over-segmented objects can be possibly assigned to one class of interest in contrast to under-segmented images.

The implementation of further segmentation scales, containing super-object information precise assignments of class labels can be promoted. Hence, the feature sets from more scales with super-object information could reduce the MAPE as can be seen by comparing figure 40a and 40b.

With respect to the complex urban morphology of Istanbul (especially for industrial/ commercial urban structures) the additional information of super-objects attained higher accuracies (cf. figure 40b). The SVR mapping results deployed on models originated by 50% of the samples, for the appropriate feature sets and are illustrated in figure 41 with respect to its corresponding MAPE. The residual 50% of the sample data are used for validation.

The inspection of the maps shows that extremes (i.e., lowest and highest damage grades) were barely estimated in all maps. Especially in feature sets with higher MAPEs, the models estimated mainly medium damage grade values, so over- and underestimation of the extremes are present. That reflects the typical phenomenon of regression analysis to the mean, which was initially delineated by GALTON (1886). This effect particularly appears for features with low correlations. Therefore, the correlation coefficient R is an additional important measure for the determination of accuracies from regression analysis, beside the MAPE. Hence, the optimum is indicated by a high R and a low MAPE.

The mapping results in figure 41 depict the relations of R and MAPE for each feature set. Thereby, low correlation coefficients are associated with higher MAPEs and the associated effect of regression to the mean. For all mapping results with R > 0.7 a MAPE < 14% was obtained and a relatively slight effect of the regression to the mean is present. That reflects also the best fitted model with good agreements to the reference data, which was originated from the best 50 ranked features with the lowest MAPE of all feature sets of 13% and an R of 0.75.

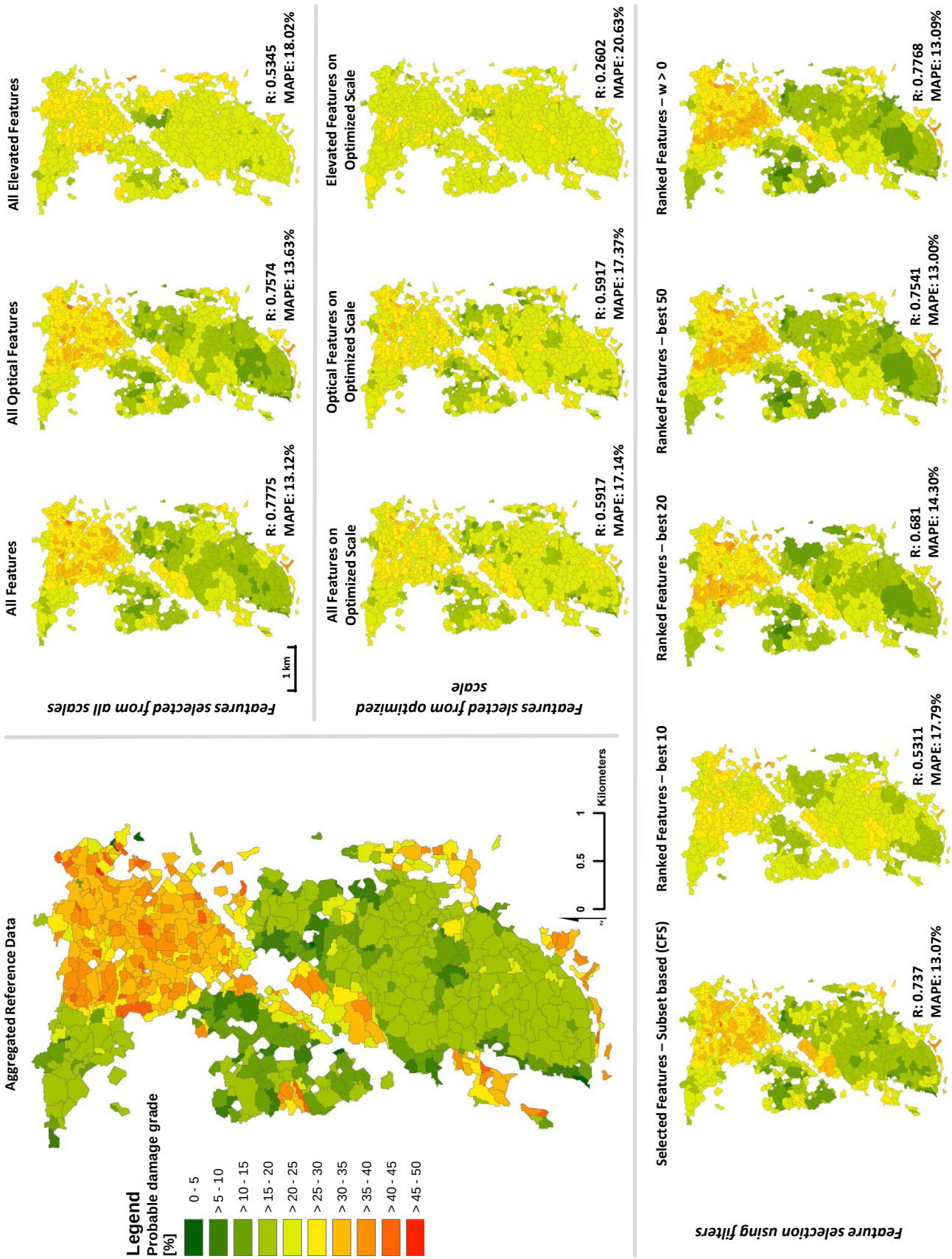

Figure 41: *Estimated damage grades for Zeytinburnu using SVR on different feature sets.*

8.2 Evaluation: Assignment of Vulnerability Classes with ν-OC-SVM

The models created with ν-OC-SVM from the eleven feature sets, composed five independent trials (i.e., randomized distributions of sample data) were validated by means of 50% of the samples, which were previously not used for model learning. Furthermore, 50% of the reference samples from the residual class, available for C-SVM, were used for validation. The classification accuracy is quoted by the κ-statistic, User's- and Producer's Accuracy for each class label, and the Overall Accuracy as described in chapter 7.1.4. The predicted κ-accuracies for the models composed of different randomly drawn feature sets are given in figure 42.

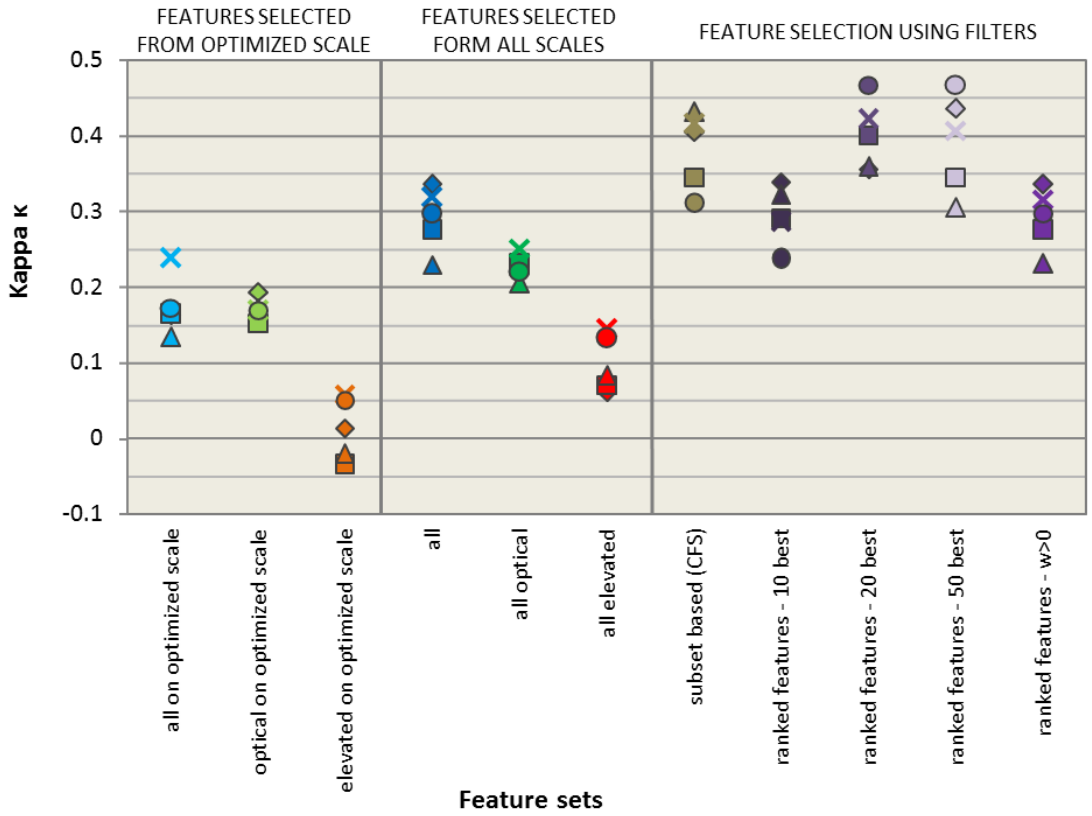

Figure 42: *Functions of the κ-statistics of the combined ν-OC-SVM results for different feature sets with five different randomly drawn feature sets (marked with different symbols: □,◇,○,×,△) a) represents the classification accuracies (κ-statistics) for feature sets derived from the optimized segmentation scale; b) the classification accuracies for feature sets derived from the optimized segmentation scale, h=80, and h=120 and c) the κ-statistics for feature sets selected by filter methods.*

At this point, it should be noted that each trial of randomly drawn samples is similar for the respective feature set. Even more interesting are the differently achieved accuracies of each randomization (cf. figure 42) where the highest accuracies were not always obtained from the same randomization. Similar to the SVR-approach the accuracies of distinct feature sets differ significantly. As well as for the other applied SVM methods, feature sets composed of optical features could generally gained higher accuracies than elevation features or feature sets made up of elevation and optical features (i.e., all features). In addition, feature sets derived from optimized scale only, achieved lower accuracies than the same feature sets obtained from all segmentation scales, analogous to the SVR approach. Thereby, the κ-statistics range from -0.03 to 0.24 for feature sets derived from the optimized scale only. In general a mean increase of κ-statistics by 0.09, 0.05 and 0.12 regarding similar feature sets from optimized scale to all scales could be recognized. Again the highest κ-statistic, and therefore the highest accuracy, were encountered within the group of feature sets originated by feature selection methods with filters. Thereby, the highest accuracy of κ = 0.468 was achieved for the 50 highest ranked features, closely followed by the 20 best ranked features with a κ-statistic of 0.467. However, the accuracies between the five independent trials of the 50 best ranked features exhibit a larger spread, than for the best 20 ranked features (cf. figure 42). Hence, no precise suggestion regarding the viability of a specific feature set (i.e., best 20 or best 50 ranked features) in real-life situation can be given. Nevertheless, figure 43 shows the seismic vulnerability of Istanbul for the highest obtainable accuracy from the underlying best 50 ranked feature sets. In addition, the feature ‘year of construction’ (cf. chapter 6.1.3) was attributed to extract the urban development regarding the urban structures.

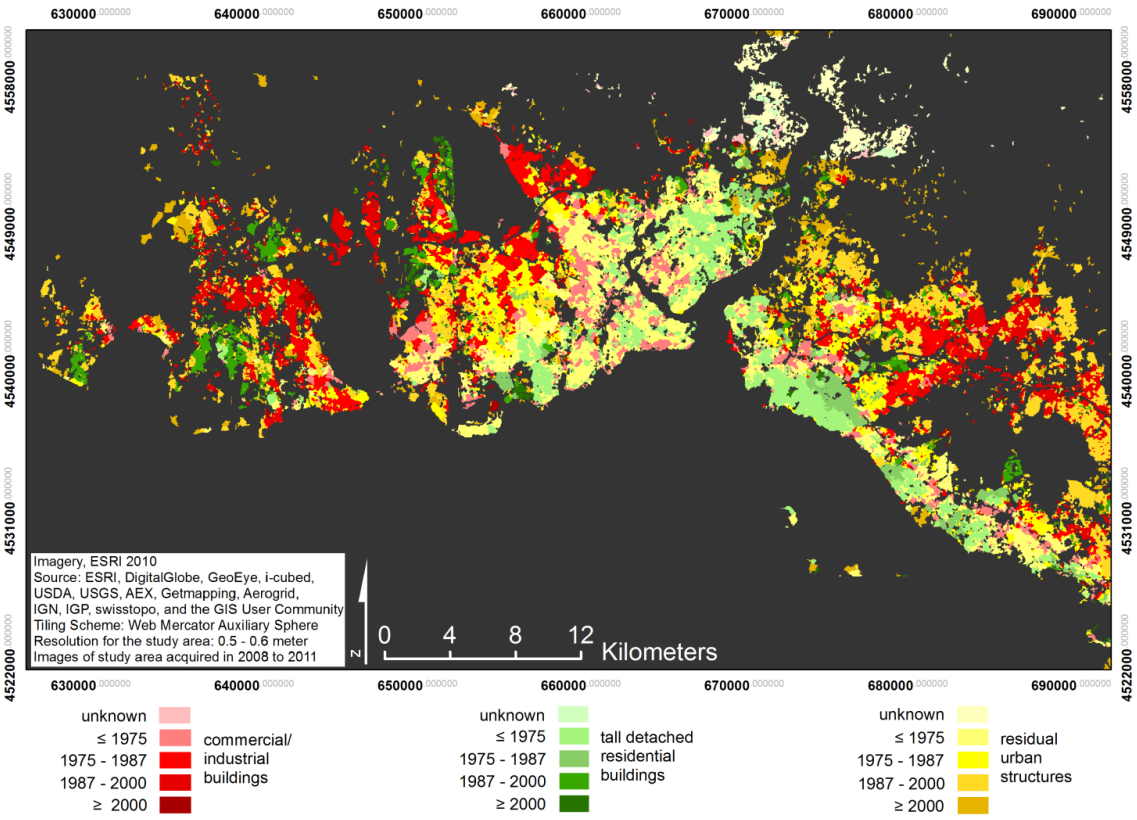

Figure 43: *Classification of urban structures of Istanbul with an ensemble of ν-OC-SVM for the highest obtainable accuracy combined with the year of construction.*

Additionally, the highest attainable accuracies (OA, UA, PA, and κ-statistics; cf. chapter 7.1.4) for the applied feature sets are represented as seismic vulnerability maps with respect to the class of interest in figure 44. That shows that the class tall residential building was generally best estimated with an UA of 66.67% to 87.14% when comparing all feature sets used for generating the maps. Despite, the PA ranges between 9.21% and 86.84%, whereas low values were mainly gained for the elevated feature sets. The class industrial/ commercial buildings could be correctly estimated by 53.33% – 80.56% (UA) with an associated PA of 12.63% to 74.74%. The residual class obtained the lowest rate of correctly estimated objects, indicated by its UA of 28.76% to 42.86% and a respective PA of 39.0% to 91.0%. This affirms the statement that it is difficult to delineate only one class of interest (i.e., commercial/ industrial buildings and high-rise buildings) by true positive rates, whereas the residual class represents the negative class, despite of the combination of single ν-OC-SVM classifications. The highest accuracy (κ-statistic of 0.47 and OA of 65.4%) was obtained from the best 50 ranked features as already mentioned before. This highest obtainable accuracy of a medium agreement with the reference data, questions the viability in real-life situations, especially in comparison to the results of the C-SVM approach, as outlined in the subsequent chapter (GEIß ET AL., 2014d).

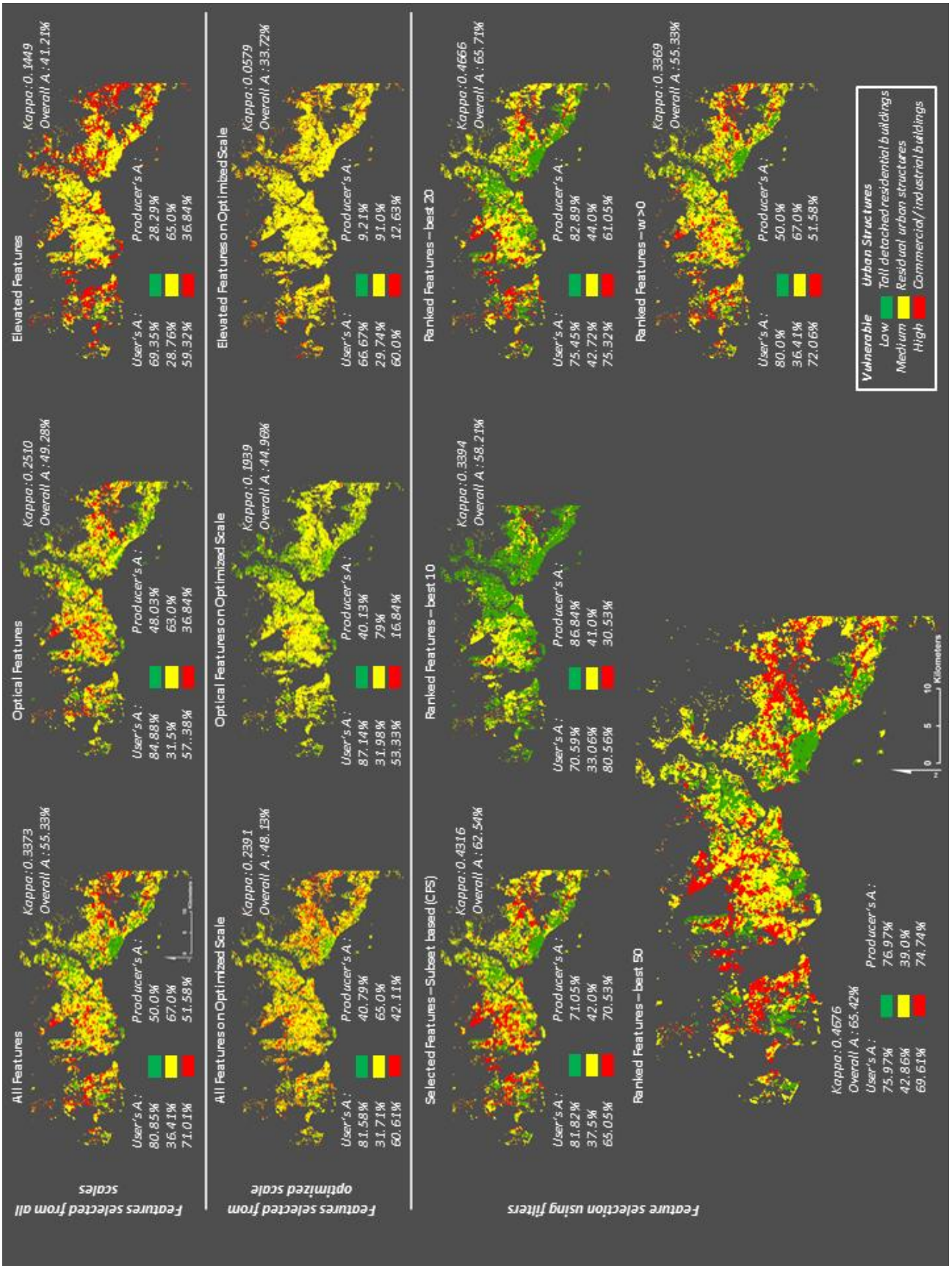

Figure 44: *Classification of urban structures of Istanbul using an ensemble of ν-OC-SVM for different feature sets.*

8.3 Evaluation: Assignment of Vulnerability Classes with C-SVM

Similar to the ν-OC-SVM strategy, the model accuracies of the different feature sets were graphically represented as functions in figure 45. Thereby, the accuracy for each feature set was calculated as the mean of five independent trials for different shares of samples and distinct feature sets. The figure is analogous to the seismic vulnerability assessment with SVR subdivided in the distinct types of feature sets by a) features derived from optimized segmentation scale, b) features derived from all scales, and c) features selected with filters (i.e., CFS, Relief-F).

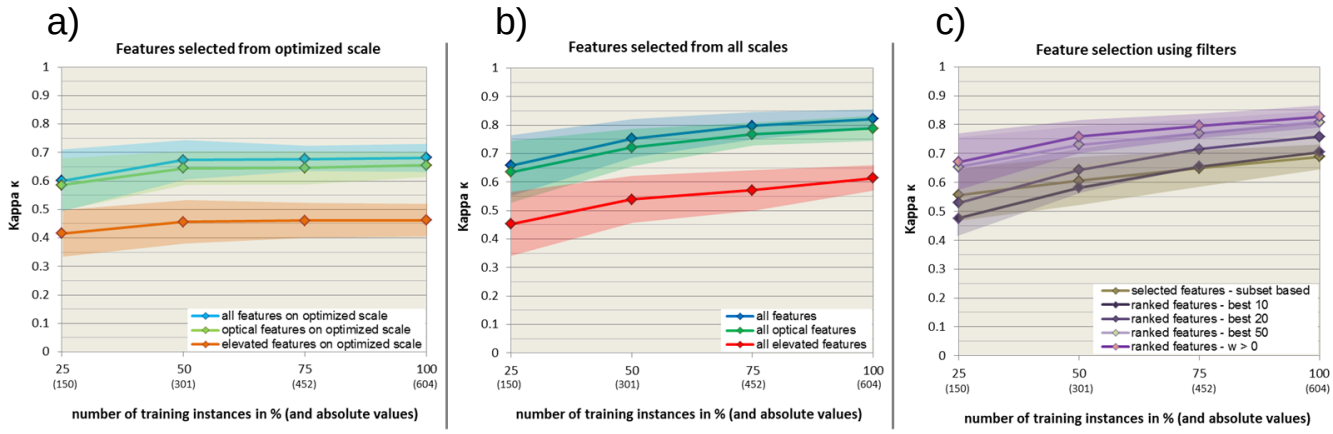

Figure 45: *Functions of the κ-statistics for different training set sizes of the applied feature sets for C-SVM. a) represents the classification accuracies (κ-statistics) for feature sets derived from the optimized segmentation scale; b) the classification accuracies for feature sets derived from the optimized segmentation scale, h=80, and h=120 and c) the κ-statistics for feature sets selected by filter methods.*

In comparison with the other SVM approaches the accuracies differs depending on the applied feature sets. Elevation feature sets on optimized segmentation scale (κ=0.46 $\pm$0.05) as well as on all scales (κ=0.61 $\pm$0.04) could gained, compared to respective optical and all features the lowest accuracy. The highest κ-statistic for qualitatively selected feature sets (i.e., features from optimized segmentation scale only and from all scales) were revealed for the combined feature sets with a slight difference (i.e., a difference between -0.022 and -0.044) to the optical feature sets. For the combined feature set on all scales a κ-statistic of 0.832 ($\pm$0.02) could be gained, and a

κ-statistic > 0.7 ($\pm$0.03) for the features derived from the optimized segmentation only. Concerning the features sets selected by filter methods, the highest classification accuracy was found for the feature set of all positive ranked features of the Relief-F approach (i.e., $w > 0$). For this feature set a κ-statistic of 0.827 ($\pm$0.05) was achieved. Therefore, the best performed classification result was generated for the trained model of the feature set derived for all segmentation scales with elevation and optical features together. This feature set covers only one more feature (i.e., n=153) than the ranked feature set with all positive ranked features (i.e., n=152). The attained classification accuracies of κ-statistic > 0.81 indicate excellent classification accuracies (GREVE & WENTURA, 1997).

The estimated classes of each type of feature set for Istanbul is given in figure 47 and gives indications about the seismic vulnerability of the city. Thereby 50% of the sample data were used for training the model, and 50% for validation purposes analogous to OC-SVM. Respective κ-statistics, Overall Accuracy, as well as User's- and Producer's Accuracy of each class label for the applied feature sets are given in the illustration.

In general, when comparing all mapping results of all deployed feature sets the tall detached building class could gained a Producer's Accuracy between 70.3% and 93.0% and a User's Accuracy of 77.3% to 99.4%. The commercial/ industrial class achieved a Producer's Accuracy between 47.3% and 84.9% and a User's Accuracy of 62.5% to 84.8%. A large range was obtained for PA and UA for the residual class, where PAs were between 37.3% and 86.7% and UAs between 34.4% and 70.5%. Therefore, the class containing high-rise buildings could be generally best estimated (UA between 77.3% and 99.4%), whereas the residual class was partly difficult to be estimated, similar to the ν-OC-SVM approach (cf. chapter 8.2). However, that reveals the assumption for this type of urban structures, because this class comprised a combination of different building types, whereas the other classes where composed of only a single type of buildings. This illustration (figure 45) demonstrates that especially elevation features achieved an over-estimation of commercial and industrial urban structures, as can be seen from the low PA and UA (UA 55.2% and PA 62.4% for elevated features on optimized scale and UA 62.5%, PA 64.5% for elevated features on all scales). For the quantitatively selected feature sets (cf. figure 47) very high accuracies (UA > 84%) of tall detached residential buildings could be achieved.

The highest overall accuracy (85.63%) and the highest κ-statistic (> 0.77) was identified for the feature set covering all features on all segmentation scales. Especially

for the residual urban structure types (UA: 70.5%) and the commercial/ industrial buildings (UA 84.8%) the highest accuracies were obtained on this feature set. Despite that tall detached residential buildings achieved a UA of 94%, this urban structure type could be better derived for the feature sets with the best 50 ranked features (UA: 99.4%) as well as the optical features on all scales (UA: 95.7%). However, the OA is higher than for optical features on all scales or the 50 best ranked features (i.e., it is a tradeoff of accuracies of all classes).

Additionally, as already mentioned in chapter 8.2, the information 'year of construction' is added as supplementary information to the best classification result (i.e., based on the combined feature set composed of optical and elevation features from all segmentation scales) and is illustrated in figure 46. This illustration shows the development of Istanbul's built-up area with respect to the type of urban structures before 1975 till now.

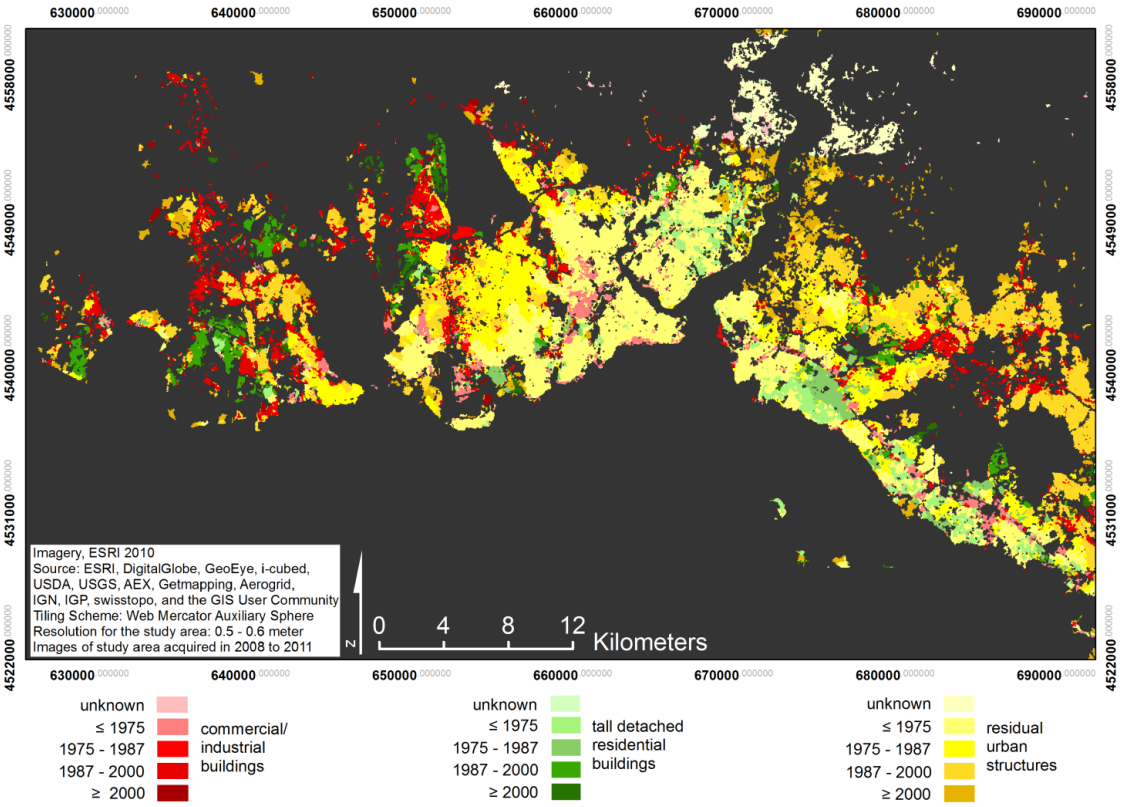

Figure 46: *Classification of urban structures of Istanbul with C-SVM for the highest obtainable accuracy combined with the year of construction.*

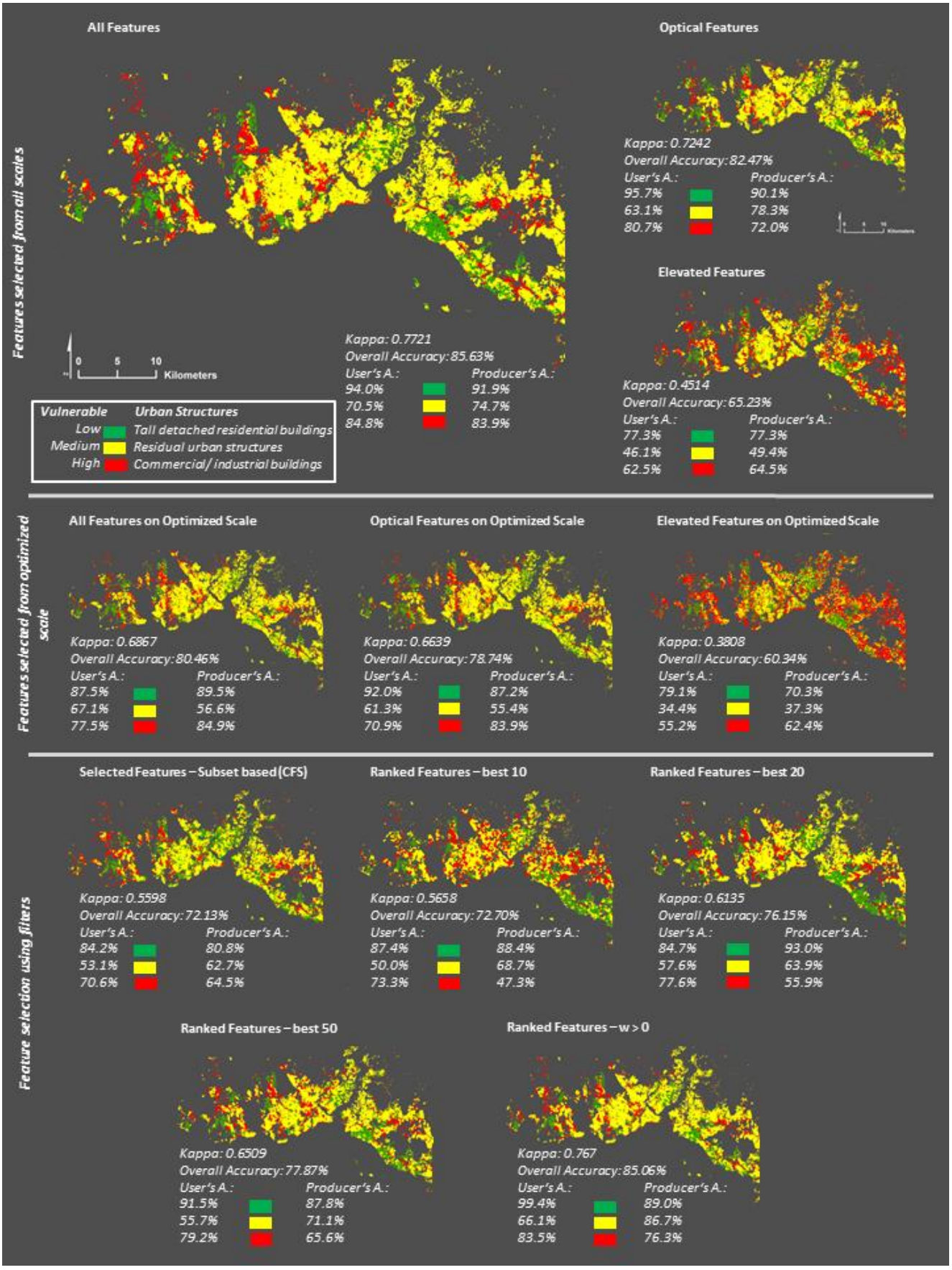

Figure 47: *Estimated class label with respect to seismic vulnerability using C-SVM on different feature sets.*

When comparing the best results from ν-OC-SVM and C-SVM the accuracies from C-SVM increased distinctively. This outcome was assumed due to more a prior knowledge within the C-SVM approach (i.e., information of three classes instead of one resp. two classes). Thereby, ν-OC-SVM could only yield moderate κ-statistics up to 0.45, where for C-SVM an outstanding κ-statistic (κ > 0.8), was obtainable. A κ > 0.8 indicates excellent accuracies (cf. chapter 7.1.4; GREVE & WENTURA, 1997). Furthermore, the classified urban structure types of C-SVM are spatially more cumulated than for ν-OC-SVM. In addition, the residual urban structure class of the ν-OC-SVM result is highly under-estimated with respect to the result of C-SVM. Generally the class tall detached residential buildings could be best estimated, which attest the gained high accuracies, compared to the other classes, in both classification results.

However, in real-life situations it is often the case that not all classes are known or not all samples are available. The ensemble of the applied ν-OC-SVM approach was implemented to tackle this problem with moderate accuracies of selected features. Therefore, the applied SVM approaches had shown that it is possible to estimate urban structures which are related to seismic vulnerability with moderate to excellent results regarding available a priori knowledge.

9. Conclusion and Outlook

Enduring urbanization processes and progressive agglomerations of buildings evoke the risk to be struck by seismic activity. Especially building conditions influence the seismic vulnerability. Many studies focused on the determination and inventory of seismic vulnerability of single buildings by means of remote sensing and in situ inventories (TAUBENBÖCK ET AL., 2009; BORZI ET AL., 2011; BORFECCHIA ET AL., 2009; WIELAND ET AL., 2012). Beside rapid transformations in the townscape and the extension of a city make it impossible to gather seismic building vulnerability for the entire area of large cities.

Hence, this study focused on the assessment of seismic vulnerability of so called homogeneous urban areas (i.e., agglomerated buildings with similar characteristics). Therefore, multi-sensor remote sensing data and in situ information were used for assessing seismic vulnerability of these urban structures. Based on optical data (i.e., RapidEye) and building height information (i.e., nDSM calculated by means of a DSM, derived from TanDEM-X) homogeneous urban structures were delineated by object-based image analysis. By means of remote sensing numerous features related to seismic vulnerability were derived and distinct feature sets compiled (i.e., quantitative and qualitative feature sets). Finally, within a framework of statistical learning (i.e., SVM) seismic vulnerability was estimated for different scenarios of a priori knowledge. This procedure was carried out for the Turkish mega city Istanbul.

Initially the building heights were derived by calculating a normalized DSM. This was further on used for the discrimination of homogeneous settlement units as well as for the calculation of seismic vulnerability features. Urban areas are generally composed of complex morphology. Frequently, homogeneous urban settlement units are irregularly shaped and sized, where fundamental segmentation techniques can not be used. The problem of delineating homogeneous urban areas was tackled by a multi-scale procedure, whilst taking into account the multispectral remote sensing data and building heights (i.e., nDSM). Subsequently, seismic vulnerability features were calculated and grouped according to their underlying remote sensing data (i.e., optical, elevation or both remote sensing data), segmentation scale and SVM-based feature selection methods (i.e., correlation based and feature ranking methods). Finally, the assessment of seismic vulnerability of homogeneous urban areas based on a

framework of approaches originated from SVM. Thereby, different settings for available reference data were assumed and applied in three different regression and classification scenarios (i.e., SVR, C-SVM, and an ensemble of ν-OC-SVM) to confirm their viability.

The regression analysis (i.e., SVR) for the district Zeytinburnu based on available aggregated single building in situ references composed of probable damage grades. The application gained an estimation of probable damage grads with a mean absolute percentage error less than 11% for an optimal feature set with a correlation coefficient of > 0.75. The SVM methods ν-OC-SVM and C-SVM aimed for the identification of specified classes of interest correlated with certain levels of seismic vulnerability. For the approach of ν-OC-SVM a sample set composed of only one class of interest for estimating the occurrence in the entire data set was used. In this study an ensemble of two ν-OC-SVMs (i.e., classification of commercial/ industrial urban structures and tall detached residential buildings) were used and combined for assessing Istanbul's seismic vulnerability. In contrast, the C-SVM method was used for a given sample set composed of 3 classes of interest: commercial/ industrial buildings considered as highly vulnerable, tall detached residential buildings considered as low vulnerable and residual buildings representing medium vulnerable urban structures. A comparison of the outcomes from C-SVM and ν-OC-SVM showed a moderate classification accuracy of κ below 0.5 for the ν-OC-SVM ensemble and an extremely high accuracy of the optimal applicable feature set of κ > 0.8 for the C-SVM method.

The utilization had shown that features derived from elevation data only, as well as from one segmentation scale only could not obtain viable models for classification. A combination of features derived from optical data and elevation data, or also features from optical data basis could gain much higher accuracies. Furthermore, the accuracies in all SVM studies were higher, when feature sets are derived from more than one segmentation scale. Nevertheless, in most cases (i.e., SVR and OC-SVM) feature set derived by a feature selection methods (e.g., Relief-F and CFS) was founded as optimal feature set (i.e., gathered the highest accuracies).

In conclusion, this study has shown that multi-sensor remote sensing can be used to delineate homogeneous urban areas and characterize them for the assessment of seismic vulnerability with viable results and high accuracies, in respect of available a priori knowledge.

Nevertheless, further developments in the methodological framework could gain enhanced accuracies, especially if only a few numbers of labeled samples are available. In this context a semi-supervised approach (e.g., BRUZZONE ET AL., 2006) with encode knowledge from unlabeled data may be beneficial (GEIß ET AL., 2014d). In addition, enhancements in the multi-scale segmentation technique may reduce remaining over-segmentation and could be compensate the application of additional segmentation scales. Especially the usage of OC-SVM necessitates further developments in the identification of finding the optimal free parameter settings for training the most suitable model, because the applied evaluation heuristic based on the overall accuracy and the model complexity (i.e., expressed by the number of support vectors). A more sophisticated approach may lead to higher accuracies if a more accurate parameter tuning could be reached.

From the conceptual perspective, different constructive forms of buildings impact seismic vulnerability (e.g., steel-reinforced, construction material). This information can not or just partly acquired with remote sensing such as the material of the building roof (e.g. with hyperspectral remote sensing). Therefore, in situ surveys by earthquake engineers are indispensable so that damage grades can be estimated, as the SVR approach indicated. However, by means of remote sensing different types of constructions can be identified in a relatively short timeframe. Hence, remote sensing data may be helpful for the estimation of seismic building vulnerability and can support lengthy and expensive in situ building assessments. Therefore, an exchange with experts in the field of earthquake engineering may profitable and could facilitate the assessment of seismic vulnerability in urban areas of larger extent.

Bibliography

A

ABE, S., (2005). Support vector machines for pattern classification (advances in pattern recognition). Springer, New York.

ANDERSON, E., THOMPSON, J., AUSTIN, R., (2005). LiDAR density and linear interpolator effects on elevatin estimates. In International Journal of Remote Sensing, Vol., 26, No. 18, pp. 3889-3900.

ALBERTZ, J., (1991). Einführung in die Fernerkundung – Grundlagen der Interpretation von Luft- und Satellitenbildern. Wissenschaftliche Buchgesellschaft Darmstadt, ISBN 3-534-19878-6.

ASTRIUM (2011). DEM products from TerraSAR-X & TanDEM-X. Retrieved July 4, 2014 from www.dgpf.de/neu/din/din2011/06_MeyerZuErpen_AstriumGEO.pdf.

AXELSSON, P., (1999). Processing of laser scanner data – algorithms and applications. In ISPRS Journal of Photogrammetry & Remote Sensing, Vol. 54, pp. 138-147.

B

BAATZ, M., SCHÄPE, A., (2000). Multiresolution Segmentation: an optimization approach for high quality multi-scale image segmentation. In Angewandte Geographische Informationsverarbeitung XII (Eds: Strobl, J. and Blaschke, T.), Beitrag zum AGIT-Symposium Salzburg 2000, Karlsruhe, Herbert Wichman Verlag, pp. 12-23.

BAATZ, M., SCHÄPE, A., SCHMIDT, G., ATHELOGOU, M., BINNIG, G., (2005). Cognition network, technology: Object orientation and fractal topology in biomedical image analysis. Methods and applications. In Fractals in Biology and Medicine, Vol. 4, pt 1, Losa, G., Merlini, D., Nonnenmacher, T, Weibel, E, (eds.), Basel, Switzerland, Birkhäuser Verlag, pp. 67-73.

BANSE, G., (1996). Herkunft und Anspruch der Risikoforschung. In Risikoforschung zwischen Disziplinarität und Interdisziplinarität, Banse,G.,(Eds.), Berlin, Edition Sigma, pp. 15-72.

BANZHAF, E., HÖFER, R., (2008). Monitoring Urban Structure Types as Spatial Indicators with CIR Aerial Photographs for a more effective urban environmental management. In IEEE Journal of Selected Topics in Applied Earth Observations and Remote Sensing, Vol. 1, No. 2, pp. 129-138.

BAUD, I., KUFFER, M., PFEFFER, K., SLIUZAS, R., KARUPPANNAN, S., (2010). Understanding heterogeneity in metropolitan India: The added value of remote sensing data for analyzing sub-standard residential areas. In International Journal of Applied Earth Observation and Geoinformation, Vol. 12, pp. 359-374.

BECHTEL, B., DANEKE, C., (2012). Classification of Local Climate Zones Based on Multiple Earth Observation Data. In IEEE Journal of Selected Topics in Applied Earth Observations and Remote Sensing, Vol. 5, No. 4, pp. 1191-1202.

BECK, U., (1986). Risikogesellschaft. Auf dem Weg in eine andere Moderne. Suhrkamp, Frankfurt a. M., ISBN 3-518-13326-8.

BENZ, U., HOFMANN, P., WILLHAUCK, G., LINGENFELDER, I., HEYNEN, M., (2004). Multi-resolution, object-oriented fuzzy analysis of remote sensing data for GIS-ready information. In ISPRS Journal of Photogrammetry & Remote Sensing, Vol. 58, pp. 239-258.

BERK, A., BERNSTEIN, L., ANDERSON, G., ACHARYA, P., ROBERTSON, D., CHETWYND , J., ADLER-GOLDEN, S., (1998). MODTRAN cloud and multiple scattering upgrade with application to AVIRIS – editions of 1991 and 1992. In Remote Sensing of Environment, Vol. 65, pp. 367-375.

BERRY, B. J. L., KIM, H.M. (1993). Challenges to the monocentric model. In Geographical Analysis (Impact Factor: 1.05), 09/2010, 25(1):1 - 4. DOI: 10.1111/j.1538-4632.1993.tb00275.x

BILHAM, R., (2009). The seismic future of cities. In Bulletin of Earthquake Engineering, Vol. 7, pp. 839–887.

BIRKMANN, J., (2006). Measuring Vulnerability to Natural Hazards – Towards Disaster Resilient Societies, New York, United Nations University, p. 524.

BLASCHKE, T., STROBL, J., (2001). What's wrong with pixels? Some recent developments interfacing remote sensing and GIS. In GIS-Zeitschriften für Geoinformations Systeme, Vol. 14, No. 6, pp. 12-17.

BLASCHKE, T., (2010). Object based image analysis for remote sensing. In ISPRS Journal of Photogrammetry and Remote Sensing, Vol. 65, pp. 2-16.

BLASCHKE, T., HAY, G., KELLY, M., LANG, S., HOFMANN, P., ADDINK, E., QUEIROZ FEITOSA, R., VAN DER MEER, F., VAN DER WERFF, VAN COILLIE, F., TIEDE, D., (2014). Geographic Object-Based Image Analysis – Towards a new paradigm. In ISPRS Journal of Photogrammetry and Remote Sensing, Vol. 87, No. 100, pp. 180-191.

BOCHOW, M., SEGL, K., KAUFMANN, H., (2007). Automating the build-up process of feature-based fuzzy logic models for the identification of urban biotopes from hyperspectral remote sensing data. In Urban Remote Sensing Joint Event, 2007, DOI: 10.1109/URS.2007.371800, pp. 1-8.

BOHLE, H.-G., (2001). Vulnerability and Criticality: Perspectives from social geography, IHDP Update 2/2001, Newsletter of the International Human Dimensions Programme on Global Environmental Change, Bonn.

BORFECCHIA, F., POLLINO, M., DE CECCO, L., LUGARI, A., MARTINI, S., LA PORTA, L., RISTORATORE, E., PASCALE, C., (2010). Active and passive remote sensing for supporting the evaluation of the urban seismic vulnerability. In Italian Journal of Remote Sensing, 42, pp. 129-141.

BORZI, B., DELL'ACQUA, F., FARAVELLI, M., GAMBA, P., LISINI, G., ONIDA, M., POLLI, D., (2011). Vulnerability study on a large industrial area using satellite remotely sensed images. In Bulletin of Earthquake Engineering, Vol. 9, pp. 675-690.

BROOKS, N., (2003). Vulnerability, Risk and Adaption: A conceptual framework. Working Paper 38. Tyndall Centre for Climate Change Research, Norwhich, UK, pp. 1-20.

BRUZZONE, L., CARLIN, L., (2006). A multilevel context-based system for classification of very high spatial resolution images. In IEEE Transactions on Geoscience and Remote Sensing, Vol. 44, No. 9, pp. 2587-2600.

BRUZZONE, L., CHI, M., MARCONCINI, M., (2006). A novel transductive SVM for supervised classification of remote-sensing images. In IEEE Transactions on Geoscience and Remote Sensing , Vol. 44, No. 11, pp. 3363-3373.

BURGES, C., (1998). A tutorial on support vector machines for pattern recognition. In Data Mining and Knowledge Discovery, Vol. 2, pp. 121-167.

C

CAKTI, E., (2013). Issues with the earthquake vulnerability of Istanbul. In Natural Hazards, Vol. 68, pp. 227-228.

CAMPBELL, J., (2002). Introduction to remote sensing. 3rd edition, The Guilford Press, ISBN 1-57230-640-8.

CAMPS-VALLS, G., BRUZZONE, L., (2005). Kernel-based methods for hyperspectral image classification. In IEEE Transactions on Geoscience and Remote Sensing, Vol. 43, pp. 1351-1362.

CAMPS-VALLS, G., BRUZZONE, L., (2009). Kernel methods for remote sensing data analysis. John Wiley & Sons.

CAMPS-VALLS, G., TUIA, D., BRUZZONE, L., BENEDIKTSSON, J., (2014). Advances in hyperspectral image classification: Earth monitoring with statistical learning methods. In IEEE Signal Processing Magazine, Vol. 31, No. 10, pp. 45-54.

CHABRIER, S., EMILE, B., ROSENBERGER, C., LAURENT, H., (2006). Unsupervised performance evaluation of image segmentation. In EURASIP Journal on Applied Signal Processing, pp. 1-12.

CHAMBERS, R., (1989). Editorial Introduction: Vulnerability, Coping, Policy. In IDS Bulletin, Vol. 20, No. 2, pp. 1-7.

CHANG, C.-C., LIN, C.-J., (2011). LibSVM: A library for support vector machines. Rerieved June 15, 2014 from http://www.csie.ntu.edu.tw/~cjlin/libsvm.

CHEN, Q., GONG, P., BALDOCCHI, D., XIE, G., (2007). Filtering Airborne Laser Scanning Data with Morphologiccal Methods. In Photogrammetric Engineering & Remote Sensing, Vol. 73, No. 2, pp. 175-185.

CHEN, C. H., HO, P.-G. P., (2008). Statistical pattern recognition in remote sensing. In Pattern Recognition, Vol. 41, No. 9, pp. 2731-2741.

CHRISTIANINI, N., SHAWE-TAYLOR, J., (2000). An introduction to support vector machines and other kernel-based learning methods. Cambridge University Press, 1st edition.

CIRACI, H., KUNDAK, S. (2000): Changing urban pattern of Istanbul: From monocentric to polycentric structure. In 40th Congress of the European Regional Science Association, Barcelona. Retrieved April 12, 2014 from http://ideas.repec.org/s/wiw/wiwrsa8.html.

COHENS, J., (1960). A coefficient of agreement for nominal scales. In Educational and Psychological Measurement, Vol. 20, pp. 37-64.

CORTES, C., VAPNIK, V. (1995). Support vector networks. In Machine Learning, Vol. 20, No. 3, pp. 273-297.

D

DEICHMANN, U., EHRLICH, D., SMALL, C., ZEUG, G., (2011). Using high resolution satellite data for the identification of urban natural disaster risk. In JRC, GFDRR, IPSC, WB, pp. 80.

DORREN, L., MAIER, B., SEIJMONSBERGEN, A., (2003). Improved Landsat-based forest mapping in steep mountainous terrain using object-based classification. In Forest Ecology and Management 183 (1-3), pp. 31-46.

DRAGUT, L., TIEDE, D., LEVICK, S., (2010). ESP: a tool to estimate scale parameter for multiresolution image segmentation or remotely sensed data. In International Journal of Geographical Information Science, 24:6, pp. 859-871.

DRAGUT, L., CSILLIK, O., EISANK, C., TIEDE, D., (2014). Automated parameterisation for multi-scale image segmentation on multiple layers. In ISPRS Journal of Photogrammetry and Remote Sensing, 88, pp. 119-127.

DRUCKER, H., BURGES, C., KAUFMAN, L., SMOLA, A, VAPNIK, V., (1997). Support vector regression machines. In Advances in Neural Information Processing Systems, Vol. 9, pp. 155-161.

E

ECHOVIEW (2014). About the GLCM and textures. Retrieved June 09, 2014 from

http://support.echoview.com/WebHelp/Reference/Algorithms/Operators/GLCM_textures/About_the_GLCM_and_textures.htm.

ERDIK, M. (2002). Earthquake risk assessment for Istanbul Metropolitan area. The American Red Cross – Turkish Red Crescent. Department of Earthquake Engineering, Bogazici University Istanbul, pp. 352.

ERDIK, M., (2002). Earthquake risk assessment for Istanbul Metropolitan Area. The American Red Cross – Turkish Red Crescent. Department of Earthquake Engineering, Bogazici University Istanbul.

ERDIK, M., DURUKAL, E., (2008). Earthquake risk and its mitigation in Istanbul. In Natural Hazards, Vol. 44, pp. 181-197.

ERDIK, M., BIRO, Y. A., ONUR, T., SESETYAN, K., BIRGOREN, G. (1999). Assessment of earthquake hazard in Turkey and neighboring regions. In Annali di Geofisica, Vol. 42, No. 6, pp. 1125-1138.

ERDIK, M., AYDINOGLU, N., FAHJAN, Y., SESETYAN, K., DEMIRCIOGLU, M., SIYAHI, B., DURUKAL, E., OZBEY, C., BIRO, Y., AKMAN, H., YUZUGULLU, O., (2003). Earthquake risk assessment for Istanbul metropolitan area. In Earthquake engineering and engineering vibration, Vol. 2, No. 1, pp. 1-23.

ERDIK, M. , DEMIRCIOGLU, M., SESETYAN, K., DURUKAL, E., SIYAHI, B. (2004). Earthquake hazard in Marmara region, Turkey. In 13th World Conference on Earthquake Engineering, Vancouver B.C., Canada, Paper No.: 270.

ESCH, T., THIEL, M., SCHENK, A., ROTH, A., MÜLLER, A., DECH, S., (2010). Delineation of Urban Footprints From TerraSAR-X Data by Analyzing Speckle Characteristics and Intensity Information. In IEEE Transactions on Geoscience and Remote Sensing, Vol. 48, No. 2, pp. 905-916.

ESCH, T., TAUBENBÖCK, H, ROTH, A., HELDENS, W., FELBIER, A., THIEL, M., SCHMIDT, M., MÜLLER, A., DECH, S., (2012). TanDEM-X mission – new perspectives for the inventory and monitoring of global settlement patterns. In Journal of Applied Remote Sensing, Vol. 6, pp. 1-21.

ESCH, T., THIEL, M., BOCK, M., ROTH, A., DECH, S., (2008). Improvement of Image Segmentation Accuracy based on multiscale optimization procedure. In IEEE Geoscience and Remote Sensing Letters, Vol. 5, No. 3, pp. 463- 467.

ESPINDOLA, G., CAMARA, G., REIS, I., BINS, L., MONTEIRO, A., (2006). Parameter selection for region growing image segmentation algorithms using spatial autocorrelation. In International Journal of Remote Sensing, Vol. 27, No. 14, pp. 3035-3040.

ESRI (N. D.). GIS Dictionary. Retrieved May 10, 2014 from http://support.esri.com/en/knowledgebase/GISDictionary/term/sliver%20polygon.

EXELIS (2014). Seamless Mosaic, retrieved at July 22, 2014 from www.exelisvis.com/docs/MosaicSeamless.html.

EXPLORATORIUM (2014). Faultline – Seismic Science at the epicenter: Damage control engineering. Retrieved August 1, 2014 from www.exploratorium.edu/faultline/damage/building.html.

F

FEMA310 (1998). Handbook for the Seismic Evaluation of existing buildings. Federal Emergency Management Agency (FEMA), Washington D.C., pp. 1-288.

FISCHHOFF, B., WATSON, S., HOPE, C., (1984). Defining risk. In Policy Sciences, Vol. 17, pp. 123-129.

FOTHERINGHAM, A., BRUNSDON, C., CHARLTON, M., (2000). Quantitative Geography: Perspectives on Spatial Analysis. Sage Publications, California.

FOODY, G., (2002). Status of land cover classification accuracy assessment. In Remote Sensing of Environment, Vol. 80, pp. 185-201.

FOODY, G., (2004). Thematic map comparison: evaluating the statistical significance of differences in classification accuracy. In Phtogrammetric Engineering and Remote Sensing, Vol. 70, pp. 627-633.

FRANCO, G., ALARCON, J. (2009). Izmit-Düzce ten years later: Is Istanbul at greater risk today. In AIR Worldwide, August 11, 2009. Retrieved April 13, 2014 from http://www.air-worldwide.com/Publications/AIR-Currents/Izmit-D%CF%8Bzce-Ten-Years-Later--Is-Istanbul-at-Greater-Risk-Today-/.

FRENCH, S., MUTHUKUMAR, S., (2006). Advanced technologies for earthquake risk inventories. In Journal of Earthquake Engineering, Vol. 10, pp. 207-236.

G

GALLOPIN, G., (2006). Linkages between vulnerability, resilience, and adaptive capacity. In Global Environmental Change, Vol. 16, pp. 293-303.

GALTON, F., (1886). Regression toward mediocrity in hereditary stature. In Journal of the Antropological Institute, Vol. 15, pp. 246-263.

GAMBA, P., HOUSHMAND, B., (2000). Digital Surface Models and Building extraction: A comparison of IFSAR and LIDAR data. In IEEE Transaction on Geoscience and Remote Sensing , Vol. 38, No. 4, pp. 1959-1968.

GAO, Y., KERLE, N., MAS, J., NAVARREE, A, NIEMEYER, I., (2007). Optimized image segmentation and its effect on classification accuracy. Retrieved April 5, 2014 from http://www.isprs.org/proceedings/xxxvi/2-c43/Postersession/gao_kerle_et_al.pdf.

GEISS, C., TAUBENBÖCK, H., (2013). Remote sensing contributing to assess earthquake risk: from a literature review towards a roadmap. In Natural Hazards, Vol. 68, pp. 7-48.

GEISS, C., TAUBENBÖCK, H., TYAGUNOV, S., TISCH, A., POST, J., LAKES, T., (2014a). Assessment of seismic building vulnerability from space. In Earthquake Spectra, in press. doi: http://dx.doi.org/10.1193/121812EQS350M.

GEISS, C., ARAVENA PELIZARI, P., MARCONCINI, M., SENGARA, W., EDWARDS, M., LAKES, T., TAUBENBÖCK, H., (2014b). Estimation of seismic buildings structural types using multi-sensor remote sensing and machine learning techniques. In ISPRS Journal of Photogrammetry and Remote Sensing, revisions.

GEISS, C., WURM, M., BREUNIG, M., FELBIER, A., TAUBENBÖCK, H., (2014c). Normalization of TanDEM-X DSM data in urban environments with morphological filters. In IEEE Transactions on Geoscience and Remote Sensing, in review.

GEISS, C., JILGE, M., LAKES, T., TAUBENBÖCK, H. (2014d). Seismic vulnerability assessment of urban structures with multi-sensor remote sensing. Submitted manuscript.

GEM, (2013). Global Earthquake Model, Inventory Data Capture Tools. Retrieved June 13, 2014 from www.globalquakemodel.org/risk-global-components/inventory-capture.

GIRGERT, W. (2008). Auf der Überholspur gen Westen. In Frankfurter Rundschau, October 13, 2008. Retrieved April 12, 2014 from http://www.fr-online.de/kultur/istanbul-auf-der-ueberholspur-gen-westen,1472786,3280368.html.

GLADE, T., MURTY, T., SCHENK, V., (2014). Natural Hazards. Vol. 73, Springer Netherlands.

GRAF, A., SMOLA, A., BORER, S., (2003). Classification in a normalized feature space using support vector machines. In IEEE Transactions on Neural Networks, Vol. 14, pp. 597-605.

GREVE, W., WENTURA, D., (1997). Wissenschaftliche Beobachtung – Eine Einführung. Beltz, Psycholgie VerlagsUnion.

GRÜNTHAL, G., (1998). European Macroseismic Scale 1998. In Cahiers du Centre Européen de Géodynamic et de Séismologie, Vol. 15, Luxembourg.

GUALTIERI, J., CROMP, R., (1998). Support vector machines for hyperspectral remote sensing classification. In Proceedings of the SPIE, Vol. 3584, pp. 221-232.

GUNN, S., (1998). Support Vector Machines for Classification and Regression, ISIS Technical Report, University of Southampton. Retrieved July, 19, 2014 from http://svms.org/tutorials/Gunn1998.pdf.

H

HALL, M., (1999). Correlation-based feature selection for machine learning. Ph.D. dissertation, Department of Computer Science, The University of Waikato, Hamilton, New Zealand.

HARALICK, R., SHANMUGAM, K., ITS 'HAK DINSTEIN, (1973). Textural Features for Image Classification. In IEEE Transactions on Systems, Man and Cybernetics, Vol. SMC-3, No., 6, pp. 610-621.

HEIDEN, U., HELDENS, W., ROESSNER, S., SEGL, K., ESCH, T., MUELLER, A., (2012). Urban structure type characterization using hyperspectral remote sensing and height information. In Landscape and Urban Planning, Vol. 105, pp. 361-375.

HELDENS, W., ESCH, T., HEIDEN, U., (2012). Supporting urban micro climate modelling with airborne hyperspectral data. In Proceedings of IEEE International Geoscience and Remote Sensing Symposium, July 23-27, 2012, Munich, Germany, pp. 1598-1601.

HEINRICHS, D., KABISCH, S., (2006). Risikolebensraum Megacity. Mitteilungen der HGF. GAIA 15/2. pp. 157-160.

HENGL, T., (2006). Finding the right pixel size. In Computers & Geosciences, 32, pp. 1283-1298.

HEROLD, M., LIU, X., CLARKE, K., (2003). Spatial metrics and image texture for mapping urban land use. In Photogrammetric Engineering and Remote Sensing, Vol. 69, pp. 991-1001.

HILDEBRANDT, G., (1996). Fernerkundung und Luftbildmessung: Für Forstwirtschaft Vegetationskartierung und Landschaftsökologie. Wichmann, Heidelberg.

HOOD, C., JONES, D., (1996). Accident and design: Contemporary debates in risk management. London, UCL-Press.

HSU, C., LIN, C., (2002). A comparison of methods for multi-class support vector machines. In IEEE Transactions on Neural Networks, Vol. 13, No. 2, pp. 415-425.

HSU, C.-W., CHANG, C.-C., LIN, C.-J., (2010). A practical guide to support vector classification. Technical report, Department of Computer Science, National Taiwan University.

HUGHES, G., (1968). On the mean accuracy of statistical pattern recognizers. In IEEE Transaction on Information Theory, Vol. IT-14, No. 1, pp. 55-63.

I

IAEE, NICEE, (2004). Guidelines for earthquake resistant non-engineered construction. Retrieved June 06, 2014 from www.traditional-is-modern.net./LIBRARY/GUIDELINES/1986IAEE-Non-EngBldgs/1986GuidelinesNon-Eng(ALL).pdf.

J

JENSEN, J., (2005). Digital Image Processing: A Remote Sensing Perspective. 3rd edition, Prentice Hall. ISBN 0-13-188950-8.

JINN.TV (2012). Sulukule Bizim Mahalle – Eine Einführung in den städteplanerischen Wahnsinn von Istanbul. In Academia.edu. Retrieved April 11, 2014 from https://www.academia.edu/2431330/Eine_Einfuhrung_in_den_stadteplanerischen_Wahnsinn_von_Istanbul.

JOHNSON, B., XIE, Z., (2011). Unsupervised image segmentation evaluation and refinement using a multi-scale approach. In ISPRS Journal of Photogrammetry and Remote Sensing, 66, pp. 473-483.

JOHNSON, B., XIE, Z., (2013). Classifying a high resolution image of an urban area using super-object information. In ISPRS Journal of Photogrammetry and Remote Sensing, Vol. 83, pp. 40-49.

K

KIM, M., MADDEN, M., WARNER, T., (2009). Forest type mapping using object-specific texture measures from multispectral IKONOS imagery: segmentation quality and image classification issues. In Photogrammetric Engineering & Remote Sensing, Vol. 75, No. 7, pp. 819-830.

KIM, M., MADDEN, M., XU, B., (2010). GEOBIA vegetation mapping in Great Smoky Mountains National park with spectral and non-spectral ancillary information. In Photogrammetric Engineering & Remote Sensing, Vol. 76, No. 2, pp. 137-149.

KÖHLER, W., (1929). Gestalt Psychology. New York: Liveright.

KOFFKA, K., (1935). Principles of Gestalt Psychology. New York: Harcourt, Brace.

KONONENKO, I., (1994). Estimating attributes: Analysis and extension of RELIEF. In Proceeding of the European Conference on Machine Learning, Springer, Catania, Italy, pp. 171-182.

KRAUSS, T., AREFI, H., REINARTZ, P., (2011). Evaluation of selected methods for extracting digital terrain models from satellite borne digital surface models in urban areas. In International Conference on Sensors and Models in Photogrammetry and Remote Sensing , SMPR.

KRAUS, K., PFEIFFER, N., (1998). Determination of terrain models in wooded areas with airborne laser scanner data. In ISPRS Journal of Photogrammetry & Remote Sensing, Vol. 53, pp. 193-203.

KRIEGER, G., FIEDLER, H., HAJNSEK, I., EINEDER, M., WERNER, M., MOREIRA, A., (2005). TanDEM-X: Mission Concept and Performance Analysis. In Geoscience and Remote Sensing Symposium, 2005. IGARSS '05. Proceedings. 2005 IEEE International, Vol. 7, pp. 4890-4893. .

L

LAM, N., (1983). Spatial interpolation methods: a review. In The American Cartographer, Vol. 10, No. 2, pp. 129-149.

LANG, S., BLASCHKE, T., (2003). Hierarchical object representation – comparative multi-scale mapping of anthropogenic and natural features. In ISPRS Archives, Vol. XXXIV, Part 3/W8, Munich, 17.-19. Sept. 2003, pp. 181- 186.

LEE, J.-S., (1983). Digital image smoothing and the sigma filter. In Computer Vision, Graphics and Image Processing, Vol. 24, No. 2, pp. 255-269.

LILLESAND, T., KIEFER, R., (2000). Remote Sensing and Image Interpretation. 4th edition, John Wiley & Sons, Inc.

LIU, D., XIA, F., (2010). Assessing object-based classification: advantages and limitations. In Remote Sensing Letters, Vol. 1, No. 4, pp. 187-194.

LIU, H., LI, J., WONG, L., (2002). A comparative study on feature selection and classification methods using gene expression profiles and proteomic patterns. In Genome Informatics, Vol. 13, pp. 51-60.

LIU, X., (2008). Airborne LiDAR for DEM generation: some critical issues. In Progress in Physical Geography, Vol. 32, pp. 31-49.

LIU, Y., SCHUMANN, M., (2005). Data mining feature selection for credit scoring models. In Journal of the Operational Research Society, pp. 1-10.

LLOYD, C., ATKINSON, P., (2010). Deriving DSMs from LiDAR data with kriging. In International Journal of Remote sensing, Vol. 23, No. 12, pp. 2519-2524.

LU, P., STUMPF, A., KERLE, N., CASAGLI, N., (2011). Object-oriented change detection for landslide rapid mapping . In IEEE Geoscience and Remote Sensing Letters, Vol. 8, No. 4, pp. 701-705.

LÜHR, G., MILKEREIT, C., PAROLAI, S., PICOZZI, M., WOITH, H., STROLLO, A., ERDIK, M., ANSAL, A., ZSCHAU, J. (2011). Sekunden für Istanbul – Vorhersage der Erdbeben-Bodenbewegung. System Erde, 1, 1, pp. 18-23, Retrieved April 20, 2014 from http://gfzpublic.gfz-potsdam.de/pubman/faces/viewItemFullPage.jsp?itemId=escidoc:23080.

M

MAGUYA, A., JUNTTILA, V., KAURANNE. (2013). Adaptive algorithm for large scale DTM interpolation from LiDAR data for forestry applications in steep forested terrain. In ISPRS Journal of Photogrammetry & Remote Sensing, Vol. 85, pp. 74-83.

MATHER, P., (2004). Computer Processing of Remotely-Sensed Images: An Introduction. 3rd edition, John Wiley.

MARCONCINI, M., FERNANDEZ-PRIETO, D., BUCHHOLZ, T., (2014). Targeted Land-cover Classification. In IEEE Transactions on Geoscience and Remote Sensing, Vol. 52, No. 7, pp. 4173-4193.

MARTHA, T., KERLE, N., VAN WESTEN, C., JETTEN, V., KUMAR, K., (2011). Segment Optimization and Data-Driven Thresholding for Knowledge-Based Landslide Detection by Object-Based Image Analysis. In IEEE Transactions on Geoscience and Remote Sensing, Vol. 49, No. 12, pp. 4928-4943.

MELGANI, F., BRUZZONE, L., (2004). Classification of hyperspectral remote sensing images with support vector machines. In IEEE Transactions on Geoscience and Remote Sensing, Vol. 42, No. 8, pp. 1778-1790.

MENG, X., CURRIT, N., ZHAO, K., (2010). Ground filtering algorithms for airborne LiDAR data: A review of critical issues. In Remote Sensing , Vol. 2, No. 3, pp. 833-860.

MERTINS, G., (1992). Urbanisierung, Metropolisierung und Megacities. Ursachen der Stadtexplosion in der Dritten Welt. In Deutsche Gesellschaft für die Vereinten Nationen (Eds.), Mega-Städte – Zeitbombe mit globalen Folgen?, Bonn, pp. 7-21.

MOREIRA, A., KRIEGER, G., HAJNSEK, I., HOUNAM, D., WERNER, M., (2004). TanDEM-X: a TerraSAR-X add-on satellite for single-pass SAR interferometry. In Geoscience and Remote Sensing Symposium, 2004. IGARSS '04. Proceedings. 2004 IEEE International, Vol. 2, pp. 1000-1003.

MOUNTRAKIS, G., IM, J., OGOLE, C., (2011). Support vector machines in remote sensing: a review. In ISPRS Journal of Photogrammetry and Remote Sensing, Vol. 66, pp. 247-259.

MÜLLER, M., SEGL, K., HEIDEN, U., KAUFMANN, H., (2006). Potential of high-resolution satellite data in the context of vulnerability of buildings. In Natural Hazards, Vol. 38, pp. 247-258.

MUNOZ-MARI, J., BOVOLO, F., GOMEZ-CHOVA, L., BRUZZONE, L., CAMPS-VALLS, G., (2010). Semi-supervised one-class support vector machines for classification of remote sensing data. In IEEE Transactions on Geoscience and Remote Sensing, Vol. 48, No. 8, pp. 3188-3197.

N

NEUBERT, M., MEINEL, G., (2005). Atmosphärische und topographische Korrektur von Ikonos-Daten mit ATCOR. In Angewandte Geoinformatik, 2005, Beiträge zum 17. AGIT-Symposium, Strobl, J., Blaschke, T., Griesebner, G. (Eds.), Salzburg, Wichmann, pp. 503-512.

NIEBERGALL, S., LOEW, A., MAUSER, W., (2008). Integrative Assessment of Informal Settlements using VHR Remote Sensing Data – The Delhi Case Study. In IEEE Journal of Selected Topics in Applied Earth Observations and Remote Sensing, Vol. 3, No. 1, pp. 193-205.

P

PACIFICI, F., CHINI, M., EMERY, W., (2009). A neural network approach using multi-scale textural metrics from very high resolution panchromatic imagery for urban land-use classification. In Remote Sensing of Environment , Vol. 113, No. 6, pp. 1276-1292.

PAL, R., PAL, K., (1993). A review on image segmentation techniques. In Pattern Recognition, Vol. 26, No. 9, pp. 1277-1294.

PARSONS, T. (2004). Recalculated probability of M≥7 earthquake beneath the Sea of Marmara, Turkey. In Journal of Geophysical Research, 109 (B05304), pp. 21.

PAULEIT, S., (1998). Das Umweltwirkgefüge städtischer Siedlungsstrukturen: Darstellung des städtischen Ökosystems durch einen Strukturtypenkartierung zur Bestimmung von Umweltqualitätszielen für die Stadtplanung. Dissertation, Technical University Munich.

PAULEIT, S., DUHME, F., (2000). Assessing the environmental performance of land cover types for urban planning. In Landscape and Urban Plannings, Vol. 52, pp. 1-20.

PEKKARINEN, A., (2002). A method for the segmentation of very high spatial resolution images of forested landscapes. In International Journal of Remote Sensing, 23, pp. 2817-2836.

PINGEL, T., CLARKE, K., McBRIDE, W., (2013). An improved simple morphological filter for the terrain classification of airborne LiDAR data. In ISPRS Journal of Photogrammetry & Remote Sensing, Vol. 77, pp. 21-30.

PITTORE, M., WIELAND, M., (2013). Towards a rapid probabilistic seismic vulnerability assessment using satellite and ground-based remote sensing. In Natural Hazards, Vol. 68, pp. 115-145.

R

RADOUX, J., DEFOURNY, P., (2008). Quality assessment results devoted to object-based classification. In Blaschke, T., Lang, S., Hay, G., (eds.), Object-based image analysis, spatial concepts for knowledge-driven remote sensing applications. Springer, Heidelberg, Berlin, New York, pp. 255-271.

RICHARDS, J., JIA, X., (2006). Remote Sensing Digital Analysis – An Introduction. 4rd edition, Springer, ISBN 3-540-25128-6.

RICHTER, R., (1996). A spatially adaptive fast atmospheric correction algorithm. In International Journal of Remote Sensing, Vol. 17, No. 6, pp. 1201-1214.

RICHTER, R., (2014).Problems with intermediate DEM from TanDEM-X for ATCOR-2. Written message (E-Mail) from February 24, 2014.

RICHTER, R., SCHLÄPFER, D., (2014). Atmospheric/ Topopgraphic Correction for Satellite Imagery – ATCOR-2/3 User Guide, Version 8.3.1, February 2014.

ROUSE Jr., J., HAAS, R., SCHELL, J., DERRING, D., (1974). Monitoring vegetation systems in the Great Plains with ERTS. In Goddard Space Flight Center 3rd ERTS-1 Symp., Vol. 1, Sect. A, pp. 309-317.

S

SAHAR, L., MUTHUKUMAR, S., FRENCH, P., (2010). Using aerial imagery and GIS in automated building footprint extraction and shape recognition for earthquake risk assessment of urban inventories. In IEEE Transactions on Geoscience and Remote Sensing, 48, pp. 3511-3520.

SALCEDO-SANZ, S., ROJO-ALVAREZ, J., MARTINEZ-RAMON, M., CAMPS-VALLS, G., (2014). Support vector machines in engineering: an overview. In Wiley Interdisciplinary Reviews: Data Mining and Knowledge Discovery, Vol. 4, No. 3, pp. 234-267.

SARABANDI, P., KIREMIDJIAN, A., EGUCHI, R., ADAMS, B., (2008). Building inventory compilation for disaster management: Application of remote sensing and statistical modeling. In Technical Report Series MCEER-08-0025, MCEER: Buffalo.

SCHÖLKOPF, B., WILLIAMSON, R., SMOLA, A., SHAWE-TAYLOR, J., PLATT, J., (2000). Support vector method for novelty detection. In Advances in Neural Information Processing Systems, Vol. 12, No. 3, pp. 582-588.

SCHÖLKOPF, B., PLATT, J., SHAWE-TAYLOR, J., SMOLA, A., WILLIAMSON, R., (2001). Estimating the support of a high dimensional distribution. In Neural Computation, Vol. 13, No. 7, pp. 1443-1471.

SCHÖLKOPF, B., SMOLA, A., (2002). Learning with kernels: support vector machines, regularization, optimization, and beyond. MIT Press, Cambridge (MA).

SCHÖLKOPF, B., SMOLA, A., (2004). A tutorial on support vector regression. In Statistics and Computing, Vol. 14., pp. 199-222.

SCHOWENGERDT, R., (1997). Remote Sensing – Models and Methods for Image Processing. 2nd edition, Academic Press, San Diego.

SCHOWENGERDT, R., (2006). Remote Sensing – Models and Methods for Image Processing, 3rd edition, Elsevier, Academic Press.

SIRMACEK, B., TAUBENBÖCK, H., REINARTZ, B., EHLERS, M., (2012). Performance Evaluation for 3-D City Model Generation of six different DSMs from Air-and Spaceborne Sensors. In IEEE Journal of selected Topics in Applied Earth Observation and Remote Sensing, Vol. 5, No. 1, pp. 59-70.

SITHOLE, G., VOSSELMAN, G., (2004). Experimental comparison of filter algorithms for bare-earth extraction from airborne laser scanning point clouds. In ISPRS Journal of Photogrammetry & Remote Sensing, Vol. 59, pp. 85-101.

STEIN, A., DE BEURS, K., (2005). Complexity metrics to quantify semantic accuracy in segmented Landsat images. In International Journal of Remote Sensing 26 (14), pp. 2937-2951.

STEINIGER, S., LANGE, T., BURGHARDT, D., WEIBEL, R., (2008). An approach for the classification of urban building structures based on discriminant analysis techniques. In Transactions in GIS, Vol. 12, No. 1, pp. 31-59.

T

TANG, Y., (2007). An integrated GIS-spatial analysis of Atlanta's urban structure and urban space. PhD thesis. Unviersity of Georgia, USA.

TAUBENBÖCK, H., (2007). Vulnerabilitätsabschätzung der erdbebengefährdeten Megacity Istanbul mit Methoden der Fernerkundung. PhD thesis, University Würzburg.

TAUBENBÖCK, H. (2007). Vulnerabilitätsabschätzung der erdbebengefährdeten Megacity Istanbul mit Methoden der Fernerkundung. Dissertation, pp. 13, Julius-Maximilians University Würzburg.

TAUBENBÖCK, H., ROTH, A., DECH, S., MEHL, H., MÜNICH, J., STEMPNIEWSKI, L., ZSCHAU, J., (2009). Assessing building vulnerability using synergistically remote sensing and civil engineering. In Urban and Regional Data Management, Kreck, A., Rumor, M., Zlatanova, S., and Fendel, E. (Eds.), Taylor & Francis Group, London, pp. 287-300.

TAUBENBÖCK, H., ESCH, T., FELBIER, A., ROTH, A., DECH, S., (2011). Pattern-based accuracy assessment of an urban footprint classification using TerraSAR-X data. In IEEE Geoscience and Remote Sensing Letters. 8 (2), pp. 278-282.

TAX, D., DUIN, R., (1999). Support vector domain description. In Pattern Recognition Letter, Vol. 20, No. 11-13, pp. 1191-1199.

TERME, L. (2013). Istanbul TALRAUM – nachhaltige städtebauliche und landschaftliche Entwicklung in Tälern am Bosporus. Master-Thesis, Technical University of Munich.

TOBLER, W., (1970). A computer movie simulating urban growth in the Detroit region. In Economic Geography, Vol. 46, pp. 234-40.

TRIMBLE (2011). eCognition Developer 8.7 – Reference Book. Publisher: Trimble Germany GmbH, Munich, Germany.

TUCKER, C., (2004). NASA's global orthorectified Landsat data set. In Photogrammetric Engineering and Remote Sensing, Vol. 70, pp. 313-322.

TURKSTAT (2014). Turkish statistical institute. Retrieved April 11, 2014 from http://www.turkstat.gov.tr.

TZOTSOS, A. (2006). A support vector machine approach for object based image analysis. In ISPRS Archivs, Vol. XXXVI-4/C42, 2006 – Bridging Remote Sensing and GIS 1st International Conference on Object-based Image Analysis (OBIA 2006), Salzburg.

TZOTSOS, A., ARGIALAS, D., (2008). Support Vector Machine Classification for Object-Based Image Analysis. In Object-based image analysis spatial concepts for knowledge-driven remote sensing applications, Eds. T. Blaschke, S. Lang & G. Hay, pp. 663-677. Berlin. Springer.

U

UNITED NATIONS (1991). Mitigating Natural Disasters: Phenomena, Effects, and Options: A manual for Policy Makers and Planners. New York: UNDRO (United Nations Disaster Relief Organization), pp. 1-64.

UNITED NATIONS, (2003). World Urbanization Prospects – The 2003 revision. Department of Economic and Social Affairs, New York, ST/ESA/SER.A/237, ISBN 92-1-141396-0.

UNITED NATIONS POPULATION FUND (2007). Urbanization: A Majority in cities. Retrieved April 20, 2014 from http://unfpa.org/pds/urbanization.htm.

UNITED NATIONS DEVELOPMENT PROGRAMME (UNPD), (1994). 1. Seismic Hazard Mapping and Risk Assessment for Nepal, 2. Development of Alternative Building Materials and Technologies 3. Seismic vulnerability analysis (Appendix c). Subproject NEP/88/054/21.03, 1994. His Majesty's Govt. of Nepal, Ministry of Housing and Physical Planning, UNPD/UNCHS Habitat. In Assessing building vulnerability for earthquake using field survey and development control data: a case study in Lalitpur sub-metropolitan city, Nepal, R. Thapaliya, Masterthesis, International Institute for Geo-Information Science and Earth Observation, Enschede, The Netherlands.

UNITED NATIONS DEVELOPMENT PROGRAMME (UNPD) (2004). Reducing disaster risk – A challenge for development: A global report. ISBN 92-1-126160-0, New York, USA.

UNITED NATIONS/ISDR (International Strategy for Disaster Reduction), (2004). Living with risk: A global review of disaster reduction initiatives. United Nations International Strategy for Disaster Reduction, Version 2004, Vo. 1, Geneva, Switzerland: UN Publications.

UNITED NATIONS/ISDR (International Strategy for Disaster Reduction), (2013). On-Line Conference – Terminology: Basic terms of disaster risk reduction. Retrieved August 2, 2014 from www.unisdr.org/2004/wcdr-dialogue/terminology.htm.

UNITED NATIONS (2014). World Urbanization Prospects: The 2014 Revision, Highlights. Department of Economic and Social Affairs, Population Devision, New York, ST/ESA/SER.A/352, ISBN 978-92-1-151517-6.

UNITED STATES CENSUS BUREAU, (2014). U.S. and World Population Clock. Retrieved July 29, 2014 from www.census.gov/popclock.

UNIVERSITY UTRECHT (N. D.). Chapter 10 – Segmentation. Retrieved May 5, 2014 from www.cs.uu.nl/docs/vakken/ibv/reader/chapter10.pdf.

U.S. GEOLOGICAL SURVEY (USGS) (2014). Earthquake Hazard Program: Latest Earthquakes. Retrieved July 30, 2014 from http://earthquake.usgs.gov/.

V

VAPNIK, V., (1995). The nature of statistical learning theory. Springer.

VAPNIK, V., (1998). Statistical learning theory. Wiley, New York, 1st edition.

VERRELST, J., MUŇOZ-MARI, J., ALONSO, L., DELEGIDO, J. RIVERA, J., CAMPS-VALLS, G., MORENO, J., (2012). Machine learning regression algorithms for biophysical parameter retrieval: Opportunities for Sentinel-2 and -3. In Remote Sensing of Environment, Vol. 118, pp. 127-139.

VOLPI, M., TUIA, D., BOVOLO, F., KANEVSKI, M., BRUZZONE, L., (2013). Supervised change detection in VHR images using contextual information and support vector machines. In International Journal of Applied Earth Observation and Geoinformation, Vol. 20, pp. 77-85.

VOZIKIS, G., (2004). Urban Data Collection: An Automated Approach in Remote Sensing. In Application of high resolution remote sensing data – Part III, Chapter 2, Vienna University of technology, Austria: Institute of Photogrammetry and Remote Sensing, pp. 101-110.

W

WASKE, B., BRAUN, M., (2009). Classifier ensembles for land cover mapping using multitemporal SAR imagery. In ISPRS Journal of Photogrammetry and Remote Sensing, Vol. 64, No. 5, pp. 450-457.

WATSON, D., PHILIP, G., (1985). A refinement of inverse distance weighted interpolation. In Geo-Processing, Vol. 2, pp. 315-327.

WEBER, M., HERRMANN, J., HAJNSEK, I., MOREIRA, A., (2006). TerraSAR-X and TanDEM-X: Global Mapping in 3D using Radar. In Proc. Second Int. Workshop “The future of remote sensing“, pp. 36-1.

WERTHEIMER, M., (1923). Untersuchungen zur Lehre von der Gestalt II. In Psycholgische Forschung, Vol. 4, No. 1, pp. 301-350.

WICKOP, E., BÖHM, P., EITNER, K., BREUSTE, J., (1998). Qualitätszielkonzept für Stadtstrukturen am Beispiel der Stadt Leipzig (Benchmark concept for urban structure types – A case study of the city of Leipzig). UFZ technical report 14.

WIELAND, M., PITTORE, M., PAROLAI, S., ZSCHAU, J., MOLDOBEKOV, B., BEGALIEV, U., (2012). Estimating building inventory for rapid seismic vulnerability assessment: towards an integrated approach based on multisource imaging. In Soil Dynamics and Earthquake Engineering, Vol. 36, pp. 70-83.

WITTIG, R., SUKOPP, H., KLAUSNITZER, B., (1998). Die ökologische Gliederung der Stadt. In Stadtökologie – Ein Fachbuch für Studium und Praxis, Ed. 2, Sukopp, H., & Wittig, R., pp. 316-372.

WURM, M., TAUBENBÖCK, H., ROTH, A., DECH, S., (2009). Urban structuring using multisensoral remote sensing data. Urban Remote Sensing Event, 2009, Shanghai, China, pp. 1-8.

WURM, M., TAUBENBÖCK, H., SCHARDT, M., ESCH, T., DECH, S., (2011). Object –based image information fusion using multisensor earth observation data over urban areas. In International Journal of Image and Data Fusion, Vol., 2, No., 2, pp. 121-147.

Y

YU, Q., GONG, P., CHINTON, N., BIGING, G., KELLY, M., SCHIROKAUER, D., (2006). Object-based detailed vegetation classification with airborne high spatial resolution remote sensing imagery. In Photogrammetric Engineering & Remote Sensing, Vol. 72, No. 7, pp. 799-811.

Z

ZHANG, Y., (1997). Evaluation and comparison of different segmentation algorithms. In Pattern Recognition Letters, Vol. 18, No. 10, pp. 963-974.

ZHANG, K., CHEN, S.-C., WHITMAN, D., SHYU, M.-L., YAN, J., ZHANG, C., (2003). A progressive morphological filter for removing nonground measurements from airborne LiDAR data. In IEEE Transaction on Geoscience & Remote Sensing, Vol., 41, No. 4, pp. 872-882.

ZHANG, Y., MAXWELL, T., TONG, H., DEY, V., (2010). Development of a supervised software tool for automated determination of optimal segmentation parameters for eCognition. In Wagner, W., Székely, B. (eds): ISPRS TC VII Symposium – 100 Years ISPRS Vienna, Austria, July 5-7, 2010. IAPRS, Vol. XXXVIII, Part 7B.

ZINK, M., KRIEGER, G., FIEDLER, H., HAJNSEK, I., MOREIRA, A., (2008). The TanDEM-X Mission Concept. In Synthetic Aperture Radar (EUSAR), 2008 7th European Conference in Friedrichshafen/ Germany, pp. 1-4.

ZSCHAU, J. JSIKARA, M., ERGÜNAY, O, YALCIN, M., ERDIK, M., (2002). Towards an earthquake early warning system for the megacity Istanbul. In Early Warning Systems for Natural Disaster Reduction, Zschau, J., Küppers, A., (Eds.), Springer, pp. 433-440.

Appendix

Appendix A:

Scale factor	number of objects	number of non-valid objects	percentage of non-valid objects	delta
5	252415	252324	99.96394826	-
6	175024	174254	99.56006033	0.403887925
7	127796	124876	97.71510845	1.84495188
8	96685	90131	93.22128562	4.493822836
9	75293	64740	85.98408883	7.237196792
10	59865	46031	76.89133885	9.092749981
11	48539	32433	66.81843466	10.07290418
12	40128	22996	57.30661882	9.511815841
13	33611	16310	48.52578025	8.780838569
14	28449	11609	40.80635523	7.719425018
15	24254	8264	34.07273027	6.733624961
16	20979	5973	28.47132847	5.6014018
17	18369	4427	24.10038652	4.370941951
18	16073	3247	20.20158029	3.898806231
19	14255	2468	17.31322343	2.88835686
20	12707	1879	14.78712521	2.526098224
21	11419	1487	13.02215606	1.764969151
22	10252	1178	11.49044089	1.531715166
23	9333	955	10.2325083	1.257932586
24	8529	778	9.121819674	1.11068863
25	7779	641	8.240133693	0.881685981
26	7101	509	7.168004506	1.072129187
27	6520	409	6.273006135	0.894998371
28	5998	343	5.718572858	0.554433277
29	5551	285	5.134210052	0.584362805
30	5202	251	4.825067282	0.30914277
31	4819	203	4.212492218	0.612575064
32	4527	172	3.799425668	0.41306655
33	4288	147	3.428171642	0.371254026
34	4027	125	3.104047678	0.324123964
35	3777	109	2.885888271	0.218159407
36	3568	97	2.718609865	0.167278406
37	3373	89	2.638600652	0.080009213
38	3195	82	2.566510172	0.07209048
39	3050	72	2.360655738	0.205854434
40	2904	62	2.134986226	0.225669512
41	2750	55	2	0.134986226
42	2612	44	1.684532925	0.315467075
43	2496	36	1.442307692	0.242225233
44	2401	33	1.374427322	0.06788037
45	2302	30	1.303214596	0.071212726
46	2204	25	1.13430127	0.168913326
47	2127	23	1.081335214	0.052966057
48	2032	23	1.131889764	-0.05055455
49	1961	21	1.070882203	0.061007561
50	1893	19	1.003697834	0.067184369

Appendix A: *Percentage of non-valid objects for the scales h=5 to h=50, to determine initial segmentation scale.*

Appendix B:

scale factor	v	I	v_{norm}	I_{norm}	F(v,I)
24	146.22	0.000260	1	0.927325581	1.927325581
25	149.24	0.000254	0.9612423	0.944767442	1.906009742
26	152.22	0.000250	0.9229979	0.956395349	1.879393295
27	154.90	0.000247	0.8886037	0.965116279	1.853719975
28	157.54	0.000238	0.8547228	0.991279070	1.846001862
29	160.18	0.000240	0.8208419	0.985465116	1.806307005
30	162.41	0.000243	0.7922228	0.976744186	1.768966979
31	164.64	0.000248	0.7636037	0.962209302	1.725812998
32	166.78	0.000251	0.7361396	0.953488372	1.689628002
33	168.66	0.000260	0.7120123	0.927325581	1.639337902
34	170.71	0.000266	0.6857033	0.909883721	1.595587006
35	172.73	0.000272	0.6597793	0.892441860	1.552221121
36	174.45	0.000277	0.6377053	0.877906977	1.515612316
37	176.26	0.000281	0.6144764	0.866279070	1.480755456
38	177.92	0.000287	0.5931725	0.848837209	1.442009694
39	179.55	0.000295	0.5722536	0.825581395	1.397834989
40	180.88	0.000302	0.5551848	0.805232558	1.360417363
41	182.12	0.000310	0.5392710	0.781976744	1.321247791
42	183.42	0.000320	0.5225873	0.752906977	1.275494246
43	184.65	0.000328	0.5068018	0.729651163	1.236453011
44	186.05	0.000337	0.4888347	0.703488372	1.192323074
45	187.32	0.000345	0.4725359	0.680232558	1.152768492
46	188.74	0.000343	0.4543121	0.686046512	1.140358627
47	189.94	0.000352	0.4389117	0.659883721	1.098795425
48	191.06	0.000350	0.4245380	0.665697674	1.090235662
49	192.21	0.000358	0.4097793	0.642441860	1.052221121
50	193.34	0.000395	0.3952772	0.534883721	0.930160928
51	194.32	0.000402	0.3827002	0.514534884	0.897235089
52	195.17	0.000410	0.3717916	0.491279070	0.863070651
53	196.16	0.000419	0.3590862	0.465116279	0.824202521
54	196.78	0.000425	0.3511294	0.447674419	0.798803782
55	197.74	0.000433	0.3388090	0.424418605	0.763227640
56	198.56	0.000440	0.3282854	0.404069767	0.732355188
57	199.52	0.000447	0.3159651	0.383720930	0.699686023
58	200.26	0.000454	0.3064682	0.363372093	0.669840266
59	200.97	0.000460	0.2973563	0.345930233	0.643286495
60	201.83	0.000467	0.2863193	0.325581395	0.611900697
61	202.48	0.000474	0.2779774	0.305232558	0.583209971
62	203.17	0.000485	0.2691222	0.273255814	0.542377991
63	203.67	0.000491	0.2627053	0.255813953	0.518519292
64	204.26	0.000498	0.2551335	0.235465116	0.490598587
65	204.81	0.000503	0.2480749	0.220930233	0.469005181
66	205.21	0.000508	0.2429415	0.206395349	0.449336827
67	205.82	0.000512	0.2351129	0.194767442	0.429880378
68	206.20	0.000517	0.2302361	0.180232558	0.410468698
69	206.68	0.000523	0.2240760	0.162790698	0.386866673
70	207.20	0.000528	0.2174025	0.148255814	0.365658278
71	207.76	0.000534	0.2102156	0.130813953	0.341029559
72	208.27	0.000539	0.2036704	0.116279070	0.319949501
73	208.79	0.000543	0.1969969	0.104651163	0.301648083
74	209.28	0.000547	0.1907084	0.093023256	0.283731675
75	209.75	0.000550	0.1846766	0.084302326	0.268978917
76	210.14	0.000553	0.1796715	0.075581395	0.255252853
77	210.65	0.000554	0.1731263	0.072674419	0.245800702
78	211.00	0.000558	0.1686345	0.061046512	0.229681009
79	211.47	0.000560	0.1626027	0.055232558	0.217835228
80	211.71	0.000563	0.1595226	0.046511628	0.206034215
81	212.08	0.000563	0.1547741	0.046511628	0.201285755
82	212.37	0.000564	0.1510524	0.043604651	0.194657013
83	212.67	0.000566	0.1472023	0.037790698	0.184992956
84	213.01	0.000571	0.1428388	0.023255814	0.166094623
85	213.37	0.000573	0.1382187	0.017441860	0.155660546
86	213.66	0.000573	0.1344969	0.017441860	0.151938780

87	213.99	0.000575	0.1302618	0.011627907	0.141889714
88	214.20	0.000575	0.1275667	0.011627907	0.139194642
89	214.60	0.000575	0.1224333	0.011627907	0.134061172
90	214.93	0.000575	0.1181982	0.011627907	0.129826059
91	215.26	0.000577	0.1139630	0.005813953	0.119776993
92	215.62	0.000577	0.1093429	0.005813953	0.115156869
93	215.83	0.000576	0.1066478	0.008720930	0.115368774
94	215.98	0.000579	0.1047228	0	0.104722793
95	216.17	0.000579	0.1022844	0	0.102284394
96	216.41	0.000579	0.0992043	0	0.099204312
97	216.59	0.000534	0.0968943	0.130813953	0.227708204
98	216.84	0.000533	0.0936858	0.133720930	0.227406762
99	217.06	0.000532	0.0908624	0.136627907	0.227490330
100	217.48	0.000530	0.0854723	0.142441860	0.227914140
101	217.83	0.000524	0.0809805	0.159883721	0.240864214
102	218.15	0.000523	0.0768737	0.162790698	0.239664414
103	218.27	0.000521	0.0753337	0.168604651	0.243938327
104	218.38	0.000518	0.0739220	0.177325581	0.251247553
105	218.54	0.000516	0.0718686	0.183139535	0.255008118
106	218.69	0.000515	0.0699435	0.186046512	0.255990043
107	218.87	0.000511	0.0676335	0.197674419	0.265307889
108	218.98	0.000509	0.0662218	0.203488372	0.269710138
109	219.12	0.000504	0.0644251	0.218023256	0.282448307
110	219.23	0.000499	0.0630133	0.232558140	0.295571487
111	219.30	0.000497	0.0621150	0.238372093	0.300487083
112	219.52	0.000493	0.0592916	0.250000000	0.309291581
113	219.70	0.000487	0.0569815	0.26744186	0.324423380
114	219.95	0.000485	0.0537731	0.273255814	0.327028915
115	220.02	0.000483	0.0528747	0.279069767	0.331944511
116	220.10	0.000477	0.0518480	0.296511628	0.348359677
117	220.30	0.000474	0.0492813	0.305232558	0.354513872
118	220.34	0.000470	0.0487680	0.316860465	0.365628432
119	220.42	0.000464	0.0477413	0.334302326	0.382043599
120	220.54	0.000458	0.0462012	0.351744186	0.397945418
121	220.79	0.000453	0.0429928	0.366279070	0.409271883
122	220.90	0.000450	0.0415811	0.375000000	0.416581109
123	221.06	0.000444	0.0395277	0.392441860	0.431969581
124	221.10	0.000440	0.0390144	0.404069767	0.443084141
125	221.36	0.000434	0.0356776	0.421511628	0.457189246
126	221.48	0.000434	0.0341376	0.421511628	0.455649205
127	221.59	0.000429	0.0327259	0.436046512	0.468772384
128	221.67	0.000420	0.0316992	0.462209302	0.493908481
129	221.80	0.000413	0.0300308	0.482558140	0.512588940
130	222.00	0.000402	0.0274641	0.514534884	0.541998949
131	222.08	0.000397	0.0264374	0.529069767	0.555507139
132	222.28	0.000390	0.0238706	0.549418605	0.573289241
133	222.45	0.000380	0.0216889	0.578488372	0.600177284
134	222.63	0.000371	0.0193789	0.604651163	0.624030013
135	222.84	0.000367	0.0166838	0.616279070	0.632962848
136	222.96	0.000360	0.0151437	0.636627907	0.651771644
137	223.21	0.000351	0.0119353	0.662790698	0.674726016
138	223.25	0.000344	0.0114220	0.683139535	0.694561506
139	223.28	0.000340	0.0110370	0.694767442	0.705804403
140	223.34	0.000335	0.0102669	0.709302326	0.719569266
141	223.45	0.000324	0.0088552	0.741279070	0.750134306
142	223.58	0.000312	0.0071869	0.776162791	0.783349649
143	223.62	0.000305	0.0066735	0.796511628	0.803185139
144	223.70	0.000297	0.0056468	0.819767442	0.825414259
145	223.75	0.000291	0.0050051	0.837209302	0.842214436
146	223.79	0.000286	0.0044918	0.851744186	0.856235972
147	223.83	0.000272	0.0039784	0.892441860	0.896420300
148	223.96	0.000256	0.0023101	0.938953488	0.941263550
149	224.04	0.000244	0.0012834	0.973837209	0.975120577
150	224.14	0.000235	0	1	1

v_{min} = 146.22	v_{max} = 224.14	I_{min}= 0.000235	I_{max} = 0.000579
	σ (F(v,I)) = 0.49542975	$F(v,I)_{max}$ = 1.927325581	F(p) = 1.431895832

Appendix B: *Calculation of objective function for h=24 to h=15.*

Appendix C:

scale factor	v	I	v_{norm}	I_{norm}	F(v,I)
24	989,06	0,000817	1	0	1
25	1137,84	0,000772	0,816551996	0,260115607	1,076667603
26	1183,72	0,00076	0,759981258	0,329479769	1,089461027
27	1230,49	0,000746	0,702313137	0,410404624	1,112717761
28	1276,29	0,000735	0,64584104	0,473988439	1,119829479
29	1328,16	0,000723	0,58188454	0,543352601	1,125237142
30	1378,4	0,000711	0,519937856	0,612716763	1,132654619
31	1432,05	0,000701	0,45378659	0,670520231	1,124306821
32	1484,82	0,000691	0,388720377	0,728323699	1,117044076
33	1538,25	0,000682	0,322840374	0,780346821	1,103187195
34	1586,89	0,000673	0,262866514	0,832369942	1,095236456
35	1638,96	0,000664	0,198663412	0,884393064	1,083056475
36	1688,26	0,000658	0,137875761	0,919075145	1,056950906
37	1743,89	0,000652	0,069283125	0,953757225	1,02304035
38	1800,08	0,000644	0	1	1

v_{min} = 989.06 v_{max} = 1800.08 I_{min}= 0.000644 I_{max} = 0.000817

σ (F(v,I)) = 0.043229139 $F(v,I)_{max}$ = 1.132654619 F(p) = 1.08942548

Appendix C: *Calculation of optimized function for h=24 to h=38.*

Appendix D:

Feature	Key for naming		
Features derived from optical data	**optimized scale**	**h=80**	**h=120**
Measure of central tendency			
mean *{Brightness}*	O_Lmean_br	OLmean_br8	OLmean_br1
mean *{Max.diff}*	O_Lmaxdiff	OLmaxdiff8	OLmaxdiff1
mean *{R}*	O_Lmean_r	OLmean_r8	OLmean_r1
mean *{G}*	O_Lmean_g	OLmean_g8	OLmean_g1
mean *{B}*	O_Lmean_b	OLmean_b8	OLmean_b1
mean *{NIR}*	O_Lmean_i	OLmean_i8	OLmean_i1
quartile50 *{R}* (median)	O_Lmed_r	OLmed_r8	OLmed_r1
quartile50 *{G}* (median)	O_Lmed_g	OLmed_g8	OLmed_g1
quartile50 *{B}* (median)	O_Lmed_b	OLmed_b8	OLmed_b1
quartile50 *{NIR}* (median)	O_Lmed_i	OLmed_i8	OLmed_i1
Measure of spread			
variance *{R}*	O_Svar_r	OSvar_r8	OSvar_r1
variance *{G}*	O_Svar_g	OSvar_g8	OSvar_g1
variance *{B}*	O_Svar_b	OSvar_b8	OSvar_b1
variance *{NIR}*	O_Svar_i	OSvar_i8	OSvar_i1
standard deviation *{R}*	O_Sstdv_r	OSstdv_r8	OSstdv_r1
standard deviation *{G}*	O_Sstdv_g	OSstdv_g8	OSstdv_g1
standard deviation *{B}*	O_Sstdv_b	OSstdv_b8	OSstdv_b1
standard deviation *{NIR}*	O_Sstdv_i	OSstdv_i8	OSstdv_i1
minimum pixel value *{R}*	O_Smin_r	OSmin_r8	OSmin_r1
minimum pixel value *{G}*	O_Smin_g	OSmin_g8	OSmin_g1
minimum pixel value *{B}*	O_Smin_b	OSmin_b8	OSmin_b1
minimum pixel value *{NIR}*	O_Smin_i	OSmin_i8	OSmin_i1
maximum pixel value *{R}*	O_Smax_r	OSmax_r8	OSmax_r1
maximum pixel value *{G}*	O_Smax_g	OSmax_g8	OSmax_g1
maximum pixel value *{B}*	O_Smax_b	OSmax_b8	OSmax_b1
maximum pixel value *{NIR}*	O_Smax_i	OSmax_i8	OSmax_i1
range *{R}*	O_Srang_r	OSrang_r8	OSrang_r1
range *{G}*	O_Srang_g	OSrang_g8	OSrang_g1
range *{B}*	O_Srang_b	OSrang_b8	OSrang_b1
range *{NIR}*	O_Srang_i	OSrang_i8	OSrang_i1
interquartile range *{R}*	O_Sintr_r	OSintr_r8	OSintr_r1
interquartile range *{G}*	O_Sintr_g	OSintr_g8	OSintr_g1
interquartile range *{B}*	O_Sintr_b	OSintr_b8	OSintr_b1
interquartile range *{NIR}*	O_Sintr_i	OSintr_i8	OSintr_i1
Texture (GLCM)			
GLCM Homogeneity *{Brightness}*	O_Thom_br	OThom_br8	OThom_br1
GLCM Contrast *{Brightness}*	O_Tcon_br	OTcon_br8	OTcon_br1
GLCM Dissimilarity *{Brightness}*	O_Tdis_br	OTdis_br8	OTdis_br1
GLCM Entropy *{Brightness}*	O_Tent_br	OTent_br8	OTent_br1
GLCM angular second moment (=energy) *{Brightness}*	O_Tsec_br	OTsec_br8	OTsec_br1
GLCM Mean *{Brightness}*	O_Tmean_br	OTmean_br8	OTmean_br1
GLCM Standard Deviation *{Brightness}*	O_Tstdv_br	OTstdv_br8	OTstdv_br1
GLCM Correlation *{Brightness}*	O_Tcor_br	OTcor_br8	OTcor_br1
Vegetated Objects			
proportion of vegetation *{NDVI ≥ 0.3}*	O_VpropVeg	OVpropVeg8	OVpropVeg1
Features derived from nDSM			
Measure of central tendency			
mean *{nDSM}*	E_Lmean_n	ELmean_n8	ELmean_n1
quartile50 *{nDSM}* (median)	E_Lmed_n	ELmed_n8	ELmed_n1
Measure of spread			
variance *{nDSM}*	E_Svar_n	ESvar_n8	ESvar_n1
standard devation *{nDSM}*	E_Sstdv_n	ESstdv_n8	ESstdv_n1
range *{nDSM}*	E_Srang_n	ESrang_n8	ESrang_n1
interquartile range *{nDSM}*	E_Sintr_n	ESintr_n8	ESintr_n1
Texture (GLCM)			
GLCM Homogeneity *{nDSM}*	E_Thom_n	EThom_n8	EThom_n1
GLCM Contrast *{nDSM}*	E_Tcont_n	ETcont_n8	ETcont_n1
GLCM Dissimilarity *{nDSM}*	E_Tdiss_n	ETdiss_n8	ETdiss_n1
GLCM Entropy *{nDSM}*	E_Tent_n	ETent_n8	ETent_n1
GLCM angular second moment (=energy) *{nDSM}*	E_Tsec_n	ETsec_n8	ETsec_n1
GLCM Mean *{nDSM}*	E_Tmean_n	ETmean_n8	ETmean_n1
GLCM Standard Deviation *{nDSM}*	E_Tstdv_n	ETstdv_n8	ETstdv_n1
GLCM Correlation *{nDSM}*	E_Tcorr_n	ETcorr_n8	ETcorr_n1
Elevated Objects			
proportion of elevated objects *{nDSM > 26}*	E_EpropEle	EEpropEle8	EEpropEle1
maximum of elevated objects *{nDSM > 26}*	E_Emax	EEmax8	EEmax1
mean of elevated objects *{nDSM > 26}*	E_Emean	EEmean8	EEmean1
minimum of elevated objects *{nDSM > 26}*	E_Emin	EEmin8	EEmin1
range of elevated objects *{nDSM > 26}*	E_Erang	EErang8	EErang1
standard deviation of elevated objects *{nDSM > 26}*	E_Estdv	EEstdv8	EEstdv1
variance of elevated objects *{nDSM > 26}*	E_Evar	EEvar8	EEvar1

Appendix D: *Naming key for vulnerability related features.*

Erklärung

Hiermit versichere ich an Eides statt, dass ich die vorliegende Arbeit ohne fremde Hilfe und ohne Benutzung anderer als der angegebenen Quellen und Hilfsmittel angefertigt und die den benutzten Quellen wörtlich oder inhaltlich entnommenen Stellen als solche kenntlich gemacht habe.
Diese Arbeit hat in gleicher oder ähnlicher Form noch keiner Prüfungsbehörde vorgelegen.

Germering, den

Marianne Jilge